HARVARD UNIVERSITY
Graduate School of Arts and Sciences

THESIS ACCEPTANCE CERTIFICATE

The undersigned, appointed by the

Division

Department of Physics

Committee

have examined a thesis entitled "Coulomb Blockade Spectroscopy of Tunnel-Coupled Quantum Dots"

presented by Carol Livermore

candidate for the degree of Doctor of Philosophy and hereby certify that it is worthy of acceptance.

Signature

Typed name Robert M. Westervelt, Chair

Signature

Typed name Bertrand I. Halperin

Signature

Typed name Michael Tinkham

Date May 15, 1998

Coulomb Blockade Spectroscopy of Tunnel-Coupled Quantum Dots

A thesis presented

by

Carol Livermore

to

The Department of Physics
in partial fulfillment of the requirements
for the degree of
Doctor of Philosophy
in the subject of

Physics

Harvard University
Cambridge, Massachusetts

May, 1998

UMI Number: 9832433

Copyright 1998 by
Livermore, Carol

All rights reserved.

UMI Microform 9832433
Copyright 1998, by UMI Company. All rights reserved.

This microform edition is protected against unauthorized
copying under Title 17, United States Code.

UMI
300 North Zeeb Road
Ann Arbor, MI 48103

© 1998 by Carol Livermore

All rights reserved.

Abstract

This thesis presents experimental studies of interactions in systems of coupled quantum dots. Quantum dots are often referred to as "artificial atoms" because the number of electrons on a dot is quantized, and those electrons occupy quantized energy levels. Two quantum dots coupled together by interdot electron tunneling may be considered an "artificial molecule". In this thesis we study artificial molecules composed of two quantum dots connected in series and use Coulomb blockade spectroscopy to measure the analog of a molecular binding energy. These measurements reveal how the effects of charge quantization on each individual dot are destroyed as interdot electron tunneling increases in both zero and strong magnetic fields.

In one set of experiments, we use transport measurements to monitor the double dot charge configuration as interdot electron tunneling is increased from near zero, where the dots are almost completely separated, to strong tunneling, where they are entirely joined by quantum mechanical charge sharing. These measurements demonstrate that in zero magnetic field, charge quantization effects on the two individual dots are destroyed when the interdot tunnel conductance is exactly $2e^2/h$. The charging diagram is shown to evolve in quantitative agreement with recent many body theories.

In other experiments, we study double quantum dots in the quantum Hall regime by applying a strong perpendicular magnetic field to the sample. We find that charge quantization weakens as the quantum Hall edge states on the two dots join, with quantization effects completely destroyed at e^2/h of interdot tunnel conductance. Finally, we find that as the magnetic field is varied, the electron distribution readjusts to minimize the energy. The adjustments form a pattern that repeats with magnetic field and with the addition of electrons.

Table of Contents

Acknowledgments

The last five years have been a rewarding time for me, and I would like to recognize the family, friends, and colleagues who have helped make it so.

First I would like to thank my advisor, Bob Westervelt. Bob's balance of guidance and willingness to let a student "follow her nose" has taught me a lot about science and the experimental approach and has enhanced my independence. I would also like to thank the other members of my committee, Professor Tinkham, Professor Halperin, and Professor Heller, for their advice and for the interest they have taken in my work.

I have benefited greatly from talking and working with our collaborators outside the Westervelt group. Bert Halperin, John Golden, Konstantin Matveev, and Piet Brouwer have offered many suggestions and are ever willing to explain pieces of physics from an experimentalist's point of view. I have enjoyed talking with Art Gossard and the members of his group at UCSB about experiments and sample design, and I am grateful to them for growing the material that has made our experiments possible.

I have worked particularly closely with several members of the Westervelt group. I had the pleasure of collaborating with Catherine Crouch for two years towards the beginning of grad school. I continue to benefit from our discussions of science and sociology, and I am pleased to report that her efforts to teach me tidy cabling were not entirely in vain. In the last year, I have also collaborated with Dave Duncan. Dave is an innovative physicist who can change his experimental approach on a dime, and I have enjoyed talking physics and analyzing career options with him. Rex Beck has offered considered and insightful advice on experiments throughout grad school, and our conversations in this year of job search and thesis have helped me keep a healthy dose of perspective. Mark Eriksson and I have had many a conversation about physics and life from our perches on opposite sides of the hallway.

The second floor of Gordon McKay Lab has been a great place to work, both because of the sheer number of knowledgable people who are willing to share their experience and because of the friendliness of the second floor denizens. I'm grateful to Doug Mar and Fred Waugh for their past and continuing guidance; to Dan Ralph for advice on many topics and his willingness to stir up a little good-natured trouble; and to Jack Hergenrother and Jia Lu for their patience, assistance, and cooperation with the old fridge. Jordan Katine's willingness to help has been almost as useful as the fact that he knows everything, and Aram Adourian's wry humor, interest in my efforts, and advice have proved invaluable.

I have benefited equally from the present occupants. Junmin Hu has always been ready with optimism and advice on jobs, and Mark Topinka brings his refreshingly pure interest in science to bear on all the group's projects. I have enjoyed Marija Drndic's straightforwardness and the scientific diversity she brings to the group. Lester Chen's openness and contributions to the common good and Jessica Shin's friendiness and willingness to lend a hand have made the second floor a better place to work. To them, and to the newest group member Chungsok Lee, I wish the best of luck in the future. I am also indebted to our neighbors down the hall in the Tinkham group. Sarah Pohlen has always been ready to offer technical advice and to commiserate about life in general. Drago Davidovic, Dolores Bozovic, and Alexey Bezryadin have all been considerate, friendly, and helpful neighbors.

Steve Shepard's expertise and smooth management of the cleanroom have been invaluable, and I am grateful to Yuan Lu for his capable supervision of the SEM facilities. Louis DeFeo and the guys in the machine shop deserve a huge thank you for their assistance and their expert, friendly advice. Through the continuing saga of the broken dilution fridges, they have made our priorities their priorities. Thanks go to David Lovler for helping the group navigate the complexities of university paperwork. To Ed Hogan I owe the same gratitude, plus thanks for his varied outside interests that kept my eyes open to the broader world outside the walls of the lab.

My housemates from early grad school, Neepa Maitra and Sheila Kannappan, have been thoughtful and supportive friends for the past five years. I remain thankful that we were able to have such useful conversations about grad school and our experiences without letting physics overrun the house.

Finally, I am deeply grateful to my family for their support. I've enjoyed the camaraderie as my brother Matt and I have faced school together. My sister Anne found time to worry about me and advise me despite the pressures of motherhood and getting her own graduate degree. My parents provided me with the early (and continuing) encouragement to explore, learn, make things, and do things. Through the last five years, they have helped me look in the mirror to see my own direction. Finally, I thank my husband Jim, who has believed in me and supported me throughout, even proving himself an expert fridge assistant. Together we have explored the path behind us, and I look forward to the road ahead.

Chapter 1

Introduction

1.1 Motivation

The physics of small devices becomes progressively more important as the size of electronic devices and systems decreases. Smaller electronics mean greater speed of operation, but scaling devices and systems brings problems ranging from device failure to stray interactions among closely spaced devices. These issues have sparked researchers to examine nanoelectronics, both to seek candidate building blocks for new types of circuitry and to understand the physical issues of scaling electronics. In this way technology provides a motivation for studying nanoelectronics. In turn, it also offers a tool. Using techniques like electron beam lithography, it is possible to define electronic structures whose behavior is governed by both classical physics and quantum mechanics. Studying these systems can shed light on possible futures for electronics; it also opens the door to fascinating basic physics in the realm of the mesoscopic.

This thesis describes experiments that probe interactions in systems of quantum dots coupled together by the tunneling of electrons. A quantum dot is a small, isolated island of electrons. For our devices, small means that there are several hundred electrons occupying an island about half a micron in size. It also means that the capacitance of the island to the rest of the world is small enough that the energy required to charge up this capacitor with even a single electron beyond its optimal charge is large relative to other energy scales, like the temperature. By isolated, we mean that quantum mechanical tunneling from the island to nearby leads, or electron reservoirs, is sufficiently weak that the island charge is quantized.

Quantum dots are a good example of a system that is studied both for its technological relevance and basic physical interest. The essential property of a quantum dot is its small size; the smaller a dot is, the more pronounced its characteristic dot behavior becomes. This is promising for scaleability, and there exist many proposals for using quantum dots as a building block for practical devices. These include single electron memory elements, in which a bit of information is stored by the presence or absence of a single electron on a quantum dot or island [Dresselhaus *et al.*, 1994; see also *Single Charge Tunneling* (eds. Grabert and Devoret), 1992]; single electron logic, in which quantum dots are used as transistors [Tucker, 1992; Korotkov *et al.*, 1995]; quantum dot cellular automata, which uses electrostatic interactions to move charges and compute [Lent *et al.*, 1993]; and certain quantum computing schemes [Loss *et al.*, 1998]. Dots also exhibit interesting basic physics. In one common analogy, dots are referred to as "artificial atoms" because they contain a small number of electrons occupying quantized energy levels in a small region of space [Kastner, 1993; Tarucha *et al.*, 1996].

We have chosen to study interactions among quantum dots for both technological and basic physics reasons. The ability to build practical structures from groups of quantum dots hinges on understanding the interactions among quantum dots and between dots and their environment. For example, the ability of electrons to tunnel between neighboring quantum dots corresponds to error rates in many of the structures mentioned above. From the basic physics point of view, coupled quantum dots are also rewarding. If one quantum dot is an artificial atom, then two quantum dots coupled together by the tunneling of electrons may be considered an "artificial molecule". In the artificial system, we can study questions that are inaccessible in real molecular systems. Because we have relatively larger systems that we can fabricate with plenty of experimental "knobs" to turn, we can vary parameters that are fixed in natural molecules. For example, we can ask how a molecular bond forms as electrons are permitted to tunnel more and more strongly between two artificial atoms. These experiments also allow us to examine issues of charge quantization in many body systems, a complex issue of substantial interest in recent condensed matter theory.

1.2 Summary of the thesis

This thesis describes the experiments we have done to understand systems of coupled quantum dots. After the introduction, we devote the second chapter to a discussion of the major players in our experiments: two-dimensional electron gases, quantum point contacts, and individual quantum dots. In addition to discussing the properties of these components, we describe our basic tools for measuring them, transport measurements and Coulomb blockade spectroscopy. The third chapter describes our experimental methods. In the first part, we address electron beam lithography and the other fabrication techniques with which we make our samples. The second part describes our measurement apparatus, including the electronics setup for the transport measurements and the cryogenic systems in which we cool our devices for study.

The fourth and fifth chapters present the central experimental results of this thesis. Chapter 4 describes a study of two identical quantum dots connected in series between source and drain leads. The two dots are each occupied by separately adjustable numbers of electrons, and the degree of electron tunneling between the two dots is experimentally controllable. In this experiment we monitor the conductance of the double quantum dot as a function of all three parameters: the two dot charges and the interdot tunnel conductance. Using Coulomb blockade spectroscopy, we observe and quantify how charge quantization on the individual dots is lost in the evolution from two separate "artificial atoms" to one composite "artificial molecule". Experimental results are presented along with an outline of and comparison with applicable theory.

Chapter 5 presents the results of our experiments on coupled quantum dots in a strong perpendicular magnetic field (the quantum Hall regime). We describe experiments that measure the weakening of charge quantization on two dots of different sizes in the high magnetic field limit. We also present transport measurements that reveal charge redistributions and Landau level depopulations when the magnetic field is varied.

Chapter 6 contains the conclusions of this thesis and a discussion of possible future directions for study. Further detail on the electronics set up is provided in Appendix A.

Chapter 2

Building Blocks for Quantum Dot Structures

This chapter introduces the building blocks that make up coupled quantum dots: two-dimensional electron gases (2DEGs), quantum point contacts, and individual quantum dots. Understanding these components gives us a framework in which to think about coupled quantum dots and allows us to extract the physical parameters that characterize our devices.

We begin by describing 2DEGs and how we use them to construct nanostructures. We explain how we define a narrow constriction in a 2DEG, a quantum point contact, and use it as a tunneling barrier between two neighboring regions of electron gas. The following section describes how we use the same techniques to confine a small region of 2DEG to form a quantum dot. Finally, we present the Coulomb blockade description of electron transport through a quantum dot.

2.1 Two-dimensional electron gas and split gate devices

Our quantum dot devices are fabricated in a GaAs/$Al_xGa_{1-x}As$ heterostructure wafer that contains a two-dimensional electron gas (2DEG).[1] The subscripts x and 1-x are subsequently omitted for brevity. A GaAs/AlGaAs heterostructure consists of alternating lattice-matched layers of GaAs and AlGaAs grown by molecular beam epitaxy (MBE). The 2DEG is a two-dimensional sheet of electrons that forms at the interface between two neighboring layers of GaAs and AlGaAs a short distance beneath the surface of the wafer

---

[1] For our samples, $x = 0.31$, large enough to offer a substantial band edge discontinuity and small enough to keep the lattice constants well matched.

[Dingle *et al.*, 1978]. The 2DEG sheet automatically provides one dimension of electron confinement, leaving just two dimensions to confine through lithography.

The heterostructures used in this thesis were grown by Ken Campman and Kevin Maranowski using the MBE setup in Art Gossard's laboratory at the University of California in Santa Barbara. With MBE a structure is grown one atomic layer at a time in ultra-high vacuum so that each atom ends up in its proper place in the crystal. Since the lattice constants of GaAs and AlGaAs are very similar, the layers form with little strain and few defects. For detailed discussions of MBE and the UCSB setup, see for example Herman and Sitter [1989] and previous group theses [Hopkins, 1990; Baskey, 1994].

Figure 2.1a is a diagram of the growth profile for a typical heterostructure. The left side corresponds to the surface of the wafer; the right side is the [100] GaAs substrate. Starting from the substrate, the initial buffer layer of GaAs is followed by a smoothing superlattice, a series of twenty alternating layers of GaAs and AlGaAs that smooth crystal defects that originate in the substrate. The smoothing superlattice is followed by a thick 1 μm layer of GaAs that constitutes one side of the interface on which the 2DEG forms. A layer of AlGaAs grown on top of the GaAs completes the interface. Embedded in the AlGaAs is a Si delta doping layer, a sheet of Si donor atoms less than one atomic layer thick. The structure is capped with a thin layer of GaAs because GaAs oxidizes more slowly than AlGaAs in air. A blowup of the near surface layers is shown in figure 2.1b. This structure corresponds to wafer KC7, which was used for the experiments in chapter 4. Wafer KM3, used for the magnetic field experiments in chapter 5, has similar structure.[2]

Figure 2.1c is a plot of the conduction band edge when the system is in equilibrium. The conduction band edge has a discontinuity at the GaAs/AlGaAs interface. The Si donors provide the crystal with excess electrons. Some of these electrons travel to the wafer's surface states; others migrate deeper into the wafer and "fall" over the conduction band

---

[2] The designation KC7 refers to the seventh wafer that we received from Ken Campman in Gossard's group. Similarly, KM3 is the third wafer that we received from Kevin Maranowski.

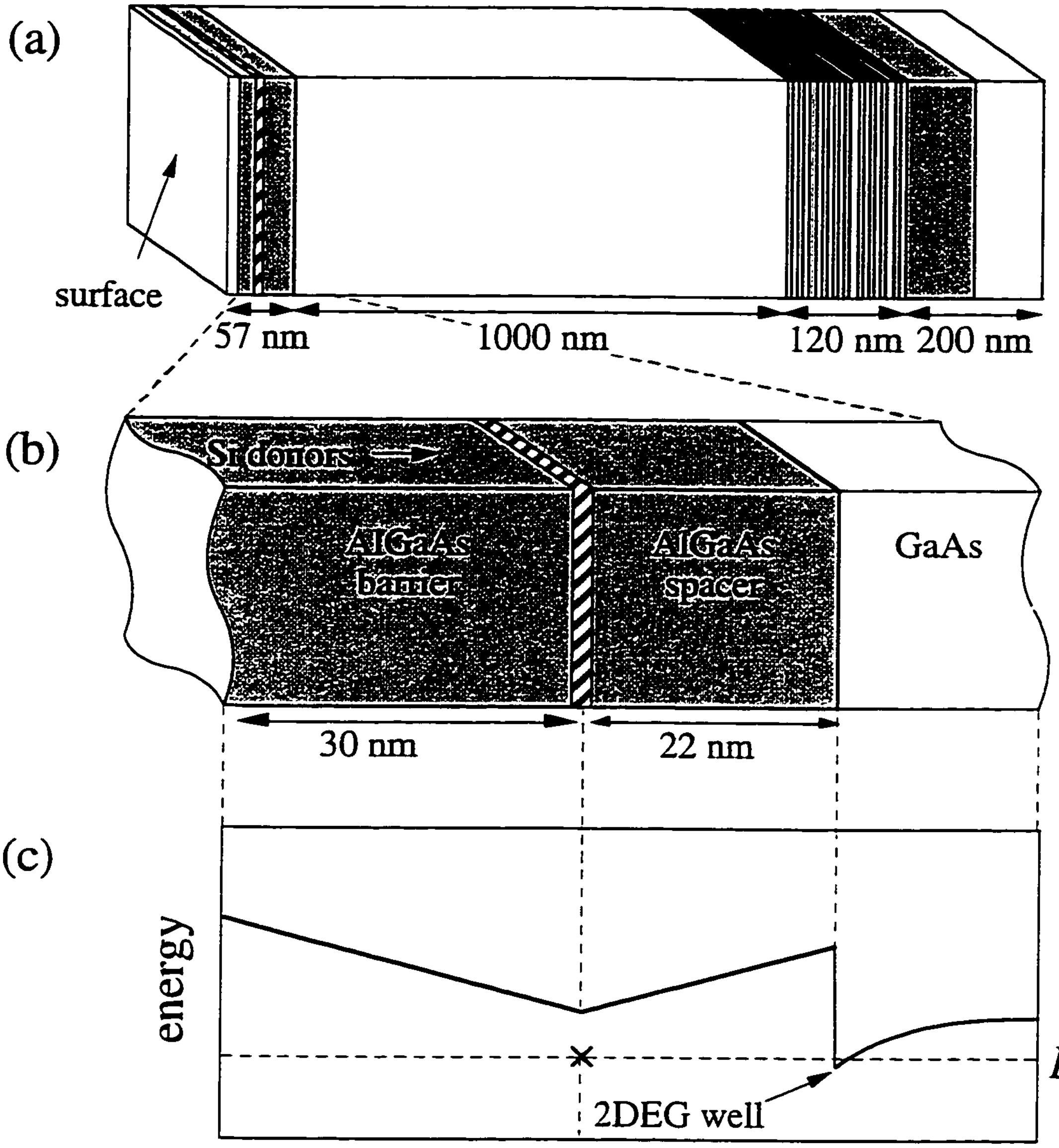

Figure 2.1 (a) Schematic diagram of layer structure in a GaAs/AlGaAs heterostructure wafer. Growth direction is from substrate on right to surface on left. White areas represent GaAs, shaded areas are AlGaAs, and banded stripe represents Si δ-doping layer. (b) Blowup of near-surface structure, where 2DEG forms. (c) Conduction band energy after equilibration of donor electrons. After Waugh, Ph.D. thesis [1994].

edge discontinuity into the GaAs layer. The resulting electric field bends the bands in a V shape around the Si donor layer. The band edge discontinuity and the band bending form a potential well at the GaAs/AlGaAs interface. The density of Si donors is chosen to place the Fermi level between the first and second subbands of the well, ensuring that all electrons are in the lowest subband. The electron layer is called a two-dimensional electron gas because the electrons have only two spatial degrees of freedom and are well approximated as non-interacting particles in those dimensions.

The wafer structure and growth conditions determine the 2DEG's properties. Sheet density rises with donor concentration, and mobility increases with 2DEG depth. The physics of 2DEGs is described in detail in Beenakker and van Houten [1991] and is recapped in previous Westervelt theses [see for example Katine, 1996]. Here we simply summarize our wafer properties. KC7 has an unilluminated mobility $\mu \cong 500{,}000$ cm^2/Vs and sheet density $n_s \cong 3.5 \times 10^{11}$ cm^{-2} at 10 K; the mobility is enhanced at lower temperatures. KM3 has an unilluminated mobility $\mu \cong 450{,}000$ cm^2/Vs and sheet density $n_s \cong 3.4 \times 10^{11}$ cm^{-2}.[3] We have also begun using wafer CK1, a lower density wafer grown by Christoph Kadow in Art Gossard's group, but it is not represented by any of the completed results presented in this thesis. This wafer is designed with a lower sheet density $n_s \cong 1.8 \times 10^{11}$ cm^{-2} and is appropriate for high magnetic field experiments in the quantum Hall regime.

Figure 2.2 is a schematic diagram of how we define structures in a 2DEG. We pattern metal gates on the wafer surface with electron-beam lithography. The gates couple capacitively to the underlying 2DEG. When the gates are energized with a sufficiently negative voltage, the electrons beneath the gates are depleted, forming a barrier region through which electrons cannot flow [Thornton *et al.*, 1986; Zheng *et al.*, 1986]. In figure 2.2 the gates define a quantum dot. The dot is the small puddle of electrons directly beneath the center area that is not covered by gates.

---

[3] This sheet density was determined from the period of the Shubnikov-de Haas oscillations in a perpendicular magnetic field at 30 mK.

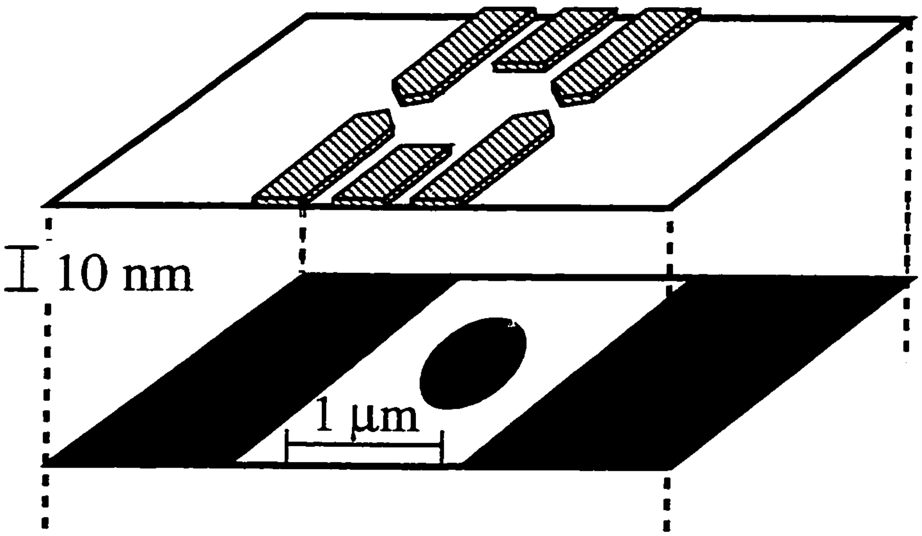

Figure 2.2 Schematic diagram of a quantum dot defined by split electrostatic gates (hatched) on the surface of a GaAs/AlGaAs heterostructure containing a 2DEG (shaded). When the gates are energized with a negative voltage, the underlying 2DEG is depleted to define a nanostructure. After Waugh [1994].

In a strong perpendicular magnetic field a 2DEG enters the quantum Hall regime and is no longer well described as free electrons in two dimensions. The new states are Landau levels, and they have energies

$$E_n = \left(n - \frac{1}{2}\right)\frac{h}{2\pi}\omega_c, \quad \omega_c = \frac{eB}{m} \qquad (2.1)$$

where n is the Landau level index. In practice the energy also includes the Zeeman splitting and the confining potential of the device. These states are highly degenerate, with one electron per flux quantum for a filled Landau level. The magnetic field and the sheet density of the electrons determine the number of filled Landau levels. The number of filled Landau levels, counting spins separately, is known as the filling factor and is given by

$$\nu = \frac{n_s h}{eB} \qquad (2.2)$$

where n_s is the sheet density of the 2DEG wafer. In a semiclassical picture, each of these electrons circles in response to the Lorentz force. In the quantum mechanical description as well, the electrons in the bulk are localized. For a detailed description, see for example Beenakker and van Houten [1991].

The electron states at the edges of the sample dominate transport in the quantum Hall regime [Halperin, 1982]. In our semiclassical picture, when the circular orbits of these electrons intersect the sample boundaries, they skip along the edge and contribute to transport. In reality, these edge channels are extended states along the boundary. Since these states are not localized, they can carry a current.

2.2 Quantum point contacts

Quantum point contacts are narrow constrictions in the path of electron flow. Our point contacts are formed by energizing two surface gates that are separated by about 100 nm. Figure 2.3 is a scanning electron micrograph of a device that includes three point contacts. The sets of point contact gates are lettered A, B, and C. Figure 2.4 is a plot of the conductance measured through a quantum point contact (corresponding to point contact B on device KC7EE) in zero magnetic field as a function of the voltage applied to the surface gates. The conductance was measured at base temperature (75 mK) in the Oxford dilution refrigerator. The conductance through the quantum point contact is quantized in units of $2e^2/h$; the step edges are thermally broadened.

Point contact conductance quantization is a result of energy level quantization in the constriction [see for example Beenakker and van Houten, 1991]. The confining potential has a saddle shape, resulting in a potential well perpendicular to the transport direction. Each occupied subband of the well contributes $2e^2/h$ (one conductance quantum for each of two spin modes) to the conductance; the total conductance is determined by the number of subbands beneath the Fermi level, as described in Beenakker and van Houten [1991]. A more negative point contact voltage narrows the well, increases the subband energies, and makes higher modes inaccessible for electron transport.

For coupled quantum dot experiments we usually keep point contacts between zero conductance and the first conductance plateau. In that range, electrons tunnel through an energy barrier with a height and width controlled by the point contact voltage. When the point contact is on the first conductance plateau, we say that the conductance is one full spin degenerate mode. Equivalently, the constriction is broad enough to admit half of a Fermi wavelength.

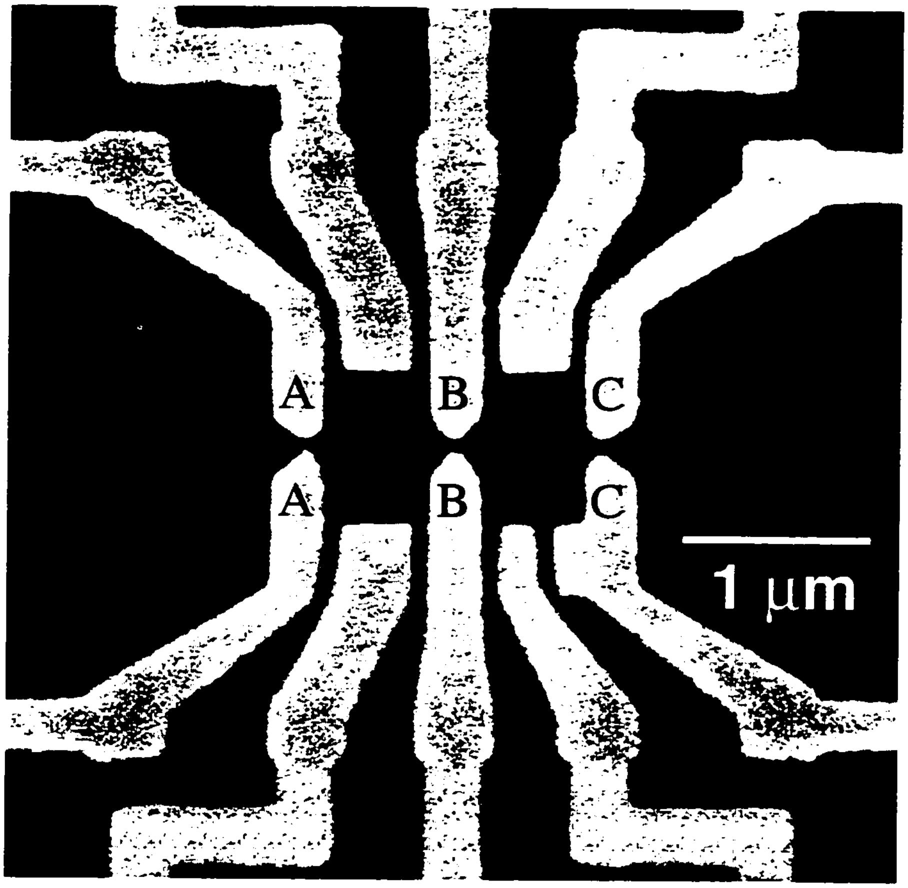

Figure 2.3 SEM micrograph of a double quantum dot with quantum point contacts indicated. Light regions are the metal surface gates; dark areas are the wafer surface. Each pair of gates A, B, and C defines a different point contact.

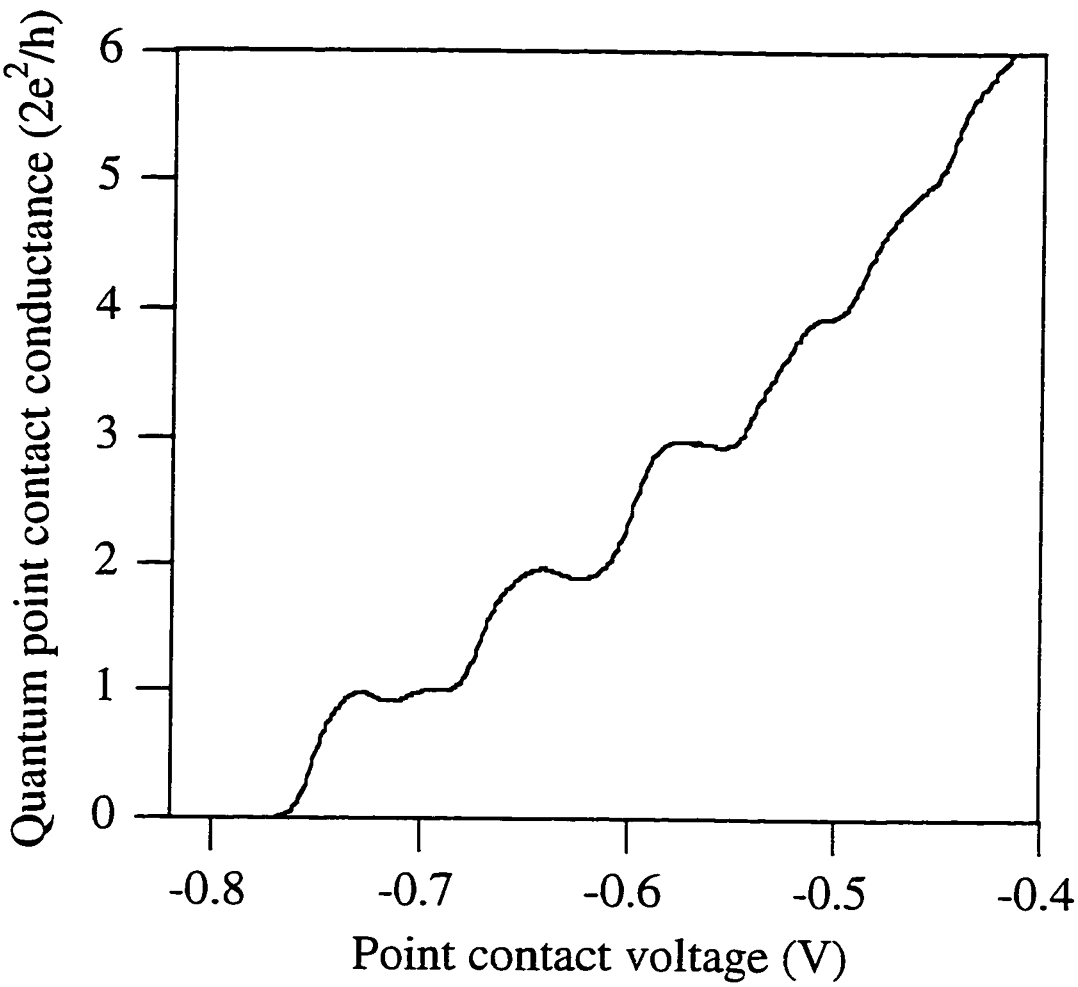

Figure 2.4 Conductance through a quantum point contact plotted vs. the voltage applied to the point contact gates, measured at dilution refrigerator base temperature (25 mK). The conductance is quantized in units of $2e^2/h$.

2.3 Single quantum dots

Coulomb blockade

A quantum dot is a small, isolated island of electrons with some capacitive coupling to its environment and a weak coupling through tunnel junctions to electrical leads. Figure 2.5 is a schematic diagram of a dot. The shaded circle represents the island; the leads are the neighboring shaded areas. The capacitive coupling to other objects (i.e. surface gates) is shown schematically by the capacitor plate. By varying the potential of these capacitively coupled gates, we can induce charge on the quantum dot. Such small islands were first examined by Fulton and Dolan [1987]; for later work see Grabert and Devoret [1992] and references therein.

The device in figure 2.3 is two quantum dots in series. A single quantum dot forms when, for example, gates A and B and the two side gates between them are all energized with a negative voltage. The two point contacts serve as gateways between the quantum dot and the leads; the side gates confine the dot laterally. The result is a small puddle of electrons in the underlying electron gas: the quantum dot.

What do we mean when we say that a quantum dot is small? The capacitance of the dot must be small enough that the electrostatic energy required to add one electron to the system is larger than other relevant energy scales, such as the temperature. The energy scale for adding an electron is the charging energy, defined here as $E_C = e^2/2C_\Sigma$. A typical lithographic dimension for our dots is 500 nm x 800 nm; the actual dot is somewhat smaller because of the finite depletion length and contains about 800 electrons. This yields a charging energy $E_C \cong 230$ μeV that is much greater than the electron gas temperature $kT \cong 7.5$ μeV at base temperature in our dilution refrigerator. The electron gas temperature $T \cong 70$ mK exceeds the mixing chamber temperature $T \cong 25$ mK.

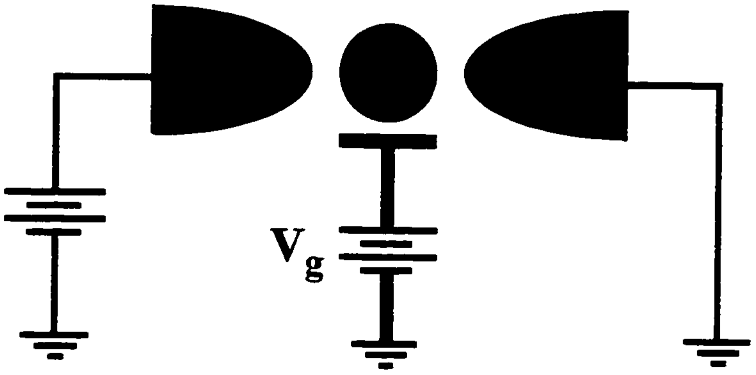

Figure 2.5 Schematic diagram of a quantum dot (shaded circle) weakly tunnel coupled to two leads (neighboring shaded regions) and capacitively coupled to a nearby electrostatic gate at a potential V_g.

When we say that a quantum dot is isolated, we mean that it is separate enough from its leads that its charge is quantized. This condition limits the resistance of the tunnel junctions between dot and leads. Starting with the energy-time statement of the uncertainty principle, $\Delta E \Delta t > h/2\pi$, and taking Δt to be the RC lifetime of an electron on the island and ΔE to be the charging energy E_C, we find

$$\frac{e^2}{2C_\Sigma} R_L C_\Sigma >> \frac{h}{2\pi} \tag{2.3}$$

$$R_L >> \frac{h}{e^2} \tag{2.4}$$

where R_L is the resistance of the tunnel junctions separating the dot from the leads.

Under most circumstances it is not possible to pass a current through a quantum dot because it is too energetically expensive to move electrons on and off the island. This effect is called the Coulomb blockade of current flow. We will start our discussion of the Coulomb blockade by treating the quantum dot as a small piece of metal. There are quantum mechanical corrections to this description. Our dots are actually many-body systems, and the total energy includes the electrostatic energy and the energy of the quantum mechanical states. Our initial approach neglects quantized energy states and models the quantum dot system as an electrostatic circuit.

Figure 2.6a is an equivalent circuit for a quantum dot. The dot is again represented by the shaded circle; the dot is connected to the leads by tunnel junctions, shown as split boxes in the circuit diagram. Each of these junctions has some capacitance C_L and some resistance R_L (discussed previously) between dot and lead. The dot is coupled via capacitor C_g to a side gate with a variable applied voltage V_g; the dot has additional capacitance C_{stray} that essentially couples it to ground. Since we are considering a very small ac bias voltage between the leads, the lead capacitances are also essentially to ground.

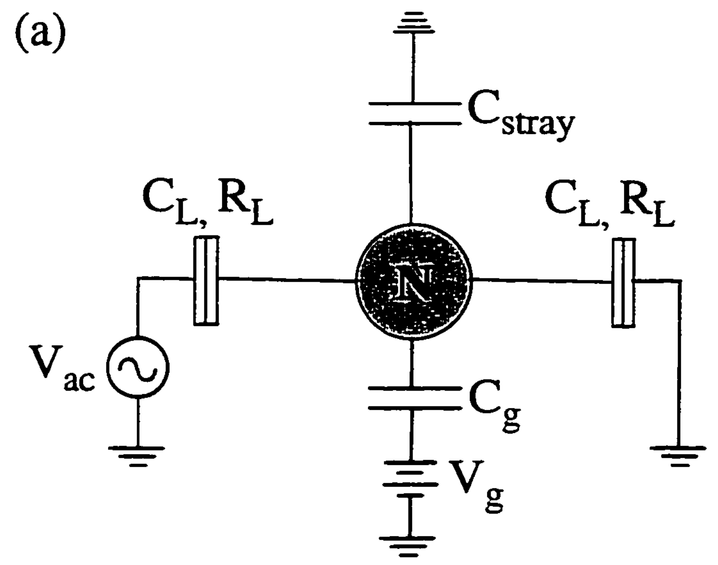

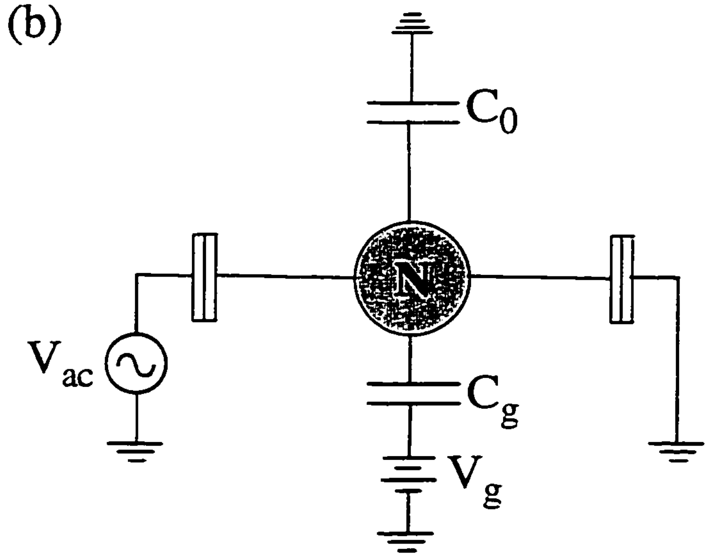

Figure 2.6 (a) Equivalent circuit diagram for a quantum dot, including the dot-gate capacitance, the stray capacitance, and the resistance and capacitance between dot and leads. (b) Modified equivalent circuit with lead capacitance subsumed in the total stray capacitance C_0. This model suffices in the absence of a finite bias voltage across the dot.

Figure 2.6b shows a simplified circuit, where the various capacitances to ground have been combined into one quantity $C_0 = 2C_L + C_{stray}$. We define the total capacitance of the dot $C_\Sigma = C_0 + C_g$. The quantized island charge is Ne, where N is the number of electrons on the dot.

It is important to ask how the charge on the quantum dot depends on the voltages applied to the side gates. Figure 2.7a is a plot of the actual quantized charge on the dot and the charge induced by the side gate voltage V_g as a function of V_g. The induced charge increases linearly with side gate voltage. Charge quantization dictates that the actual dot charge cannot vary linearly; rather, it increases stepwise in its best approximation of the induced dot charge. The system has its lowest energy whenever the actual and induced dot charges are equal. When they are unequal, the system has a frustrated charge configuration and a higher electrostatic energy.

We can calculate the total electrostatic energy $E_{dot}(V_g, N)$ and use it to understand the Coulomb blockade. Following the conventions in Tinkham [1996], we observe that E_{dot} is the total energy stored in the capacitors minus the work done by the battery to reach that configuration.

$$E_{dot} = \frac{1}{2}\sum_i C_i (V_i - \phi)^2 - \sum_i C_i V_i (V_i - \phi) \qquad (2.5)$$

The parameter ϕ is the potential on the dot, given by

$$\phi = \sum_i (C_i V_i - Ne)/C_\Sigma \qquad (2.6)$$

Only the terms that depend on N affect transport. Substituting in and eliminating all terms independent of N, we find the total electrostatic energy of the dot.

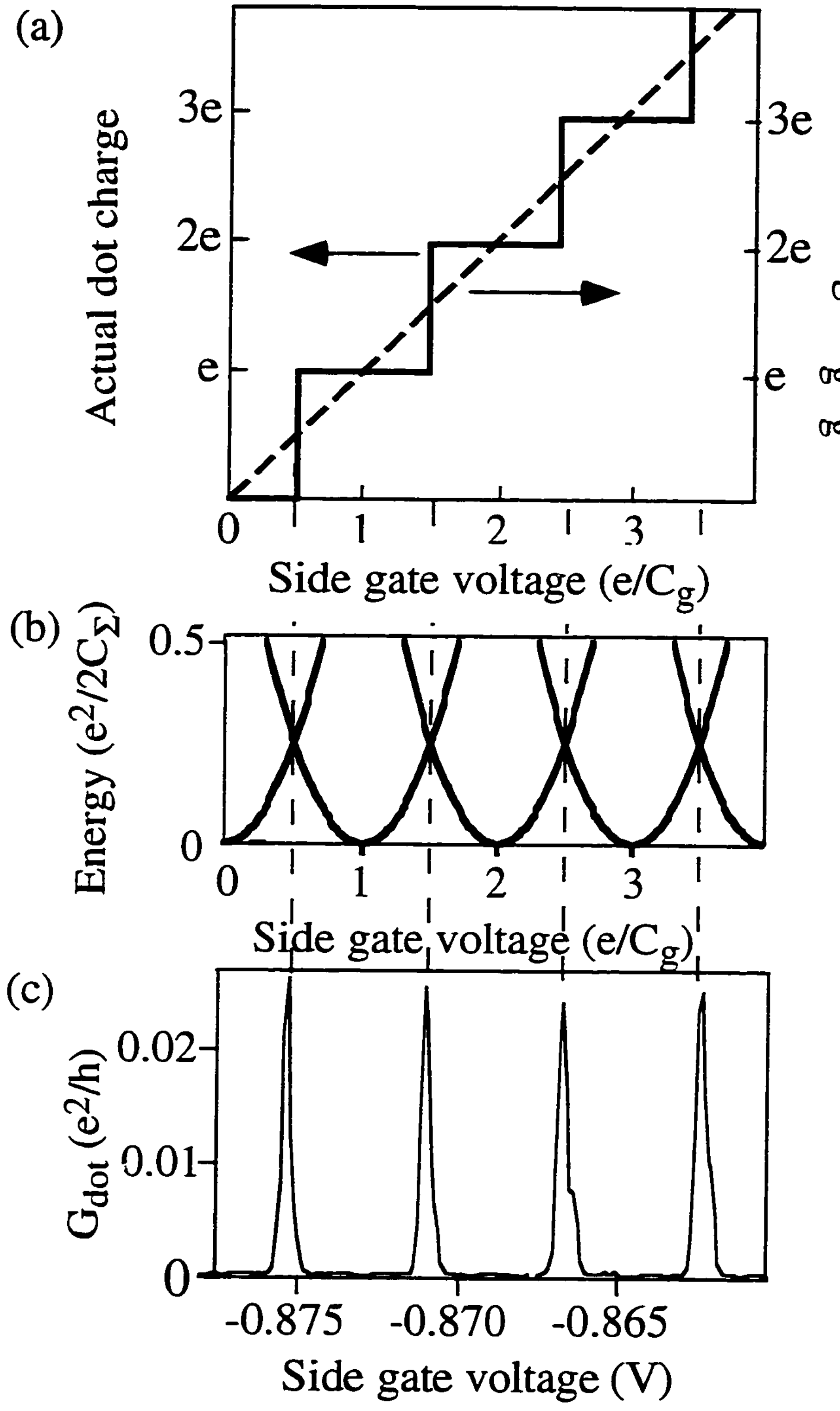

Figure 2.7 (a) Actual charge and charge induced by side gate vs. side gate voltage. (b) Electrostatic energy of dot U(Vg, N) vs. side gate voltage. (c) Measured Coulomb blockade conductance peaks vs. side gate voltage.

$$E_{dot} = \frac{\left(C_g V_g - Ne\right)^2}{2C_\Sigma} \tag{2.7}$$

The result is just the energy cost to store the difference between the actual and induced charges in a capacitor C_Σ.

Figure 2.7b is a plot of the total energy E_{dot} as a function of the side gate voltage V_g. For a given number of electrons N on the dot, the energy is parabolic. Parabolas corresponding to different values of N are offset from one another along the V_g axis. The energy required to change N is the difference between the lowest and second lowest energy parabolas, and it is on the order of the charging energy E_C. This substantial energy cost prevents current from flowing at any gate voltage except where two parabolas cross and the energy cost goes to zero. At the crossing points where the energies of the N and N + 1 states are equal, the electron number may fluctuate freely between them. Figure 2.7c is a plot of the measured conductance through a quantum dot. As predicted, we observe a series of peaks in conductance as a function of V_g. We will refer to these as "conductance oscillations" or "Coulomb blockade peaks". The gate to dot capacitance C_g determines the peak spacing by the relation $C_g \Delta V_g = e$. We use this relation to calibrate C_g for each sample.

Effects of finite level spacing

We have assumed so far that dots may be completely described in terms of the electrostatic interactions of the electrons. This would be the case if there were a continuum of energy levels on the dot. We now refine the model by adding single particle quantum states. This is an improvement because we now treat both particle interactions (via electrostatics) and quantized energy levels (via a particle in a box approximation), but it is not a complete many-body treatment of the quantum dot system.

With a finite level spacing, the energy of the system is the sum of the electrostatic charging energy and the additional energy of the quantum states into which the electrons tunnel,

$$E_{dot} = \frac{(C_g V_g - Ne)^2}{2C_\Sigma} + \sum_n \varepsilon_n \tag{2.8}$$

where ε_n is the energy of an occupied single particle state. The relative sizes of the average energy level spacing $\delta\varepsilon$, the charging energy E_C, and the thermal energy kT govern how strongly the quantized energy levels affect transport. We estimate $\delta\varepsilon = 2E_F/N \cong 35$ μeV, using $E_F \cong 14$ meV as the Fermi energy of the 2DEG system (measured via the sheet density) and $N \cong 800$ for the number of electrons on a typical dot (estimated from the dot area). The factor of two comes from the spin degeneracy of electron states. For comparison, the electron gas temperature $kT \cong 7.5$ μeV. Since the level spacing is on the order of 4kT, we are on the border of where the level spacing has observable effects. The charging energy $E_C \cong 230$ μeV is much larger than the level spacing, so electrostatics remain the dominant energy in the problem.

A finite level spacing destroys the perfect periodicity of the Coulomb oscillations because the energy required to add the next electron is the sum of the electrostatic energy and the level spacing, which may vary. Finite level spacing also results in nonuniform peak heights. Figure 2.8 is a plot of the conductance of a quantum dot vs. side gate voltage V_g over many periods of the Coulomb oscillations. The peak heights vary substantially (and non-monotonically) over this range. Since the level spacing is on the order of the thermal broadening, transport occurs through one or a few of the lowest levels. The height of the peak is affected by the coupling of the available state(s) to the leads; if there is little overlap between the wavefunction in the leads and in the dot, the peak height is suppressed. The peak heights vary slowly, indicating that subsequent states do not have

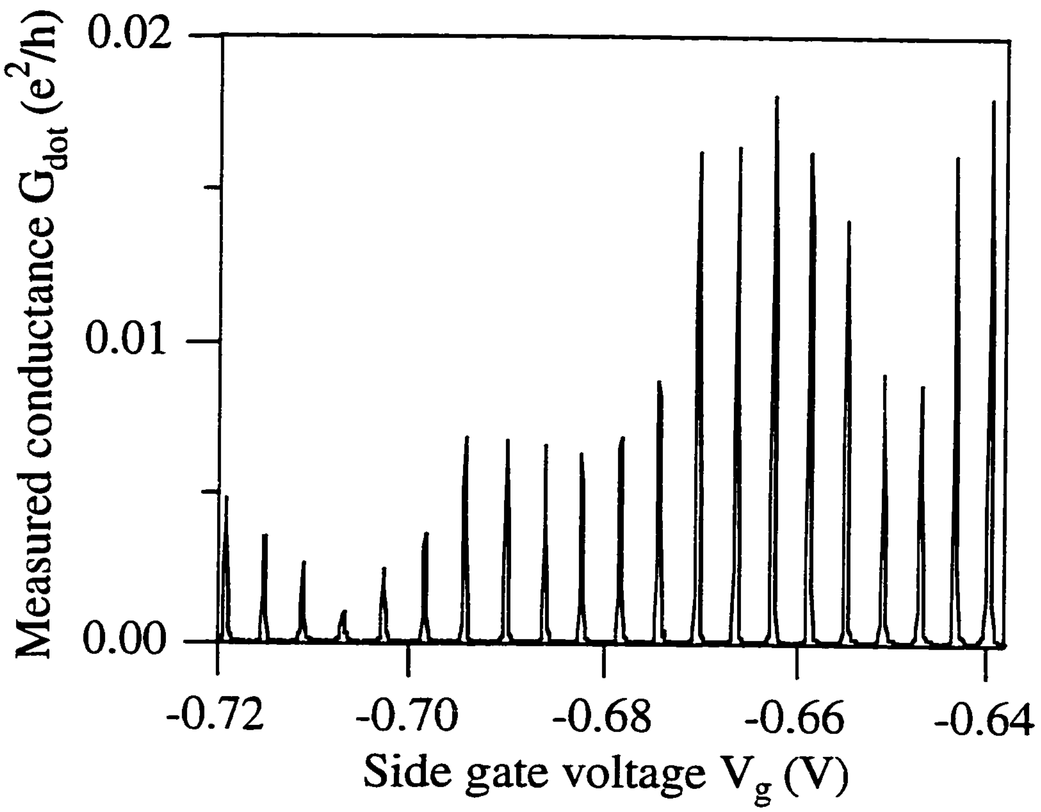

Figure 2.8 Coulomb oscillations measured in a single dot vs. side gate voltage. Variations in peak height reflect the finite energy level spacing.

vastly different wavefunctions but rather undergo a slow evolution. By contrast, the heights of the Coulomb oscillations for micron-scale metal SETs are uniform from peak to peak because the level spacing is essentially continuous.

When $E_C >> \delta E >> kT$ and the tunneling rate Γ to the leads is low ($h\Gamma << kT$), the peak shape is given by

$$G(V_g) = G_0\left[\cosh\left(\frac{eC_g\left(V_g - V_{g0}\right)}{aC_\Sigma k_B T}\right)\right]^{-2} \tag{2.9}$$

The prefactor G_0 is determined by the tunneling rates of the two leads and by the overlap of the wavefunctions in dot and lead. The constant a is either a = 2 (when transport is through the lowest state only) or a = 2.5 (if the level spacing is continuous) [van Houten *et al.*, 1992]. Figure 2.9 is a plot of several Coulomb oscillations fit to the above line shape with a = 2. The good agreement indicates that our peaks are broadened by thermal effects rather than by the conductance to the leads (lifetime broadening). Lifetime broadening would yield a Lorentzian line shape [Foxman *et al.*, 1993; see also van Houten *et al.* in *Single Charge Tunneling*, 1992].

Current-voltage characteristics

We calibrate the total dot capacitance C_Σ by measuring differential conductance through the dot as a function of a finite drain-source bias voltage V_{ds} applied between the two leads[4]. As before, current flows when there is near zero bias voltage and the N and N + 1 charge states are degenerate. Current can also flow if the bias voltage is large, so that the Fermi level in the leads is higher than the energy to add another electron.

Once again the total electrostatic energy determines to lowest order when current flows. The calculation is similar. We put in the lead capacitances C_L explicitly, add another battery, and include the work done by the battery voltage V_{ds} on the electrons that tunnel

---

[4] The ac voltage source in the circuit in Fig. 2.06 is replaced by a variable dc voltage source.

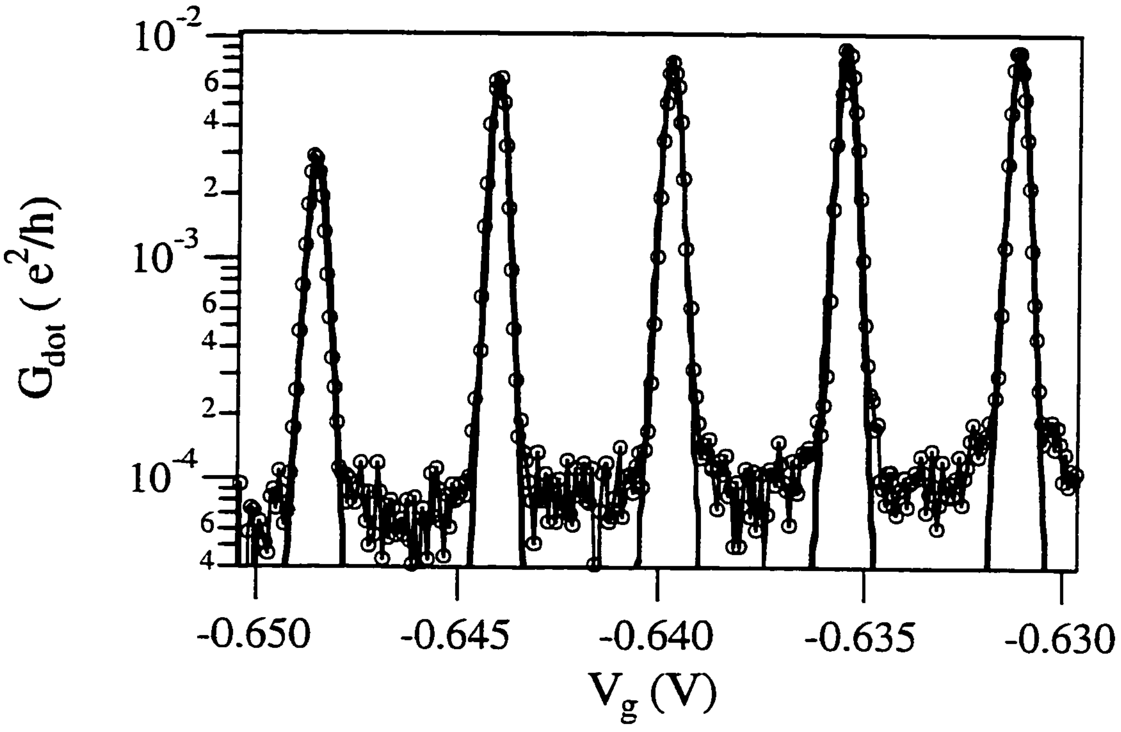

Figure 2.9 Conductance oscillations and fits to a thermally broadened lineshape. Open circles are measured conductance; thick line is fit. These data were measured at base temperature (25 mK). The fit yields an electron gas temperature T ≅ 95 mK for these data.

onto the island. (For details, see for example Averin and Likharev [1991] or the calculation in Crouch [1996a].) We find that the Coulomb blockade is in effect when the following four conditions are met.

$$N+\frac{1}{2}>\frac{C_g V_g}{e}+\frac{C_L V_{ds}}{e}>N-\frac{1}{2} \tag{2.10a}$$

$$N+\frac{1}{2}>\frac{C_g V_g}{e}-\frac{(C_\Sigma - C_L)V_{ds}}{e}>N-\frac{1}{2} \tag{2.10b}$$

The result is that current flow is prohibited in diamond shaped regions in the V_g-V_{ds} plane, each of which corresponds to a different lowest energy value of N. Figure 2.10 is a plot of differential conductance dI/dV measured through a quantum dot as a function of the side gate voltage V_g and the drain-source bias V_{ds} [Crouch *et al.*, 1997]. When $V_{ds} = 0$, it reduces to the familiar case of periodic conductance peaks as a function of V_g. The height of the diamond, as marked in the figure, is given by e/C_Σ. In finite bias measurements, the level spacing manifests itself as features in the current above the Coulomb gap, also visible in the data. When the bias increases enough to make another discrete state available for transport, the current increases. Peaks in the measured differential conductance indicate a level spacing consistent with our earlier 30 μeV estimate.

Single quantum dots in the quantum Hall regime

The behavior of single quantum dots in the quantum Hall regime depends strongly on the magnetic field. A number of experiments have examined single quantum dots in a strong perpendicular magnetic field [McEuen *et al.*, 1991; McEuen *et al.*, 1992; McEuen *et al.*, 1993; Klein *et al.*, 1995; Klein *et al.*, 1996; Ashoori *et al.*, 1993; Zhitenev *et al.*, 1997]. Figure 2.11a is a schematic diagram of the energy of electron states as a function of

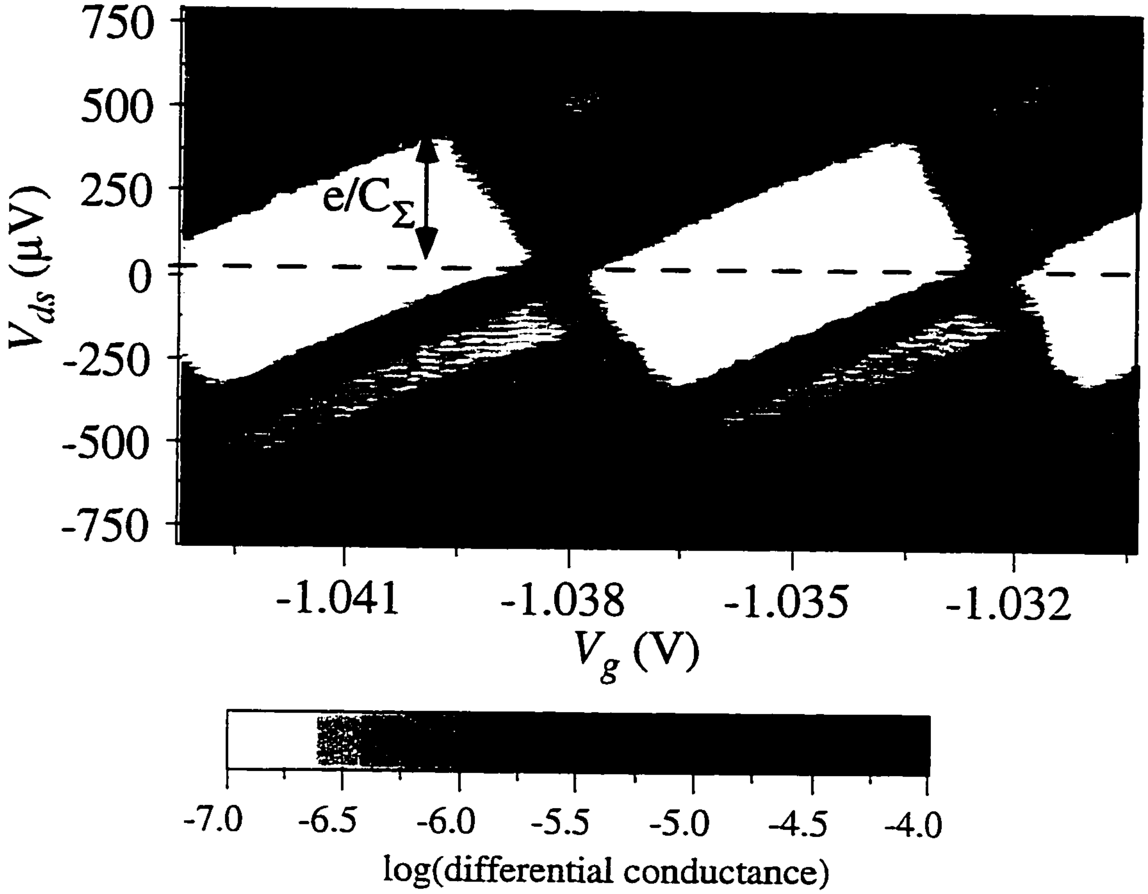

Figure 2.10 Measured differential conductance through a single quantum dot vs. finite drain-source bias and side gate voltage plotted in logarithmic color scale. White indicates low conductance and dark indicates high conductance. Data were measured at base temperature (25 mK). As appears in Crouch [1996a] and Crouch *et al.* [1997].

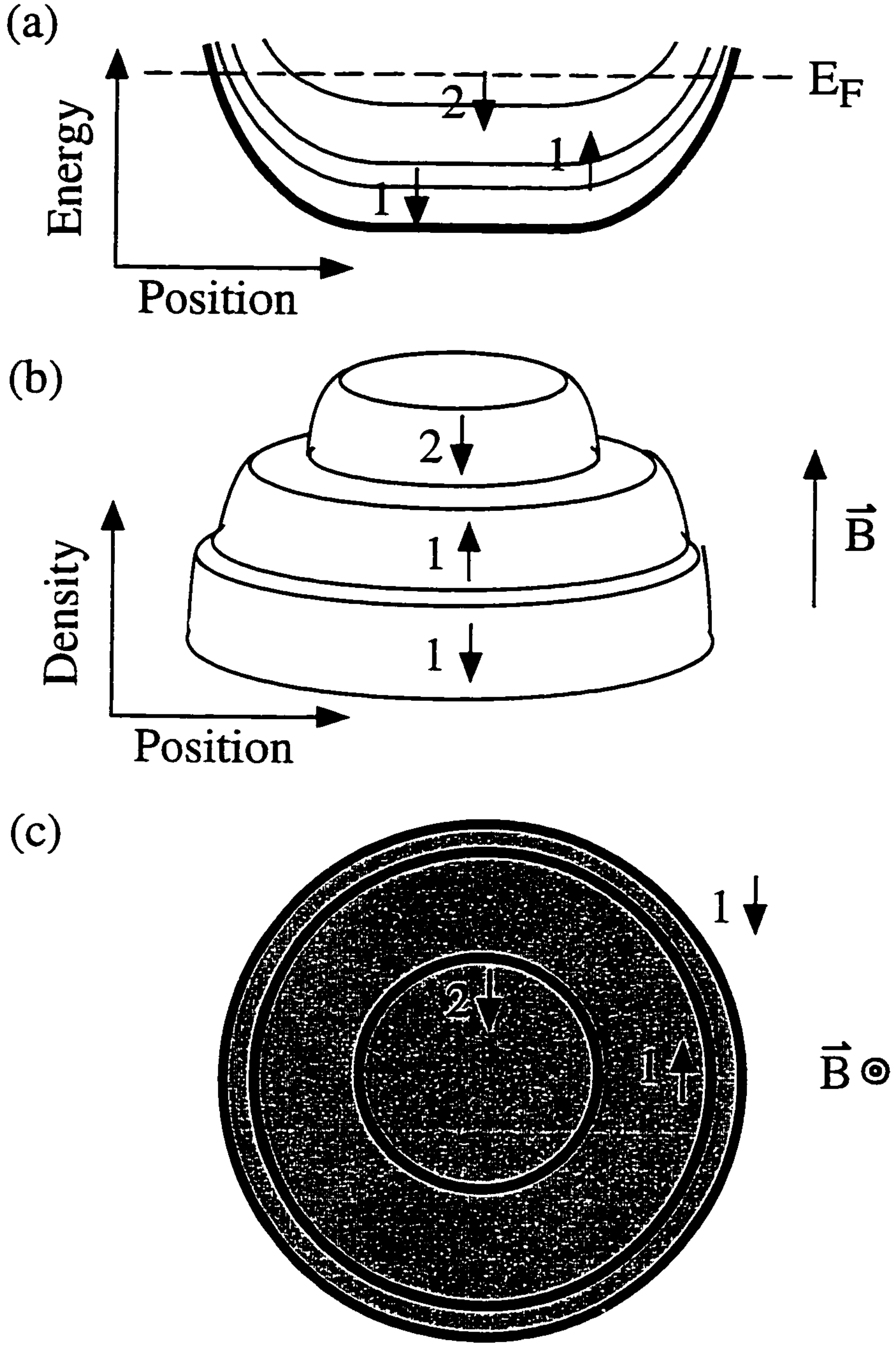

Figure 2.11 (a) Landau level energies of a quantum dot in the $\nu = 3$ regime. Edge states form wherever the states intersect the Fermi level. (b) Schematic diagram of the electron density profile in this regime; layers represent filled (or partially filled) Landau levels. (c) Schematic top view of the quantum dot showing the edge state structure. Edge states are thick lines, and shaded regions contain electrons.

position across a quantum dot. In the center of the dot, the energies are roughly independent of position, as one expects for Landau levels. At the edges of the dot, the energies rise as the confinement energy increases. The bottom two states are split only by the Zeeman energy and hence are closely spaced. The large spacing in energy between the second and third states comes from the inter-Landau level energy spacing. In this diagram, there are three states filled (if you count spins separately), so the filling factor $\nu = 3$. The edge states exist where the energy of a given state crosses the Fermi level. The situation illustrated here has three concentric edge states. Figure 2.11b schematically illustrates the electron density profile in the above described quantum dot. The bottom two layers of the structure are the spin split lowest Landau level. The next Landau level occupies an area nearer the center of the dot. Figure 2.11c is a top view of the dot that shows the resulting edge state structure. Since the outer edge state neighbors the point contact constrictions, transport in and out of the dot occurs via the outer edge state.

Experiments on single quantum dots in the quantum Hall regime have found that the electron distribution in the dot is governed by the complex interplay of electrostatics, confinement energies, and magnetic field and spin effects [McEuen *et al.*, 1991; McEuen *et al.*, 1992; McEuen *et al.*, 1993; Klein *et al.*, 1995; Klein *et al.*, 1996]. This broad range of interactions result in a rich variety of phenomena. The experiments found that when the magnetic field is varied, electrons may be redistributed among Landau levels to minimize the total energy of the system. For example, when an additional flux quantum is threaded through the area of a quantum dot, an electron can be transferred from a higher Landau level to a lower one to complete its occupancy. These depopulation events are marked by a modulation of the Coulomb oscillation height and shift in the peak position. Figure 2.12 shows an example of this behavior for a single quantum dot as measured in the course of our quantum Hall experiments. Conductance is plotted in inverse grayscale, with dark lines indicating high conductance and bright regions indicating low conductance, as a function of side gate voltage V_g on the vertical axis and magnetic field on the horizontal axis. As the magnetic field is swept, each peak undergoes modulations of conductance and position. The period of this modulation is related to the change in magnetic field required to thread additional flux quanta through the dot; the exact period depends on filling factor.

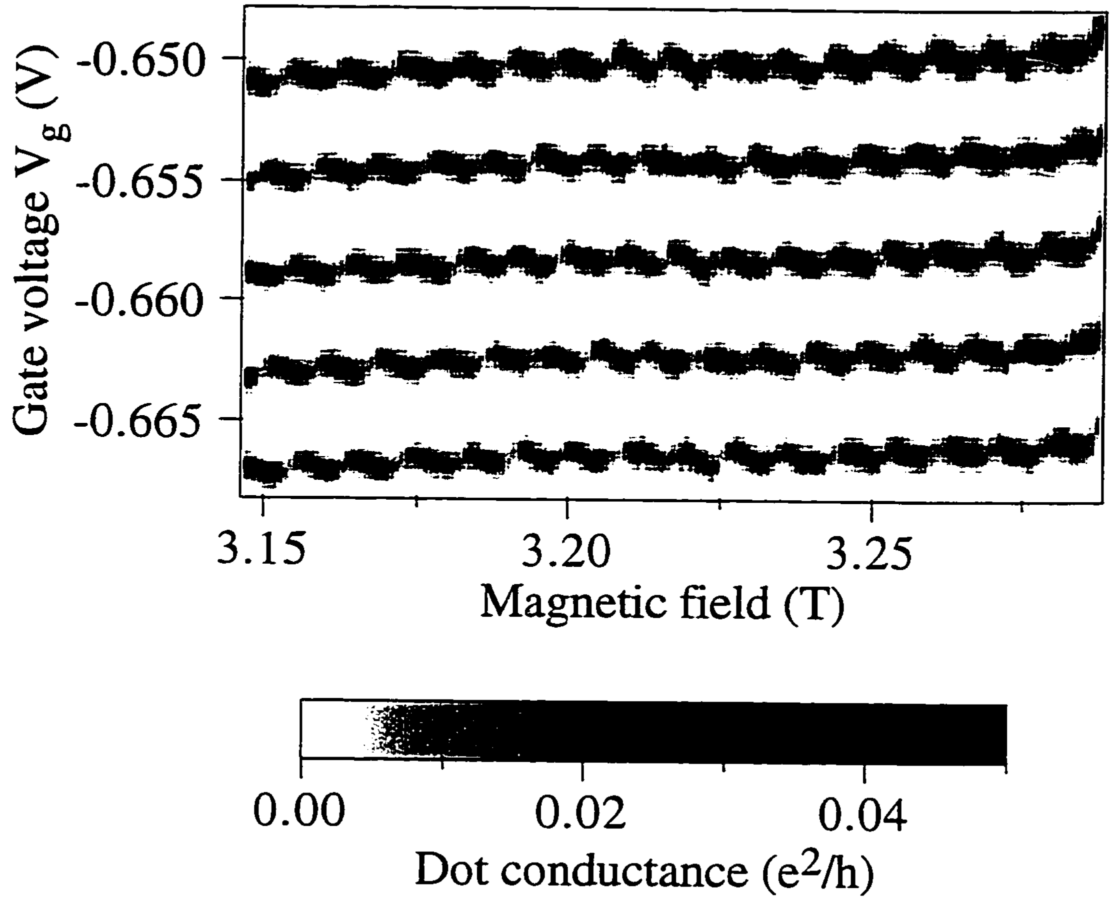

Figure 2.12 Inverted grayscale image of dot conductance as a function of side gate voltage on the vertical axis and perpendicular magnetic field on the horizontal axis, for filling factor $\nu = 3$. As the field increases, electrons shift between Landau levels, changing the peak heights and positions.

Chapter 3

Experimental Techniques

This chapter outlines the techniques we use to fabricate and measure our quantum dot samples. The first half addresses fabrication. After describing pre-cleaning and formation of ohmic contacts to the 2DEG, we discuss the lithographic techniques that produce sub-100 nm features in our samples: resist processing and electron beam lithography. Then we present the metallization and electrical wiring of the devices for measurement.

In the second half, we discuss our cryogenics and our low noise measurement techniques. We briefly describe the dilution refrigerators and magnet used in our experiments and provide a few operating notes. We then discuss our measurement setup, including the automated data acquisition system added a few years ago.

3.1 Wafer preparation

The first steps in fabrication are cleaving a chip from a 2DEG wafer and cleaning it for resist application [Katine, 1996]. Once the chip is cleaved, the underside is marked by a light diagonal scratch with a diamond scribe. Next the chip is cleaned in three steps, all in the fume hood: ten minutes of gentle boiling in a teflon beaker immersed in trichloroethylene (TCE), ten minutes of ultrasonic cleaning in acetone at room temperature, and ten minutes of ultrasonic cleaning in methanol at room temperature. The chip is blown dry with a stream of dry nitrogen gas. If after this process the chips appear clean under an optical microscope, they are ready for resist application for ohmic contacts. These cleaning steps are also repeated before defining surface gates.

3.2 Ohmic contacts

Ohmic contacts are the connections through which current flows in and out of a 2DEG. When I joined the Westervelt group, ohmic contacts were pieces of indium manually pressed onto the chip surface and annealed until the indium diffused down to the electron gas. Indium contacts frequently fail, and their large size wastes valuable wafer space. Indium contacts also cannot be wired with the wire bonder.

We have since adopted the method used in industry: deposit a gold/germanium alloy on the surface and anneal it into the 2DEG [Kulkarni *et al.*, 1985]. Nickel is deposited along with the AuGe alloy to facilitate the diffusion process. Using a recipe obtained from Dave Carter at MIT, Rex Beck and I optimized this process for our 2DEG samples and showed that NiAuGe contacts work as well or better than their indium counterparts. Because the contacts are lithographically defined, they can be smaller and more numerous than indium contacts. They are almost perfectly reliable and do not require testing.

Many of the steps in ohmic contact fabrication are less demanding versions of the procedure for defining surface gates. For brevity, we will emphasize the differences and refer the reader to the complete lithography discussion that appears later in this chapter. Pre-cleaning the chip is vital because grease or residues on the surface degrade metal adhesion and diffusion into the chip. Next a triple layer of electron beam resist is spun onto the surface (PMMA dissolved in chlorobenzene, in layers of 2% molecular weight 496K, 2% 496K, and 2% 950K). The triple layer prevents pinholes in the resist that can cause unwanted microscopic ohmic contacts to the 2DEG. The contact areas are defined using electron beam lithography, and the exposed resist is developed. Immediately before the chip is mounted in the evaporator, it is dunked in a 1:5 solution of ammonium hydroxide and deionized water and blown dry. The ammonium hydroxide removes surface residues that interfere with metal adhesion and diffusion into the chip. The chip is mounted on an evaporation stage with carbon paint. Blemishes in the resist should be covered over with carbon paint to avoid accidental ohmic contacts. Since unwanted ohmic contacts often form on the chip edges, it is wise to paint over all edges that are not supposed to have contacts.

The metal layers (50 Å Ni, 50 Å Au, 250 Å Ge, 450 Å Au, 100 Å Ni, and 400 Å Au) are deposited in the general purpose evaporator. The second, third, and fourth layers form the important alloy. Their proportions are chosen to form a eutectic, an alloy whose composition is such that it has the lowest possible melting point. The final Au layer is a thick bonding pad for wiring the device in the wirebonder. The initial Ni layer helps the eutectic diffuse into the GaAs, and the second Ni layer acts as a cap to separate the eutectic from the bond pad layer.

After deposition, the resist and unwanted metal are lifted off in acetone. Ultrasound should be avoided during liftoff because the film is fragile and ultrasound can distribute metal particles across the surface where they may subsequently become tiny ohmic contacts. It is nonetheless desirable to be sure that all the unwanted metal has lifted off the sample. We compromise by placing the lifted off chip in a fresh beaker of clean acetone and ultrasounding for a few seconds. The sample is annealed immediately after liftoff because the metal/surface interface degrades over time (on the order of days) and will ultimately fail to contact the 2DEG.

The chip is annealed in the strip heater constructed by Alex Rimberg [Rimberg, 1992]. A thermocouple attached to the bottom of the heater strip monitors the temperature. First the strip heater chamber is flushed out for five minutes with forming gas (20% H_2 and 80% He) at 3 psi. With the forming gas still flowing, the sample is heated to 110 °C for 60 seconds to drive off moisture. Next the sample is heated to 250 °C and remains there for 15 seconds to melt the eutectic. The chip is heated to 410 °C for 15 - 25 seconds to anneal it. It is virtually impossible to overbake these contacts; when in doubt, heat them longer. Once the sample returns to room temperature, the forming gas is shut off and the sample is removed and inspected under an optical microscope. If the contacts look like the cratered surface of the moon or like melted pizza cheese, they are successful. Otherwise they need to be baked longer.[1] Once they are baked, the metal film will adhere firmly and the chips may be cleaned in the ultrasound before subsequent processing steps.

3.3 Lithography

Figure 3.1 summarizes the lithographic procedure we use to fabricate our devices. The first two steps are resist application and electron beam lithography, in which we apply a polymer layer to the chip surface and damage portions of the layer with an electron beam. Next come developing and metal deposition, in which we remove the damaged portions of the resist to expose the sample surface and deposit metal on the exposed regions. Finally we lift off the unwanted resist and metal and connect the sample to the measurement apparatus. Each of these steps is described in more detail in the sections that follow.

Spinning resist

We apply electron beam resist to our samples in the Class 100 inner clean room on the second floor of Gordon McKay laboratory. The resists are molecular weight 496 K and 950 K polymethylmethacrylate (PMMA) dissolved in chlorobenzene.[2] These are positive resists; resist that is exposed to an electron beam is removed. The resist is applied in a double layer (for gates) or a triple layer (for ohmic contacts), with the 496K layer(s) on the bottom. This resist structure develops an undercut after exposure and developing because the lower molecular weight resist is more strongly affected by the electron beam and because the bottom layer is doubly exposed when electrons backscatter off the surface. The undercut aids in the liftoff of resist and unwanted metal after metal deposition.

---

[1] A lumpy or uneven surface on the strip heater can translate into some unbaked contacts on the chip. Try putting the sample elsewhere on the heating strip, and bake until all the contacts look good.

[2] PMMA is also available dissolved in anisol. The materials safety data sheet for anisol suggests that it may be preferable to chlorobenzene, and other groups use PMMA dissolved in anisol with success.

(a) Spin e-beam resist (PMMA)

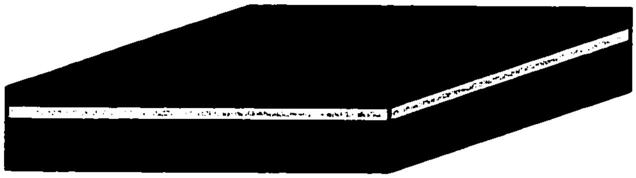

(b) Expose pattern with e-beam

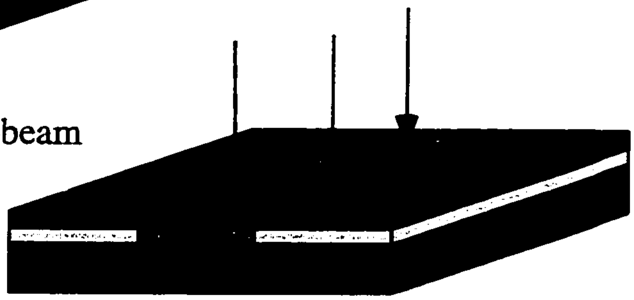

(c) Develop resist

(d) Evaporate metal

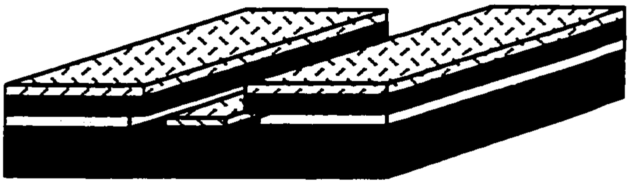

(e) Liftoff

Figure 3.1 Schematic diagram of sample fabrication by electron beam lithography. Adopted from Duncan [1997].

Figure 3.1a is a schematic diagram of a chip with resist layers in place. A summary of the spinning procedure follows.

1) Clean the chips by ultrasounding in acetone and methanol inside the inner clean room; blow dry.

2) Clean the spinner chuck to remove debris that might prevent it from pulling vacuum or keep the chip from lying flat.

3) Draw 496 K PMMA (2% by weight in chlorobenzene) into a clean, dry pipette with a rubber bulb on the end. Do not let resist into the bulb, and do not double-dip, since double-dipping could contaminate the resist supply. Place two drops of PMMA on the chip and spin for one minute at 4000 rpm.

4) Bake the chip on a hot plate at 180 °C for twenty minutes. Avoid exposure to acetone fumes, as these may damage the resist.

5) Repeat steps 3 and 4 with 950 K PMMA for a double layer. For a triple layer repeat twice, first with 496 K and then with 950 K.

6) Inspect the resist layers. A good resist layer is uniform in color, except at the edges of the chip where the resist naturally beads up. Dust particles will appear as specks or as comet-shaped defects in the resist layer. Cleanliness is helpful, but you can live with a startling number of imperfections by noting their locations and placing the pattern's sensitive features elsewhere.

Writing patterns in the scanning electron microscope

Devices are defined by exposing the desired areas of a resist covered chip to an electron beam. The damaged areas are then removed, leaving a mask through which metal may be deposited. Figure 3.1b is a schematic diagram of the damaged resist layers after exposure to the electron beam. At Harvard, a JEOL 6400 scanning electron microscope (SEM) provides the electron beam. The ebeam control is handled by a HP Vectra 500 computer with a Pentium processor, using the Nanometer Pattern Generation System (NPGS) available from J.C. Nabity Lithography Systems (Bozeman MT). The pattern design interface for NPGS is the DesignCad 2D program (American Small Business Machines, Inc., Pryor OK).

E-beam lithography has been extensively described in previous Westervelt group theses [Yang, 1995; Berry, 1994; Katine, 1996; Crouch, 1996]. This thesis will provide a brief outline of ebeam procedures followed by a discussion of helpful techniques for consistently writing the small features that are found in quantum dots.

An abbreviated ebeam lithography procedure follows.

1) Mount the sample with carbon paint on an SEM mount. The sample should be as flat as possible, and the mount should have a deep hole drilled to one side for accurate beam current measurement. Shake tiny flecks of dried Ag paint from a wooden applicator onto the chip edges (away from the pattern location).

2) Load the sample into the SEM and move the sample out of the path of the beam. Load in the appropriate conditions (accelerating voltage = 35 kV for writing, and usually working distance = 15 mm), turn on the accelerating voltage, and saturate the filament. Hit lens clear to eliminate accumulated hysteresis effects.

3) Maximize beam current by adjusting tilt at high condenser lens and shift at low condenser lens. Stabilize the low condenser lens current value by changing from high to low condenser lens several times and then maximizing the current. (This gets the hysteretic effects that cause beam current droop out of the way up front.)

4) Allow beam current to warm up for 15 minutes; recheck maximization; adjust fine condenser lens setting to obtain the same beam current that you always have on the finest condenser lens setting.

5) Straighten chip relative to x and y axes. Find the sample corners. Calculate the sample center and adjust pattern to fit on chip if necessary.

6) Focus on a fleck of Ag paint. Adjust wobbler, focus, and stigma. Focus may vary across the chip; the wobbler and stigma should not. Focus on all four corners of the chip at about x120,000 and average the focus numbers to get an approximate setting for the center of the chip. A minimal focus criterion is that features on the order of the minimal feature size in the pattern should be clear.

7) Measure the beam currents at all condenser lens settings that are called in the run file. Aim the beam into the hole at high magnification and monitor the current that flows into it. It will decline for a few minutes before stabilizing. Adjust the condenser lens fine setting if necessary.

8) Write the pattern with the computer screen off, adjusting condenser lens and magnification settings between layers. Write test patterns. Include the first several layers of the pattern, as the proximity effect from outer layers changes the exposure of the fine features.

Most badly written samples are a result of poor focus; a typical symptom is neighboring gates bleeding together. Poor focus happens when a sample does not lie flat in the SEM, so that the focus varies across the chip. The primary remedy is four-corner interpolative focusing, in which the focus is measured on each corner and averaged to obtain an appropriate value for the center, where the fine features will be. Another remedy is prudent sample design. Neighboring gates should not be placed any closer to one another than is absolutely necessary; since the depletion length is significant, electrons will not leak out between the gates.

Other techniques ensure that the sample lies flat in the first place. Sometimes the sample tips up when it is painted onto the SEM mount. Using runny carbon paint and applying it quickly to both sides of the chip minimizes this problem. The mounted sample may be held up to the light or inspected edge on under a microscope to determine whether it lies flat. It also helps to be careful when clamping the SEM mount into the sample holder (to prevent tipping) and to use minimal resist when spinning so that it does not seep beneath the chip and make the underside lumpy.

Another common problem is beam current drift, in which the current declines while the pattern is being written. Part of the problem is hysteresis, and one successful solution is to get the hysteresis out of the way early on. When maximizing the beam current, do not stop when the low condenser lens value first shows its maximal current. Cycling from low to high condenser lens a few times will cause it to decline. To deal with this problem, cycle the beam current from high to low, then maximize it, then repeat until cycling leaves the beam current reasonably constant. At this point, the microscope has settled onto a predictable hysteresis loop, and predictability is the key to e-beam writing success.

3.4 Metal deposition

Next we develop the pattern and deposit metal gates on the sample. The chip is immersed for 60 seconds in a developer that washes away exposed resist and leaves a resist mask like a stencil on the chip surface. The developing solution is a mixture of 375 ml isopropanol, 125 ml methyl isobutyl ketone (MIBK), and 6.5 ml methyl ethyl ketone (MEK). The developed chip is immediately immersed in either isopropanol or methanol to quench the developing, spritzed with the solvent, and blown dry with nitrogen gas. The pattern is then inspected for defects under an optical microscope. Any unfortunately placed debris may be removed by ultrasounding for a few seconds in isopropanol. The result is shown schematically in Figure 3.1c.

The chip may optionally be dipped in an ammonium hydroxide solution (5:1 $H_2O:NH_4OH$) right before the metal gates are deposited on the surface. Steve Shephard suggested this step to promote metal film adhesion by cleaning off surface scum. The sample is immersed in the ammonium hydroxide for a second or two, removed promptly, and blown dry with nitrogen gas.[3] I recommend using the dip for ohmic contacts but omitting it for surface gates, unless wirebonding to the surface gates is difficult.

---

[3] Another technique that future students can try, though I have not, is the oxygen plasma descum.

We deposit the metal layers that form ohmic contacts or surface gates next. Surface gates are deposited in the new cryopumped thermal evaporator (Key High Vacuum Products, Neponset NY). The samples are mounted on the stage with carbon paint, and the stage is installed upside down above the metal sources. About 50 A to 100 A of Cr are deposited first; Cr is sticky and adheres well to GaAs. This is followed by about 300 A of Au. The layer should be thick enough to wirebond to but thinner than the resist layers. Figure 3.1d is a diagram of a chip after metal deposition. Although metal coats the entire surface, it only touches the sample itself in the regions where the resist has been developed away.

The chip is soaked in acetone overnight to loosen the remaining resist and unwanted metal. Time is the best liftoff tool; acetone slowly leaks into the crevices between the metal on the surface and the leftover resist. In the morning, human intervention speeds the liftoff. The chip is ultrasounded for a few seconds in the acetone and visually inspected. The ultrasound is repeated for progressively longer intervals until liftoff appears complete. Once the extra metal is gone, the chip is rinsed in methanol and blown dry with nitrogen gas. The chip should now be handled only with metal tweezers to prevent destructive static buildup and discharge. It is also helpful to hold the chip by the ohmic contact edges and avoid the gates.

It is wise to keep the ultrasound to a bare minimum because it can knock gates off the surface. If liftoff is difficult, the chip may be subjected to ultrasound for long periods of time; when the metal doesn't lift off, there is not much to lose. Although I have lost chips to ultrasound damage, I have also left chips in ultrasound for hours with no apparent harm.

3.5 Sample wiring

Wirebonding

After liftoff, the chip is wired. The Kelvinox 100 accepts chips wirebonded to a chip carrier (Jade Corp., Part #28M270-J-060-U-06-4); the carrier is inserted into a socket (AMP Corp., Part #641444-2) in the bottom of the fridge. Figure 3.2 is an SEM photograph of a chip wirebonded into a chip carrier for use in the Kelvinox. When everything is working, wirebonding is quick and painless. A clean chip is affixed to a chip carrier with a thin layer of GE varnish (General Electric Co., Schenectady, NY), and the toxic varnish is allowed to dry in the fume hood. The sample should not be affixed to the carrier with carbon tape because carbon tape loses its stickiness on thermal cycling, and chips fall off the chip carrier. The chip carrier is held in a grounded socket during bonding to maintain all of the leads at the same potential. The wirebonder (Kulicke-Soffa Model 4123) must also be held at ground potential, with the bonding head, the surface on which the sample sits, and the grounding wire of the socket attached to a common ground point with alligator clips. The wirebonder procedures are described in the manual and highlighted in Jordan Katine's thesis [1996].

It is extremely uncommon for samples to blow up in the wirebonder if proper ground connections have been made. For additional protection, it is prudent to wire an ohmic contact first. A common problem is broken wirebonds. Dave Duncan's highly effective brute force technique of making each wirebond in duplicate or triplicate solves that problem.

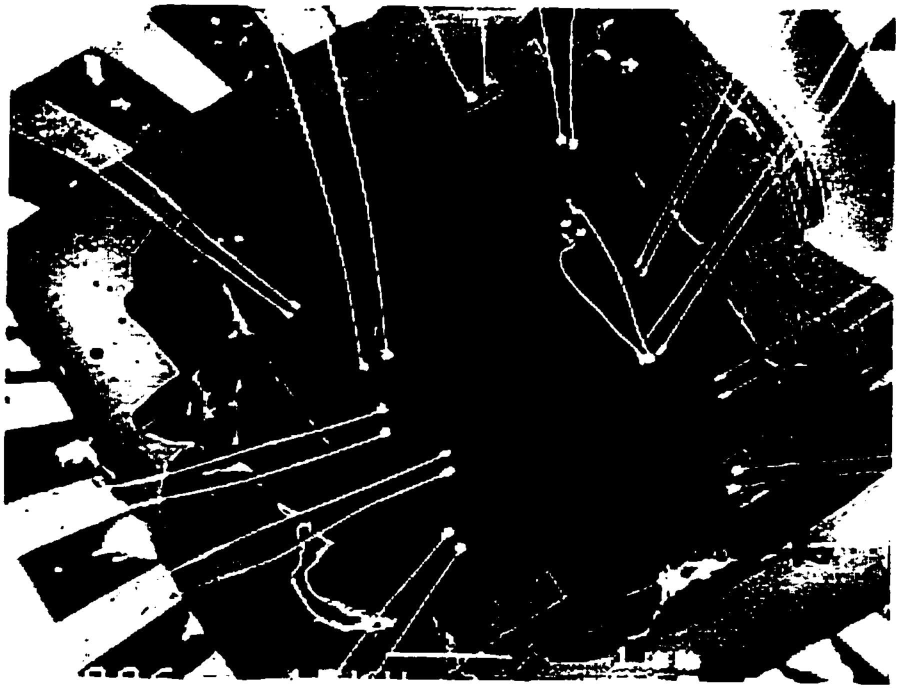

Figure 3.2 Scanning electron micrograph of a completed chip mounted and wirebonded in a chip carrier.

Indium wiring

Samples are hand wired into the top-loading dilution refrigerator by pressing gold wires into blobs of indium. As of this writing, it appears that the top-loader will be scrapped, but indium wiring remains a useful skill to have. It is good for repairs and for wiring samples whose gate pads peel off in the wirebonder. We describe indium wiring here for the above reasons and so that the knowledge is not lost.

Indium wiring is more an art than a technique. The trickiest part is protecting the sample from destructive static discharges. A second challenge is arranging to dunk test the wired sample in a liquid helium storage dewar before loading it into the fridge. The process described here is an adaptation of Catherine Crouch's wiring procedures that addresses both issues [Crouch, 1996a].

We begin with an overview. Working at a grounded station, the sample is hand wired to a piece of PC board (known as a "D") that has been hand wired to a chip carrier inside a grounded socket. The sample is dunk tested at helium temperatures by removing the chip carrier from the grounded socket and inserting it into the socket on a test rig. After the dunk test the D is removed from the chip carrier and wired into the fridge slug. Alternatively, the entire carrier may be plugged into either the Kelvinox or the ^{3}He system. This Byzantine wiring scheme provides good protection against static discharge and the modularity to measure a sample in different cryogenic apparatuses.

A detailed description of the author's indium wiring techniques follows.

1) Make a printed circuit board to serve as a D [Eriksson, 1996]. The D has metal pads arranged in an L shape around the space that holds the sample. Solder indium blobs to the metal pads. Scrape off the dirty indium caps with a scalpel and cover with fresh indium. Clean in acetone.

2) Clean the sample and tools in TCE, acetone, and methanol immediately prior to wiring.

3) Rubber cement the D into a chip carrier. Run 0.1 mm gold wire between the indium pads on the D and indium blobs pressed onto the chip carrier contacts. Place the chip carrier in a grounded socket. Ground yourself, the tools, the socket's ground wire, and the aluminum sheet metal work surface. Wear cotton clothing and turn on the humidifier to reduce static.[4]

4) Mount the sample on the D.[5]

5) Apply indium blobs to the ohmic contact and gate pads. This is the most dangerous step because if indium is ripped off the sample surface by a sticky tool, the sample may be destroyed. First wipe each clean tool across the back of your wrist to apply a fine layer of grease and reduce the tool's stickiness. Hold a piece of indium wire with a pair of tweezers and cut away the indium surface with a scalpel to reveal fresh, clean indium. Cut off a small piece of indium; it should stick to the scalpel. Invert the scalpel and press the indium clean side down on a contact pad using the scalpel and a dental probe. Begin with the ohmic contacts and then proceed to step six.

6) Using tweezers and a dental probe, press one end of a 0.05 mm wire into the indium blob on the contact pad. Press the other end into an indium blob on the D. Once the ohmic contacts are wired, repeat steps five and six for the gate contact pads.

7) Dunk test the sample by inserting the chip carrier into a socket on the test rig. If you're using the Kelvinox refrigerator, load the chip carrier into the socket and proceed. (You also should have used the wirebonder.)

8) Wire sample into the sample mount (i.e. the old fridge slug). First return the chip carrier to the grounded socket with the above precautions. Ground the slug by resting its contact rings in copper gauze. Redundantly short the contacts on the D with a 0.1 mm gold wire. Press 0.1 mm wires into the contacts on the D; they should be long enough to reach from the D to the indium blobs in the fridge slug.

---

[4] Graduate student lore also requires that the wirer remove his/her shoes (to connect human to grounded floor mat) and listen to classical music (for its calming and stabilizing effects).

[5] The author has used carbon tape as an adhesive when mounting the sample to the D. It might be wiser to use GE varnish, which never comes off.

Unwire the D from the chip carrier. Rubber cement the D into the fridge slug. Connect the 0.1 mm wires to the indium blobs in the slug. Remove the wire that shorts the D and close up the slug.

3.6 Dilution Refrigerators

In chapter 2 we observed that the temperature must be much less than the charging energy $U_C = e^2/2C_\Sigma$, or about 2 K for our samples. We use dilution refrigerators to achieve temperatures of about 25 mK. [For details, see for example Lounasmaa, 1974]. Our systems have been described in detail in previous theses [Adourian, 1996; Katine, 1996; Hergenrother, 1995; Tighe, 1993] , so our discussion with focus on recent changes and operating notes.

Oxford 200 top-loading dilution refrigerator

Two dilution refrigerators were used for the experiments described in this thesis. The top-loading Oxford 200 dilution refrigerator, installed in 1983, was used for the experiments described in chapter 4. Details may be found in the Oxford manual and in previous theses [Hergenrother, 1995; Tighe, 1993]. As of this writing, the top-loader has a persistent leak from the He bath to the IVC, and it is not clear how much of the system will be salvaged. We will describe the system anyway, and time will tell whether the comments are operating notes or a postmortem.

When functioning, the top-loading dilution fridge has many advantages. The user can change samples while the fridge is cold, with any luck keeping the mixing chamber below 1 K. The turnaround times can be faster in this refrigerator than in the Kelvinox system. When everything proceeds smoothly, an old sample can be removed and a new one brought to base temperature in about eight hours.[6] The Oxford 200 also has twice the cooling power of the Kelvinox 100 (200 μW at 100 mK, compared with 100 μW at 100 mK). The sample wiring is reliable and has good radiation shielding. Since the system is top-loading, the innards are inaccessible and difficult to destroy.[7]

The top-loader also has disadvantages beyond being broken at present. It takes longer to cool down than the Kelvinox, as the outer vacuum can must be pumped out before each cooldown. It also uses more helium, averaging about 20 liters/day to the Kelvinox's 15. There is a leak from one part of the room temperature circulation path to another, probably across valve 5. The system resembles an old car, breaking down in little ways as it proceeds down the highway. Top-loading also requires the use of the office directly above the fridge room, so we rarely achieve the fast turnaround times that are theoretically possible.

Kelvinox 100 dilution refrigerator

The Kelvinox 100, installed in 1993, was used for the high magnetic field measurements described in Chapter 5. Details may be found in the Oxford manual and in previous theses [Adourian, 1996; Katine, 1996]. The Kelvinox achieves a base temperature of about 30 mK. Its magnet (American Magnetics Inc., Oak Ridge, TN) is rated to 7 T and supposedly quenches at 8.4 T with a bath temperature of 4.2 K, a fact that remains unverified by this author. The magnet produces 0.2609 T/A of magnet current and is equipped with a persistent current switch. Protection circuitry integrated into the magnet takes over in case of a quench.

The magnet supports have been problematic. The magnet insert hangs inside the dewar. The magnet itself is supported by three long metal rods that have threaded holes at

---

[6] The eight hour estimate assumes that the top-loads go well and that the occupant of the upstairs office does not object to having his peace repeatedly shattered by vacuum pumps and experimentalists.
[7] Unfortunately, the innards are also difficult to fix.

the bottom. The magnet attaches to the supports by screws that thread upwards into the rods. The screws tend to loosen when the dewar is moved around the screen room, and the magnet has come loose from as many as two of its supports at a time.

When the magnet comes loose, the insert gets stuck on a solid object, harder than ice, on its way into the dewar. That solid object is the magnet hanging at a rakish angle. It is wise to watch for early warning signs, when the insert starts to catch on the magnet but manages to find its way down. The solution is to remove the magnet insert carefully with the crane, being careful not to break the remaining supports. The magnet supports are then reattached and the system reassembled. We included lock washers in the last repair; hopefully this will help.

We power the magnet with either the Oxford magnet supply or the remotely controllable Kepco BOP 20-20 bipolar power supplies (Kepco, Flushing, NY). The BOP 20-20 supplies a large, continuously variable magnet current that is suitable for varying the magnetic field over large or small ranges. Each BOP 20-20 can supply up to ±20 A of current, and the output current may be controlled by an external voltage. Multiple BOP 20-20s may be connected in a parallel master-slave configuration to achieve higher currents (two supplies = 40 A, three supplies = 60 A). We monitor magnetic field by measuring the voltage across a precision 0.097 Ω power resistor in series with the magnet.

3.7 Electronics

Measuring transport through quantum dots means detecting picoAmp currents and varying experimental parameters on the microVolt level. Our electronics include a low noise current measurement circuit and a few different low noise voltage sources. This section describes our two most common measurement setups.

Our simplest, most reliable technique for monitoring conductance through quantum dots uses a battery powered, analog circuit known as a ramper box to output the constant and variable voltages with which we energize the electrostatic gates that define our quantum dots. Our first ramper box was built by Jordan Katine, and the circuit is described in his thesis [Katine, 1996]. A small ac bias voltage (usually 5 to 10 μV) is applied across the sample, and current through the sample is measured as a function of a variable voltage output by the ramper box. The current is amplified by an Ithaco 1211 current preamplifier. The resulting signal is amplified using lock-in detection, measured on a Fluke digital voltmeter, and transferred through a GPIB interface to a Power Macintosh computer. The data are recorded in a Labview program called "Read N DMMs" [Mar, 1994].

Advantages of this system are that it is electrically quiet, simple, and easy to use. A disadvantage is that it is slow, measuring one to three data points per second. A more serious drawback is that it is painfully inconvenient to measure a quantity as a function of two or more parameters. The ramper box will vary one parameter; the other must be incremented by hand. Even a routine measurement like a complete current-voltage characteristic on a quantum dot can take five hours, and the frequent charging events may not leave the sample in one charge configuration long enough to measure it.

Figure 3.3 is a schematic diagram of the second measurement setup, which uses an automated system known as the "fast data-taker" to measure up to eight experimental parameters as a function of two voltages varied in a raster pattern by computer. The output comes from two AD1139K 18-bit D/A converters (Analog Devices, Norwood, MA) that are external to the computer and are driven by a NB-DIO-32F digital output board (National Instruments, Austin, TX). The resulting current is detected as described above. The parameters to be measured are read by direct 16-bit A/D conversion using a multipurpose NB-MIO-16XL-18 data acquisition board (National Instruments Corp., Austin, TX). The inherent speed of the MIO-16XL-18 is 55 kHz; in practice, the speed of operation is limited by the rest of the circuit. With a lockin amplifier in the circuit, the fast data-taker takes one point every 10 to 30 ms. This reduces the aforementioned five hour measurement to as few as ten or fifteen minutes.

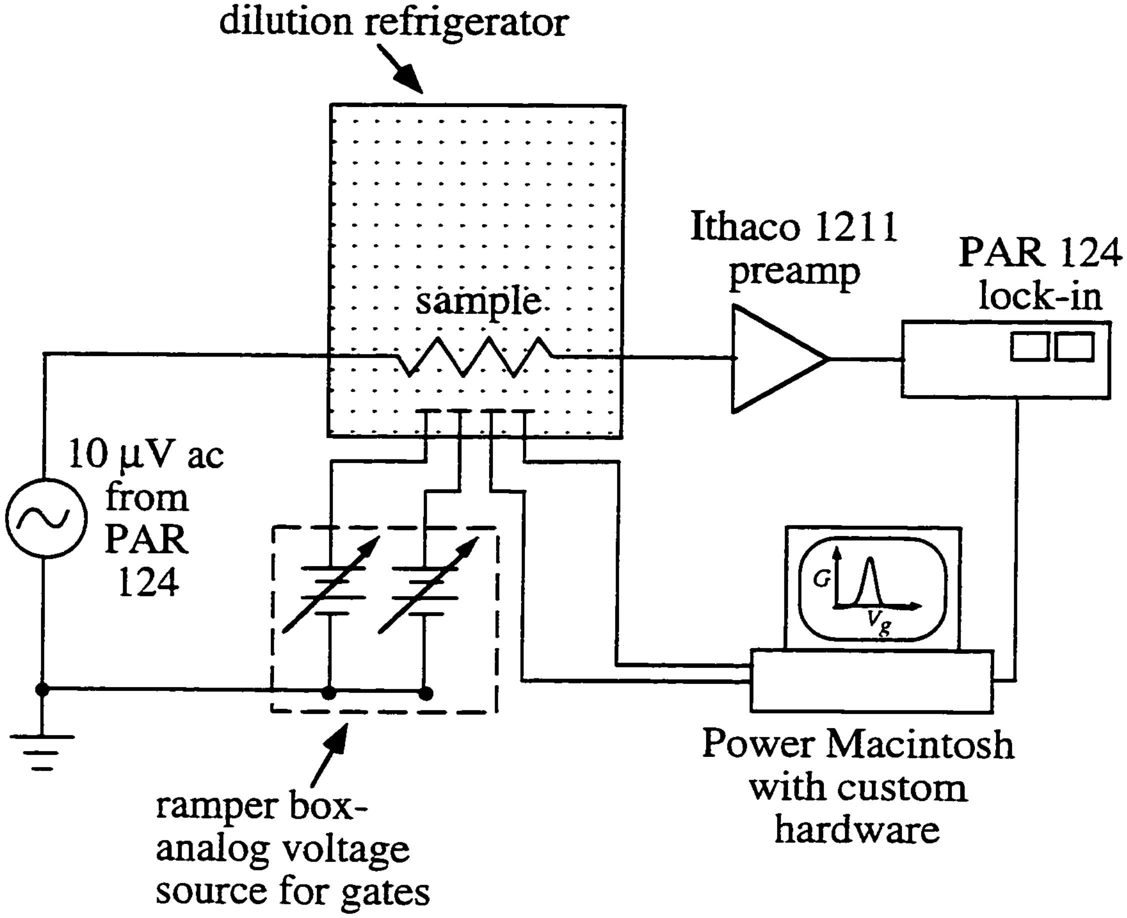

Figure 3.3 Schematic diagram of measurement setup. The sample is cooled in a dilution refrigerator. The current through the sample is monitored as a function of variable parameters such as side gate voltages. The variable parameters are put out either by a battery powered, analog ramper box or by computer controlled D/A conversions. The signal is measured using lockin detection and is recorded either by multimeters via GPIB interface or by direct A/D conversion.

Figure 3.4 is a schematic diagram of the fast data-taker's hardware. The MIO-16X produces a timing signal each time it samples the input channels. The timing signal triggers the DIO-32F to write values to the D/A converters' pins. Once the values are written, the DIO-32F emits an acknowledge pulse that triggers one of the D/A converters to read its inputs. A separate signal triggers the second D/A converter when it is time to move to the next sweep of the raster scan. Further details may be found in Appendix A.

The fast data taker was designed with external D/A converters because we need high output resolution. In order to see Coulomb oscillations clearly, we must be able to sweep a gate voltage with resolution of less than 50 μV on top of a background of order one volt. National Instruments does not sell a data acquisition board with greater than 12-bit output that meets our needs. Twelve bits spread out over 20 V gives a hopelessly inadequate digitization step of 4.9 mV. Eighteen bits is much better, providing a resolution of 76 μV on top of a signal that varies from -10 V to +10 V.

For future generations of fast data-takers, students may wish to use the 12-bit outputs built into the MIO-16X and other compatible boards. These outputs could be divided down (to get the full benefit of the 4096 digital increments) and summed onto a background voltage using summing amplifiers. This system might be more robust because the bulk of the hardware would be inside the computer. The 12-bit approach would only be appropriate if the stability of the output were adequate.

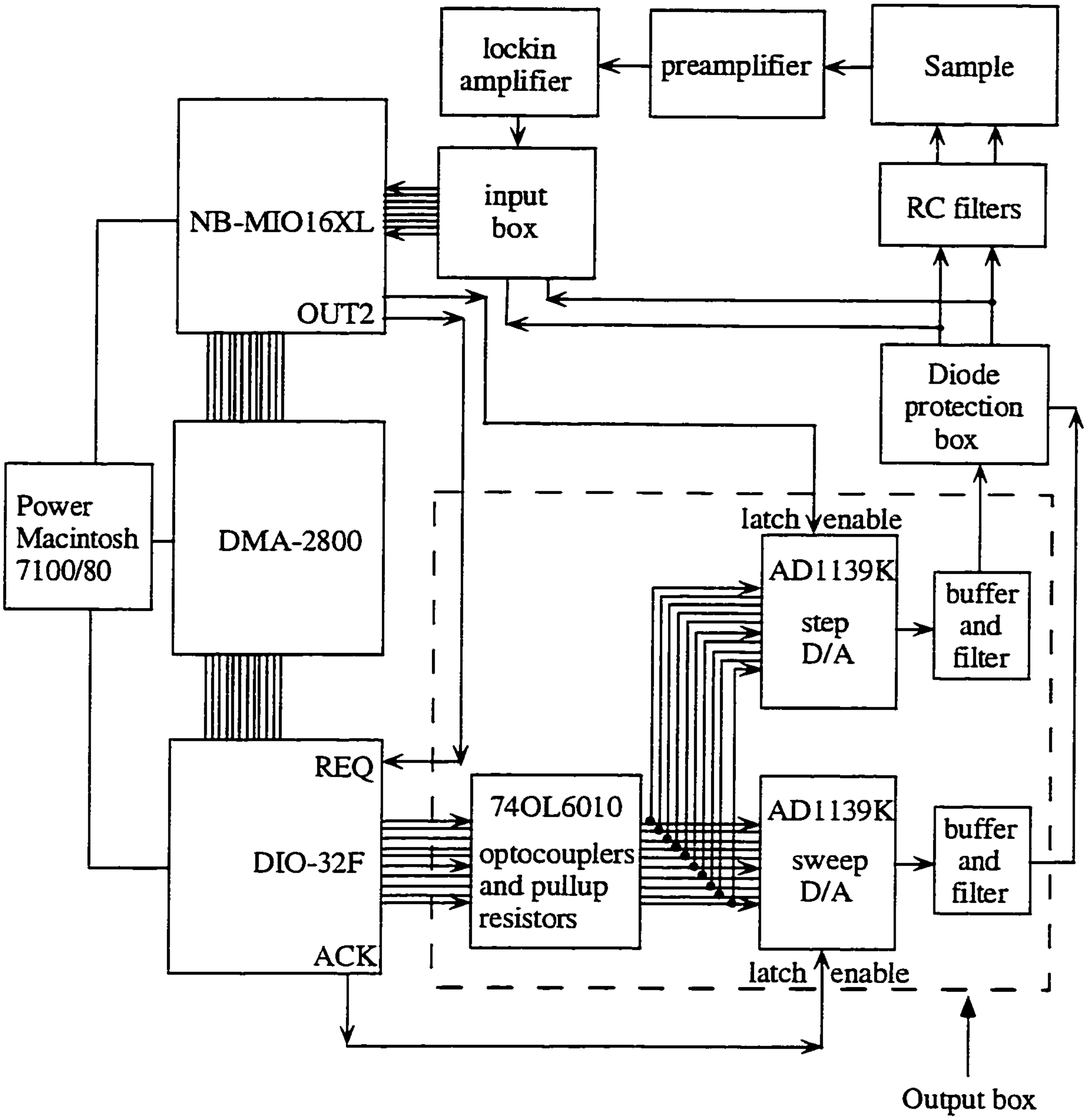

Figure 3.4 Schematic diagram of the computer controlled data acquisition system known as the "fast data-taker". The Power Macintosh controls a digital board (DIO-32F) that drives external D/A converters. The multifunction board (MIO16XL) does A/D conversion and synchronizes output with data acquisition. The system measures up to 8 channels as a function of two 18-bit outputs.

Chapter 4

Tunnel-Coupled Quantum Dots

This chapter presents experiments that use the Coulomb blockade as a spectroscopic tool to probe the ground-state configuration of charge in two tunnel-coupled quantum dots with adjustable interdot tunneling. In these measurements we independently control the induced charge on each dot and the interdot tunneling rate to cover the full three-dimensional parameter space and allow explicit comparison with theory. Previous work [Waugh *et al.*, 1995; Van der Vaart *et al.*, 1995a; Van der Vaart, 1995b; Blick *et al.*, 1996] has tested aspects of the theory by sampling two-dimensional cuts through the parameter space; other experiments have examined different configurations of quantum dots [Crouch *et al.*, 1996b; Adourian *et al.*, 1996a; Hofmann *et al.*, 1995; Molenkamp *et al.*, 1995; Dixon *et al.*, 1996; Kemerink *et al.*, 1994]. Much theoretical work has also been done to describe the physics of these devices [Matveev *et al.*, 1996a; Golden *et al.*, 1996a; Golden *et al.*, 1996b; Matveev *et al.*, 1996b; Ruzin *et al.*, 1992; Klimeck *et al.*, 1994; Stafford *et al.*, 1994]. The measurements described here present a unified picture of how the coupled dot system evolves from the weak tunneling regime, in which capacitive coupling is dominant, to the strong tunneling regime, in which interdot tunneling dominates, including the effects of interdot polarization. This evolution is analogous to the formation of an artificial molecule from two initially separated artificial atoms, and the experiments measure the analog of a molecular binding energy.

We begin by describing the device and characterizing its constituent parts. We then calculate the Coulomb blockade electrostatics of the system and discuss how interdot electron tunneling affects the energy. Next we present conductance measurements that detail the evolution from two separate dots to one large, composite dot. Finally, we describe how these results compare with the theories of Golden and Halperin [1996a; 1996b] and of Matveev, Glazman, and Baranger [1996a; 1996b].

4.1 Double dot device and characterization

Figure 4.1a is a scanning electron micrograph of a double dot device. The device is composed of ten independently adjustable electrostatic gates on the surface of a GaAs/AlGaAs heterostructure wafer; the gates define two quantum dots in the underlying 2DEG. The quantum dots are connected in series with each other and with two current leads, and each dot is capacitively coupled to the surface gates. Figure 4.1b is a schematic diagram of the device wiring for these experiments. The side gate voltages V_{g1} and V_{g2} are varied during the experiment to induce charges on the quantum dots; they are coupled to their respective dots by capacitances C_{g1} and C_{g2}. The center point contact voltage V_{qpc2} sets the amount of electron tunneling between the dots. The data in this chapter come from the device KC7EE; the behavior reproduces in the other double dot devices we have studied.

Figures 4.2a - c plot the point contact conductances G_{qpc1}, G_{qpc2}, and G_{qpc3} vs. V_{qpc1}, V_{qpc2}, and V_{qpc3} respectively, showing clear quantized step structure. These were measured at base temperature (25 mK) in the Oxford dilution refrigerator. Figure 4.3 is a close-up view of the lowest step of the center point contact conductance G_{qpc2} vs. V_{qpc2} under three different conditions: alone; with the side gates V_{g1}, V_{g2}, and V_{g3} energized; and with the side gates energized and the outer point contacts V_{qpc1} and V_{qpc3} energized just to depletion. Note that energizing additional gates shifts the G_{qpc2} characteristic laterally to less negative V_{qpc2} values because distant gates deplete the 2DEG in the constriction slightly. A second effect of energizing the other gates is that the measured conductance includes the series resistance of the other constrictions. Also note that the conductance G_{qpc2} is enhanced near the pinch off point when other point contact

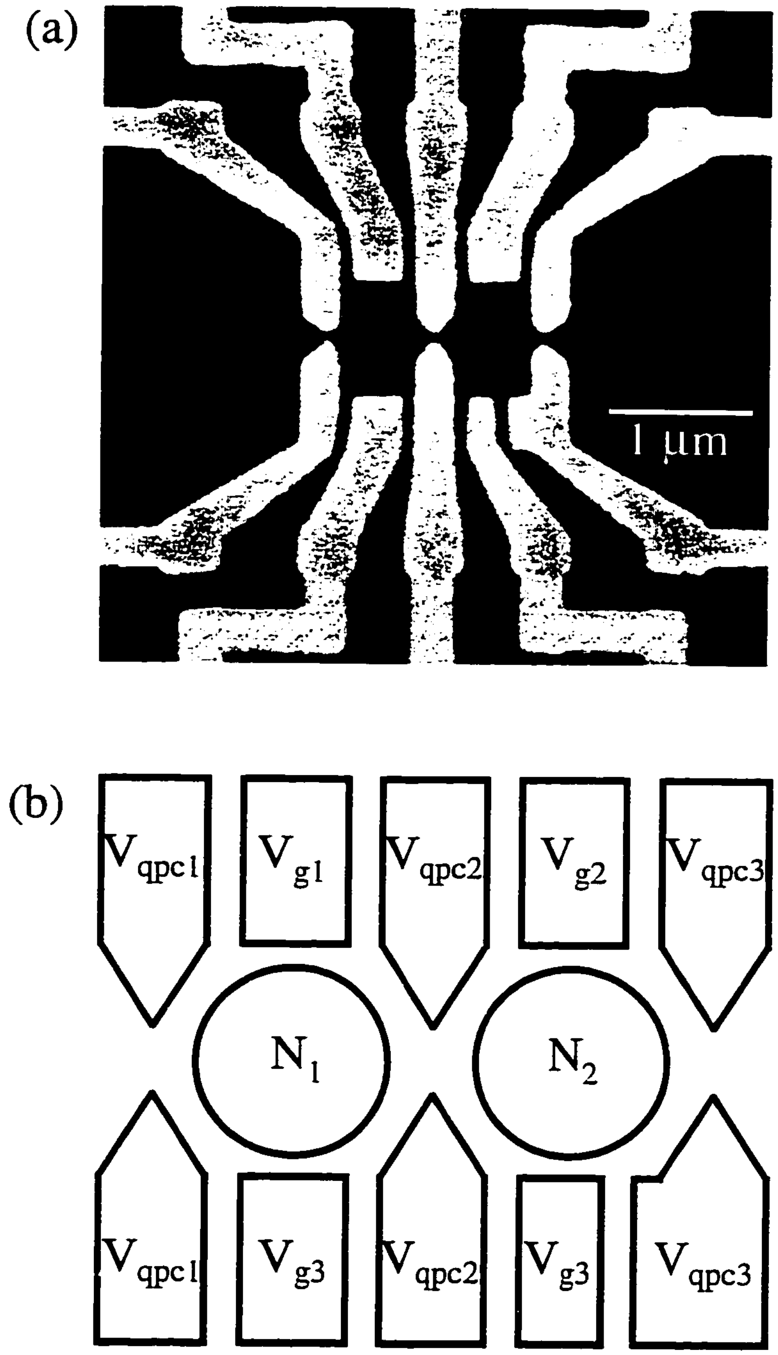

Figure 4.1 (a) Scanning electron micrograph of double quantum dot device. Light regions are electrostatic surface gates, and dark regions are the wafer surface. (b) Wiring diagram of double quantum dot device.

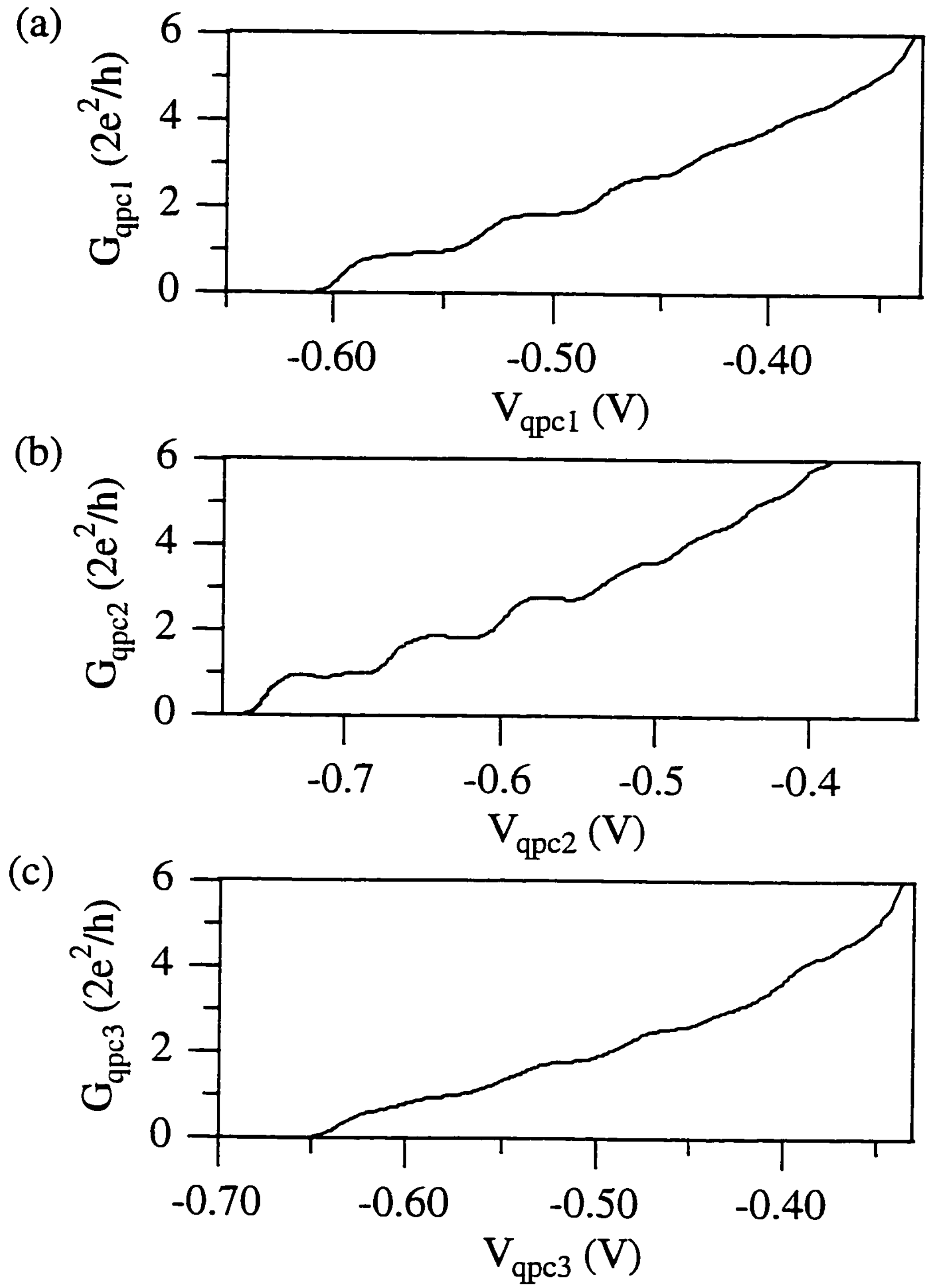

Figure 4.2 Point contact conductance vs. voltage applied to the point contact gate for point contacts (a) one, (b) two, and (c) three of device KC7EE.

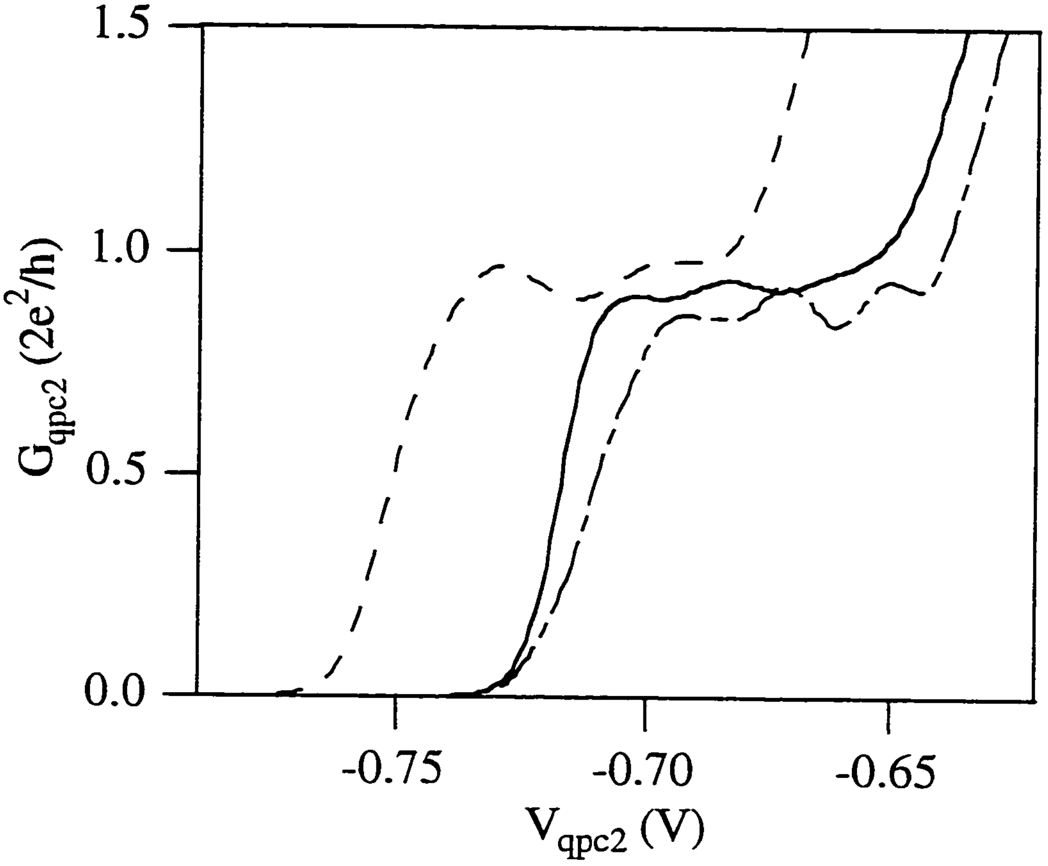

Figure 4.3 Center point contact conductance plotted vs. voltage applied to center point contact gate under three different circumstances. Dotted line is the point contact characteristic measured alone; solid line is the point contact characteristic measured with the side gates energized to approximately experimental values (-0.650 V); dot-dashed line is the point contact conductance measured with the side gates energized to experimental values and the outer point contacts energized just to depletion (-0.300 V).

constrictions are energized in series with it because of collimation of current in a point contact [Wharam *et al.*, 1988; Beton *et al.*, 1989; Beenakker *et al.*, 1989]. A second effect of the outer point contacts is the enhanced oscillations on the first conductance plateau; we associate these with interference. We use these measurements to calibrate G_{qpc2} vs. V_{qpc2} under near experimental conditions. We subtract the series resistance of the other constrictions from our measured resistance and add an additional lateral shift toward more positive V_{qpc2} to account for the effects of bringing the other gate voltages to their actual experimental values.

Figure 4.4a is a plot of the conductance through dot 1 as a function of side gate voltage V_{g1}. The period of the Coulomb oscillations yields a gate capacitance $C_{g1} = 34 \pm 2$ aF for dot 1. Figure 4.4b plots the conductance through dot 2 as a function of side gate voltage V_{g2}. The measured gate capacitance is $C_{g2} = 35 \pm 2$ aF: C_{g1} and C_{g2} are well matched.

4.2 Energetics

Electrostatic model

In our discussion of the Coulomb blockade in single quantum dots, we calculated the electrostatic energy of a dot from a capacitive circuit model. We use the same technique to understand double quantum dots with near-zero interdot tunneling, modeling the double dot as a circuit of capacitors and tunnel junctions and calculating the electrostatic energy. This approach does not include the effects of interdot electron tunneling, but it provides a convenient starting point.

Figure 4.5a is a diagram of the double dot equivalent circuit for the case of near-zero interdot tunneling, when all point contacts are in the tunneling regime. The circles again represent the quantum dots; the coupling of dots to leads and the interdot tunneling are

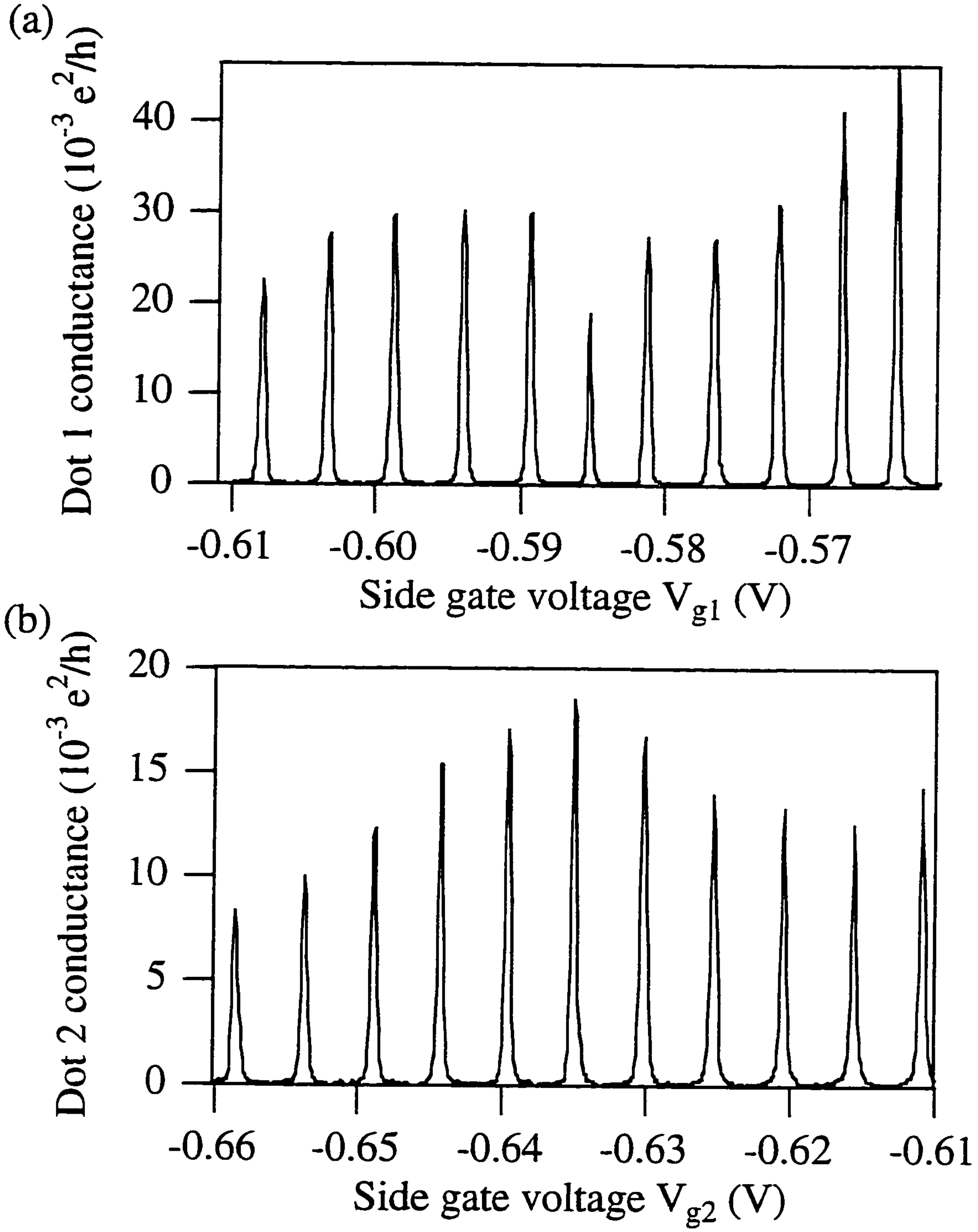

Figure 4.4 (a) Conductance of dot 1 plotted vs. side gate voltage V_{g1}. (b) Conductance of dot 2 plotted vs. side gate voltage V_{g2}.

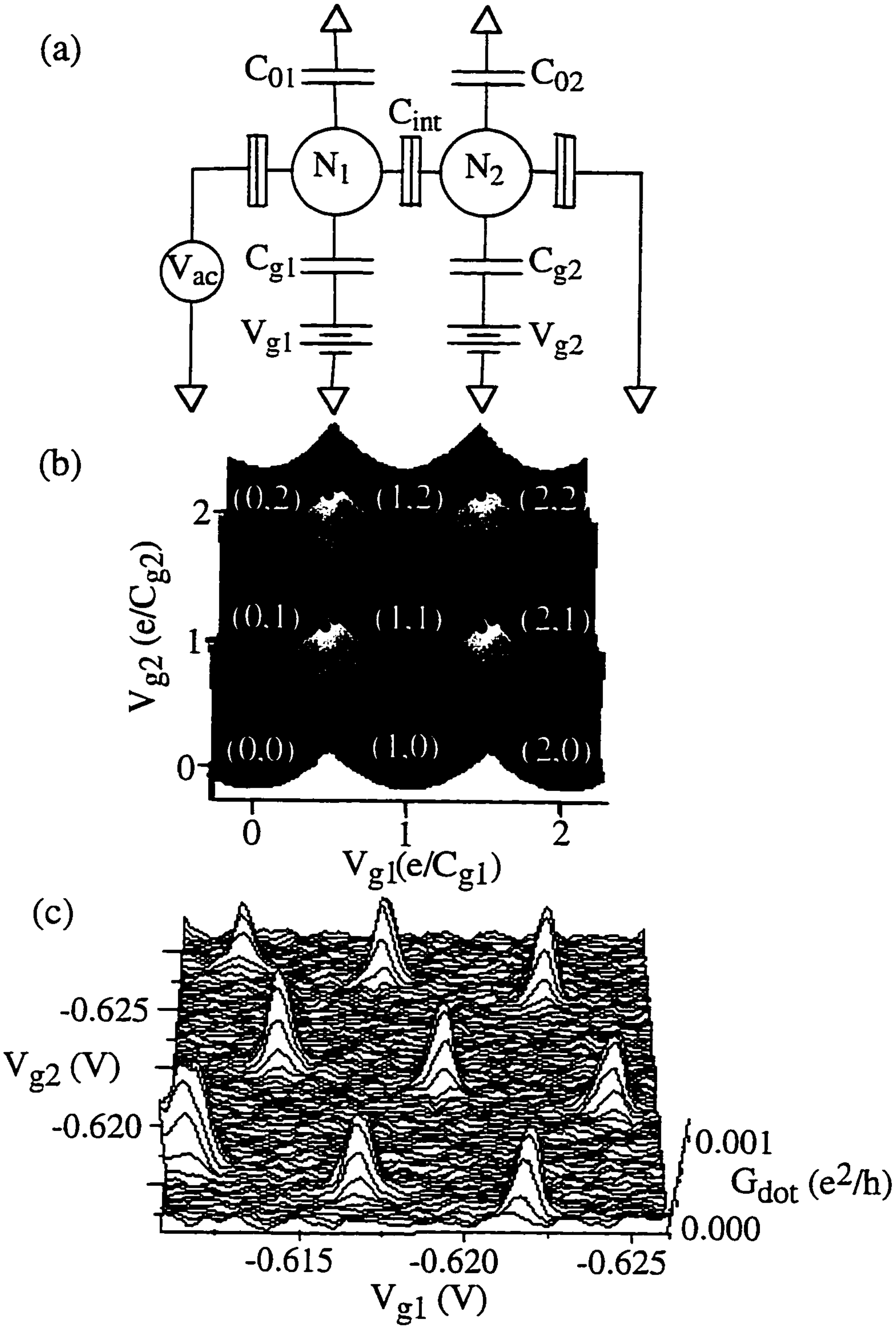

Figure 4.5 (a) Equivalent circuit for a double dot device. (b) Minimum energy surface calculated as a function of V_{g1} and V_{g2} for the above circuit. Current may flow at the intersections of three paraboloids, marked by black dots. (c) Surface plot of the measured conductance of a double dot with $G_{int} \cong 0.22\ G_0$. Current flows at an array of points as predicted.

represented by tunnel junctions (split boxes). The capacitors C_{g1} and C_{g2} couple dot 1 and dot 2 to their respective side gate voltages V_{g1} and V_{g2}, and the capacitor C_{int} represents the capacitive interaction between the dots in the weak tunneling limit. The stray capacitances from each dot to ground are labeled C_{01} and C_{02}. The stray capacitance includes the capacitance to nearby fixed voltage gates and to the leads (for zero bias measurements). We define the total capacitance of each quantum dot as $C_{\Sigma 1} = C_{\Sigma 2} = C_{\Sigma} = C_{g1}+C_{01}+C_{int}$. We extract a total capacitance $C_{\Sigma 1} \cong C_{\Sigma 2} = 342 \pm 15$ aF from differential conductance measurements. The interdot capacitance $C_{int} \cong 18 \pm 7$ aF is measured from conductance peak splittings and current-voltage characteristics [Crouch, 1996a].

The total electrostatic energy of the double dot $E_{ddot}(V_{g1}, V_{g2})$ for given numbers of electrons (N_1, N_2) on the dots is controlled by the side gate voltages V_{g1} and V_{g2}. As with the single dot, the energy of the system is equal to the total energy stored in the capacitors minus the work done by the batteries to achieve this charge configuration. E_{ddot} is given by

$$\begin{aligned} E_{ddot} = &\sum_{i}^{i\in dot1}\left[\frac{1}{2}C_i(V_i-\phi_1)^2 - C_iV_i(V_i-\phi_1)\right]+ \\ &\sum_{i}^{i\in dot2}\left[\frac{1}{2}C_i(V_i-\phi_2)^2 - C_iV_i(V_i-\phi_2)\right]+\frac{1}{2}C_{int}(\phi_1-\phi_2)^2 \end{aligned} \tag{4.1}$$

where the potentials ϕ_1 and ϕ_2 of the two dots are given by

$$\phi_{1,2} = \sum_{i}^{i\in dot1,2}\left(C_iV_i - N_{1,2}e\right)/C_{\Sigma} \tag{4.2}$$

Referring to our equivalent circuit, we find that

$$\phi_{1,2} = \frac{C_{int}\left(C_{g2,1}V_{g2,1} - N_{2,1}e\right) + C_{\Sigma}\left(C_{g1,2}V_{g1,2} - N_{1,2}e\right)}{C_{\Sigma}^2 - C_{int}^2} \tag{4.3}$$

Plugging in and eliminating terms independent of N_1 and N_2, we arrive at the total energy of the double dot system in the absence of electron tunneling,

$$E_{ddot} = \frac{1}{2C_\Sigma(1-\alpha^2)}\Big[(C_{g1}V_{g1} - N_1e)^2 + (C_{g2}V_{g2} - N_2e)^2 + \\ +2\alpha(C_{g1}V_{g1} - N_1e)(C_{g2}V_{g2} - N_2e)\Big] \tag{4.4}$$

where $\alpha \equiv C_{\rm int} / C_\Sigma$.

Figure 4.5b is a plot of the minimum energy surface $E_{ddot}(V_{g1}, V_{g2})$ calculated from equation 4.4 using experimentally measured parameter values. For a given charge configuration (N_1, N_2), the energy surface $E_{ddot}(V_{g1}, V_{g2})$ is a paraboloid. The complete minimum energy surface is a two-dimensional array of paraboloids, the double dot equivalent of single dot energy parabolas. Each paraboloid corresponds to a different charge configuration that minimizes the total electrostatic energy over some range of V_{g1} and V_{g2}. The lowest energy charge configurations (N_1, N_2) are labeled in Figure 4.5b.

The energy $E_{ddot}(V_{g1}, V_{g2})$ determines the values of V_{g1} and V_{g2} at which current can flow through the double dot. Conduction through two dots in series occurs only when both N_1 and N_2 can change simultaneously, at the intersections of three paraboloids marked by black dots in Fig. 4.5b. Consider a double dot in the (0,0) state. Current flows if an electron tunnels onto the first dot (1,0), passes from there to the second dot (0,1), and finally exits into the other lead (0,0). Because these three states have equal energy at the marked intersections, the Coulomb blockade is simultaneously lifted for both dots.

Figure 4.5c is a surface plot of the measured conductance G_{ddot} through a double quantum dot vs. V_{g1} and V_{g2} for low interdot tunnel conductance ($G_{int} \cong 0.22\ G_0$, where $G_0 \equiv 2e^2/h$). The measurement is made at dilution refrigerator base temperature (25 mK), which corresponds to an electron temperature of about 75 mK. Current flows at the array of points predicted by simple Coulomb blockade theory. Each peak is composed of two peaks slightly split by C_{int}, though they are difficult to resolve. These points occur at the intersections of the hexagonal regions defined by a particular charge configuration (N_1, N_2). The pattern is compressed along the diagonal because of cross-capacitance between each side gate and the opposite dot. This low-tunneling limit has been observed in prior work on islands or double dots in series [Pothier *et al.*, 1991; Dixon *et al.*, 1996] and on parallel dots [Hofmann *et al.*, 1995].

We can also apply simple Coulomb blockade theory when the two dots are completely merged into one large, composite dot by very strong interdot tunneling. In that case the total double dot charge $N_1 + N_2$ is quantized, but N_1 and N_2 individually are not. The situation simplifies to the single dot discussed in chapter 2, and current flows whenever the Coulomb blockade is lifted for the single composite dot (that is, when the total induced charge $C_{g1}V_{g1} + C_{g2}V_{g2}$ equals a half integer number of electrons.) Figure 4.6a shows schematically the lines in the V_{g1}-V_{g2} plane along which this condition is met.

Figure 4.6b is a surface plot of double dot conductance G_{ddot} vs. side gate voltages V_{g1} and V_{g2}, measured when the dots are completely joined by $G_{int} \cong 0.98\ G_0$. Current flow is restricted to an array of lines in the diagonal direction. These lines separate regions defined by integer values of the total number of electrons $N_{tot} = N_1 + N_2$ on the double dot. N_{tot} increases with the average gate voltage $V_{av} = (V_{g1} + V_{g2})/2$; the conductance pattern is insensitive to polarization induced by differences in gate voltage $\Delta V = V_{g1} - V_{g2}$ because the two dots have joined into one.

Effects of interdot tunneling

We must move beyond simple Coulomb blockade analysis to describe the case of arbitrary interdot tunnel conductance. The Coulomb blockade remains valid for the double dot as a whole but ceases to apply to the individual dots. Electron tunneling weakens the quantization of charge on each separate dot and lowers the ground state energy of the

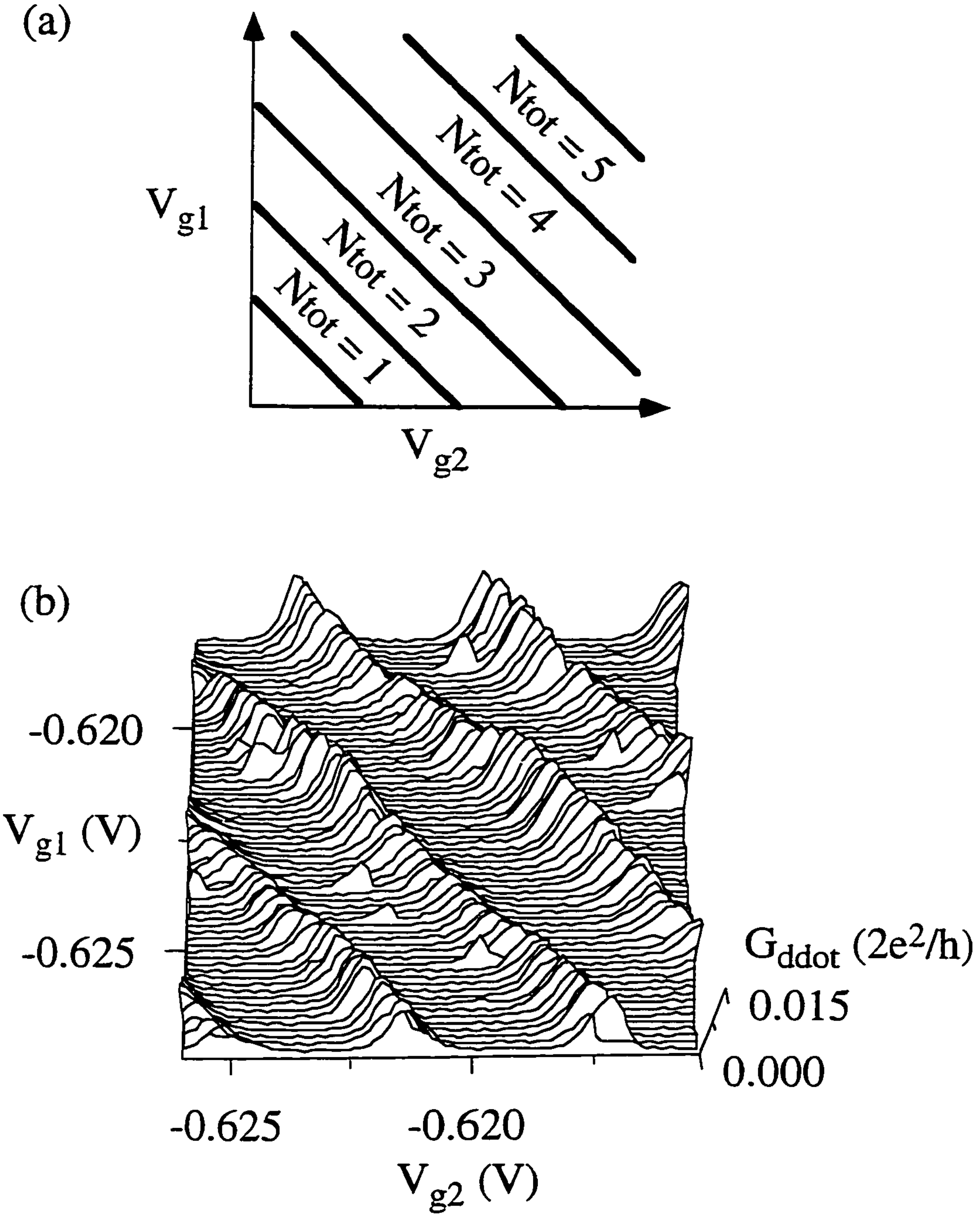

Figure 4.6 (a) Diagram indicating where the energy surfaces corresponding to different total double dot charges intersect for very strong interdot tunneling. (b) Plot of measured conductance of a double dot with strong interdot tunneling $G_{int} \cong 0.98\ 2e^2/h$. Conductance occurs along the lines predicted in (a).

system. This, rather than capacitive coupling, becomes the dominant interdot interaction. Several theories have been developed to describe the effect of electron tunneling on the ground state energy [Matveev *et al.*, 1996a; Golden *et al.*, 1996a; Golden *et al.*, 1996b; Matveev *et al.*, 1996b; Ruzin *et al.*, 1992; Klimeck *et al.*, 1994; Stafford *et al.*, 1994]. This thesis will refer mostly to the work done both by Golden and Halperin [1996a; 1996b] and by Matveev, Glazman, and Baranger [1996a; 1996b] because their starting assumptions and results closely match the experimental situation. We will first present a physical picture of how electron tunneling affects double dot energetics and then discuss the theory in more quantitative detail.

The configuration of quantized electron charges in coupled dot systems plays an essential role in coupled dot energetics. For balanced gate voltages $V_{g1} = V_{g2}$, the induced charges $C_{g1}V_{g1}$ and $C_{g2}V_{g2}$ on each dot are equal, and the lowest energy configurations have equal numbers of electrons on each dot so that $N_{tot} = N_1 + N_2$ is even. If one additional electron is added, making the total number of electrons odd, charge quantization requires that this electron reside on one dot or the other in the limit of weak interdot tunneling, so that the double dot is polarized with an electric dipole moment. This polarization costs additional electrostatic energy. If the gate voltages are adjusted with $V_{g1} \neq V_{g2}$ to induce a polarized charge configuration with $N_1 \neq N_2$, one finds analogous situations in which charge quantization results in unpolarized configurations $N_1 = N_2$ with excess energy. In general, quantization of charge on individual dots of coupled dot systems results in frustrated configurations in which the actual charge differs from that induced by the gate voltages, producing excess electrostatic energy.

Tunneling between dots relaxes the requirement for charge quantization on each dot and changes both the coupled dot ground-state energy and the selection rules for charge transport. The condition for quantization of charge in many body systems is of fundamental interest and has been studied theoretically [Glazman *et al.*, 1990; Matveev, 1991; Matveev, 1995; Falci *et al.*, 1995]. Matveev [1995] has studied a single quantum dot connected to its environment by a quantum point contact with tunnel conductance G_p near one mode. He finds that as G_p approaches $G_p = 2e^2/h$, the periodic oscillations of the charging energy with dot charge decrease continuously, and that charge quantization is completely destroyed when $G_p = 2e^2/h$. In tunnel-coupled double dots, tunneling reduces the excess electrostatic energy associated with charge quantization, as for the frustrated configurations described above, by allowing electrons to be shared between dots. Many body theory of tunnel coupled double dots [Golden *et al.*, 1996a; Golden *et al.*, 1996b; Matveev *et al.*, 1996a; Matveev *et al.*, 1996b] predicts that the excess energy of such frustrated charge configurations is controlled by the interdot tunnel conductance G_{int}, and decreases continuously from a maximum at $G_{int} = 0$ to zero at $G_{int} = 2e^2/h$. For dot geometries such as in figure 4.1a, this transition is driven entirely by the change in interdot conductance because the classical interdot capacitance remains approximately constant [Waugh *et al.*, 1996]. Interdot tunneling also relaxes the selection rules for charge transport through a series double dot because added electrons are shared by both dots.

Previous experiments have seen evidence of the transition from separate to joined dots [Waugh *et al.*, 1995; Van der Vaart *et al.*, 1995a; Van der Vaart, 1995b; Blick *et al.*, 1996]. For example, Waugh *et al.* [1995] measured the conductance as a function of V_{av} ($V_{g1} = V_{g2}$) and found that the closely spaced pairs of conductance peaks predicted in figure 4.5b split apart in the V_{av} direction as the interdot tunnel conductance increased. This effect is quantified in the fractional peak splitting F, defined as twice the ratio of the peak splitting ΔV_s to the periodicity of pairs of peaks ΔV_p: $F \equiv 2\Delta V_s/\Delta V_p$. The fractional peak splitting is directly proportional to the lowering of the energy by interdot tunneling. The energy lowering, or interaction energy, is given by

$$E_{int} = F\frac{e^2}{4C_\Sigma} \tag{4.5}$$

Figure 4.7 plots the energy of different charge states (N_1, N_2) as a function of V_{av} to demonstrate the connection between energy lowering and peak splitting. This plot corresponds to a diagonal slice in the V_{av} direction through the minimum energy surface shown in figure 4.5b. The (0, 0) and (1, 1) energy parabolas each have the lowest energy over some range of side gate voltage. The (1, 0) and (0, 1) states are higher in energy because the polarized charge configuration costs energy. In the absence of interdot interaction, current flows at the point where the four states intersect. A tunneling interaction reduces the energy of the polarized charge configuration, lowering the $N_{tot} = 1$ energy curves as shown by the dotted energy parabola. The single intersection is replaced by two intersections at which current can flow; the peak splits.

Two groups have made similar calculations of how tunneling interactions modify double dot energetics and manifest themselves in observable quantities like the peak splitting [Golden *et al.*, 1996a; Golden *et al.*, 1996b; Matveev *et al.*, 1996a; Matveev *et al.*, 1996b]. We will summarize their approach, modeling our discussion after the work of Golden and Halperin on symmetric quantum dots in series.

For weakly coupled dots, the Hamiltonian describing two dots connected by tunneling matrix elements is given below.

$$H = \sum_{i=1}^{2}\sum_{k,\sigma}\varepsilon_{ik\sigma}\hat{n}_{ik\sigma} + \sum_{k_1,k_2,\sigma}t_{k_1k_2}\left(c^{\dagger}_{2k_2\sigma}c_{1k_1\sigma} + H.c.\right) + \frac{U_\Phi}{2}\left(\hat{N}_{tot} - \Phi_{tot}\right)^2 + U_\rho\left(\hat{n} - \rho/2\right)^2 \quad (4.6)$$

The subscript i is the dot index, k refers to the electron state (excepting spin), and σ is the channel index (which is the spin index for our case of one spin-degenerate mode in the center point contact.) The first term is the kinetic energy of the occupied electron states. The second term describes the tunneling that connects states on one dot with states on the other. The final two terms are the electrostatic energy from equation 4.4, rewritten in terms of the total charge $N_{tot} \equiv N_1 + N_2$ of the double dot and the charge difference $n \equiv (N_1 - N_2)/2$ between the dots. The potentials Φ_{tot} and ρ are given by

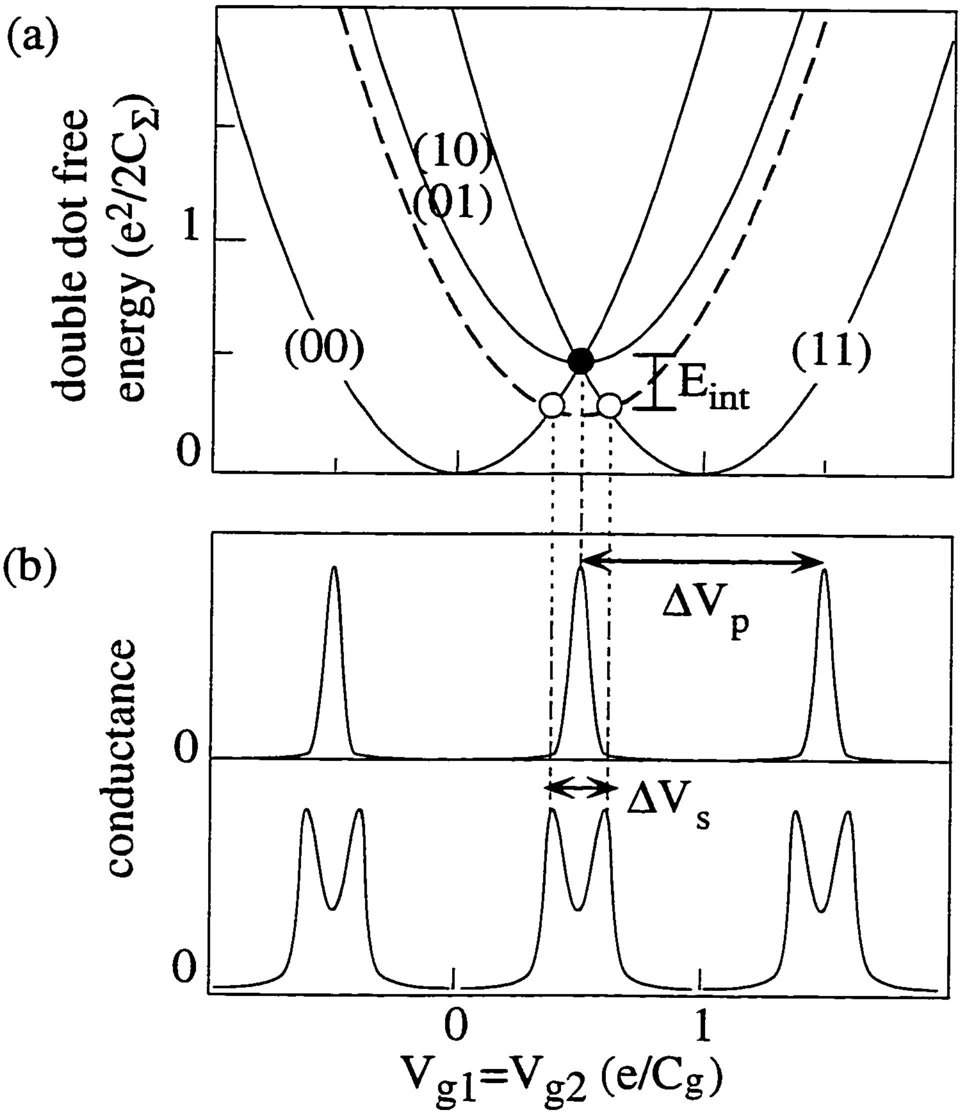

Figure 4.7 (a) Energy plotted vs. side gate voltage for a double dot with the two side gates at the same potential. The (0, 0) and (1, 1) states both have lowest energy over some range of side gate voltage; the (1, 0) and (0, 1) states have greater electrostatic energy because of the electric dipole moment. An interaction replaces the (1, 0) and (0, 1) states by $N_{tot} = 1$ states (dotted curve) and lowers their energy by an amount E_{int}. (b) Schematic plot of double dot conductance vs. side gate voltage indicating how Eint causes peak splitting. For $E_{int} = 0$ parabolas intersect at a point. For $E_{int} > 0$, parabolas intersect at two points. After Waugh [1994].

$$\Phi_{tot} = \phi_1 + \phi_2 \tag{4.7}$$

$$\rho = \phi_2 - \phi_1 \tag{4.8}$$

With the outer point contacts well closed, the total number of electrons N_{tot} is a good quantum number. The physics of charge fluctuations between dots may be understood by considering that case in which there are no fluctuations of the total double dot charge. With N_{tot} fixed, the total double dot charge term may be omitted from the Hamiltonian. The final Hamiltonian for weakly coupled dots is

$$H = \sum_{i=1}^{2} \sum_{k,\sigma} \varepsilon_{ik\sigma} \hat{n}_{ik\sigma} + \sum_{k_1,k_2,\sigma} t_{k_1 k_2} \left(c^{\dagger}_{2k_2\sigma} c_{1k_1\sigma} + H.c. \right) + U_\rho \left(\hat{n} - \rho/2 \right)^2 \tag{4.9}$$

where $\hat{n}$ is now an operator.

In the model for weakly coupled dots, the tunneling matrix element is a constant t_{k1k2} = t for states in a large energy range, which is on the order of the Fermi energy if the barrier is narrow. The coupling of states over a broad energy range reflects the fact that the temperature does not determine the coupling bandwidth. Rather, it is the coupling of levels over an energy range on the order of the charging energy that brings about the breakdown of the Coulomb blockade on the individual dots. One central result is an expression for the fractional peak splitting as a function of the number of channels N_{ch} ($N_{ch} = 2$ in our case) and the interdot tunnel conductance $g \equiv G_{int}/(2e^2/h)$ in the limit of low g:

$$F \equiv 0.1404 N_{ch} g + 0.1491 N_{ch} g^2 - 0.009798 (N_{ch})^2 g^2 + \ldots \tag{4.10}$$

The theory treats the strong tunneling limit by introducing a small amount of backscattering to an otherwise perfectly conducting channel connecting the dots. The physics is dominated by the one-dimensional channel, which is described by the Hamiltonian

$$H = \sum_{j=1}^{2} \sum_{k,\sigma} \xi_{k\sigma} \hat{n}_{jk\sigma} + U_\rho \left(\hat{n} - \rho/2\right)^2 + H_B \sum_{k_1,k_2,\sigma} v_{k_1 k_2} \left(c^{\dagger}_{2k_2\sigma} c_{1k_1\sigma} + H.c.\right) \tag{4.11}$$

The first term is the kinetic energy of a particle in the channel with channel index (i.e. spin index) σ, state index k, and a direction of motion index j, where j = 1 means "moving to the right" and j = 2 means "moving to the left". The second term is the familiar reduced electrostatic potential energy, and the third term describes backscattering from one direction of motion to the other. Proceeding in the bosonization formalism [see Golden, 1997 and references therein], one obtains the fractional peak splitting for one spin degenerate mode in the strong tunneling limit,

$$F \cong 1 + \frac{16 e^{\gamma}}{\pi^3} (1-g) \ln(1-g) - 0.425(1-g) \tag{4.12}$$

where $\gamma \cong 0.577$ is the Euler-Mascheroni constant.

4.3 Double dot conductance measurements

This section presents measurements of the conductance through a double dot as a function of the induced charges $C_{g1}V_{g1}$ and $C_{g2}V_{g2}$ and the interdot tunnel conductance G_{int}. The device was cooled to base temperature (T ≅ 25 mK) in a dilution refrigerator, and the gates were energized with the outer point contacts in the tunneling regime. By inducing charge separately on the two dots, we were able to measure the charging diagram and probe the ground state energy. We measured the charging diagram for interdot tunnel conductance ranging from $G_{int} \cong 0.22\ G_0$ to $G_{int} \cong 0.98\ G_0$.

Figures 4.8a-f plot logarithmic grayscale images of the double dot conductance G_{ddot} as a function of V_{g1} and V_{g2}. Dark spots represent high conductance, and bright regions represent low conductance. The images are arranged in order of increasing interdot conductance, with figure 4.8a and figure 4.8f corresponding to figures 4.5c and 4.6b respectively. We note again the close agreement of measured conductance with simple Coulomb blockade theory for the near zero tunneling and completely merged regimes. For intermediate interdot tunneling, the conductance pattern changes markedly and is no longer described by the Coulomb blockade theory of individual dots.

We observe two primary trends in the evolution of the conductance images from figure 4.8a to figure 4.8f. First, the initial points of conductance in panel (a) split in two and progressively separate as interdot tunnel conductance increases. Second, conductance appears and steadily grows out along the boundaries that separate neighboring charge states. The splitting between and locations of these lines of conductance provide information both about the ground state charge configuration and about the degree to which electron tunneling has lowered the ground state energy. The heights and shapes of the peaks reflect excitations in the system.

A starting point for comparing these measurements with theory is to ask at what interdot tunnel conductance the transition from entirely separate dots to entirely joined dots is complete. We find that the evolution from an array of points to an array of lines is complete when the interdot tunnel conductance $G_{int} = 0.98e^2/h$. This is in quantitative agreement with the theoretical work of Golden *et al.* [1996a; 1996b] and Matveev *et al.* [1996a; 1996b]; once one spin degenerate mode (two channels) is perfectly transmitting in the constriction, frustrated charge configurations are completely relaxed.

The evolution of the conductance pattern is a signature of the quantum mechanical tunneling processes that dominate interdot interactions in the intermediate and strong tunneling regimes. As figure 4.5b demonstrates, if coupling between dots were purely capacitive, current flow would be restricted to the intersection points of the hexagonal cells

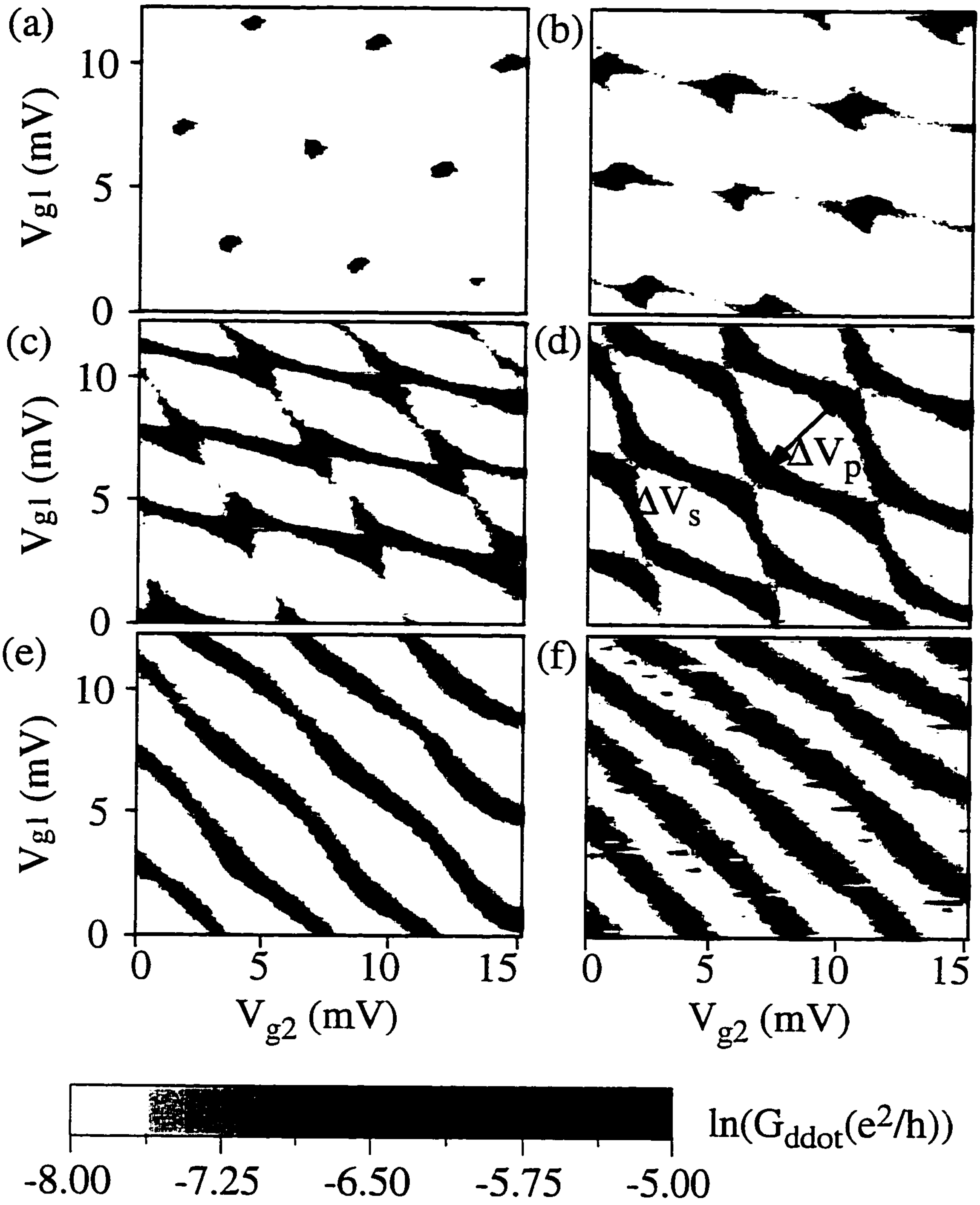

Figure 4.8 Natural log of the measured double dot conductance plotted in grayscale vs. change in gate voltages V_{g1} and V_{g2}. Dark indicates high conductance, and bright indicates low conductance. Panels are arranged in order of increasing interdot tunnel conductance Gint, with (a) $G_{int} = 0.22\ G_0$, (b) $G_{int} = 0.40\ G_0$, (c) $G_{int} = 0.65 G_0$, (d) $G_{int} = 0.78 G_0$, (e) $G_{int} = 0.96 G_0$, and (f) $G_{int} = 0.98\ G_0$. Panel (f) is thresholded to a higher value of conductance than the other panels.

of the charging diagram.[1] The growth of conductance outward along the boundaries between cells is firm evidence for loss of charge quantization because of tunneling processes. Those lines mark the boundaries between neighboring charge configurations such as (N_1, N_2) and $(N_1 + 1, N_2)$. Along these lines, the Coulomb blockade is lifted for one quantum dot but not for the other. The observed current flow is the result of a quantum mechanical process by which an electron that nominally tunnels onto the non-blockaded dot can "leak" to the other dot by tunneling into a virtual state. If the electron escapes into the lead instead of back to the dot in which it started, current flows. The increase of current flow along the charge state boundaries with increasing interdot tunnel conductance reflects the increasing magnitude of the tunneling interactions.

The changing peak positions outline the contours of the lowest energy charge states. In the near zero tunneling limit, the points of conductance occur at the intersections of hexagonal cells corresponding to different values of (N_1, N_2); we can map out the lowest energy charge configurations by connecting the intersection points. For higher interdot tunnel conductance, the hexagonal cells of given (N_1, N_2) are replaced by wavy diagonal stripes that divide different values of $N_{tot} = N_1 + N_2$. The charge states (N_1, N_2) and $(N_1 + 1, N_2 - 1)$ lose their distinctiveness as charge quantization on each dot is weakened. The change in boundary locations reflects the deformation of the minimum energy surface as interdot tunnel conductance weakens charge quantization.

The fractional peak splitting between the lines of conductance in figure 4.8 measures the modification of double dot energetics by interdot tunneling and thus determines an analog of a molecular binding energy for the artificial molecule system. The minimum splitting ΔV_s in gate voltage occurs along the V_{av} direction, as shown in figure 4.8. As interdot tunnel conductance increases from $G_{int} \cong 0$ to $G_{int} \cong 2e^2/h$, this splitting increases from $\Delta V_s \cong 0$ to $\Delta V_s \cong \Delta V_p/2$ where ΔV_p is the period of the array along the V_{av} direction.

---

[1] Although any interaction can cause peak splitting in the V_{av} direction, the interdot capacitance would have to be unreasonably large to account for the increase in splitting.

Figure 4.9 plots the measured fractional splitting defined previously as $F = 2\Delta V_s/\Delta V_p$ vs. the interdot conductance G_{int}, measured separately. The error bars represent not just scatter but also systematic errors from the calibration of G_{qpc2} vs. V_{qpc2} in the presence of the other gates. Also plotted are the fractional splitting calculated by Golden and Halperin [1996b] in the weak and strong tunneling limits (solid lines) with an interpolation (dashed line); Matveev et al. [1996a] find similar theoretical results. As shown, the data and theory are in excellent quantitative agreement. The fractional peak splitting goes to one (transition complete) at $G_{int} \cong 2e^2/h$; for $G_{int} \cong 0$, the finite residual splitting from interdot capacitance is in agreement with the measured value of C_{int}. In addition, the curvature of the F vs. G_{int} characteristic is accurate.

We have also examined the temperature dependence of conductance through the double dot. The temperature measurements presented here were also made on sample KC7EE, but on a separate cooldown. Figure 4.10 is a series of plots of the measured conductance G_{ddot} as a function of side gate voltages V_{g1} and V_{g2}. Conductance is again shown in inverted grayscale, with bright indicating low conductance and dark indicating high conductance; temperature increases from panel (a) to panel (d). All four plots correspond to an interdot conductance $G_{int} \cong 0.56\ G_0$. For the series of temperature data, the lateral shift of the point contact characteristic G_{qpc2} vs. V_{qpc2} was used as a fitting parameter to calibrate the interdot conductance G_{int}. At the lowest temperatures, there is substantial variation among the peak heights in a single measured charging diagram. This reflects the fact that the discrete levels still affect transport. As the temperature is increased, the peak heights even out as the level spacing becomes unimportant. In addition, as the temperature increases, the splitting between peaks fills in by thermal rounding.

Figures 4.11a-d and 4.12a-d are similar characterizations of charging diagram vs. temperature but for different values of the interdot tunnel conductance ($G_{int} \cong 0.84\ G_0$ and $G_{int} \cong 0.95\ G_0$ respectively). The peaks splitting again fills in by thermal rounding. Note

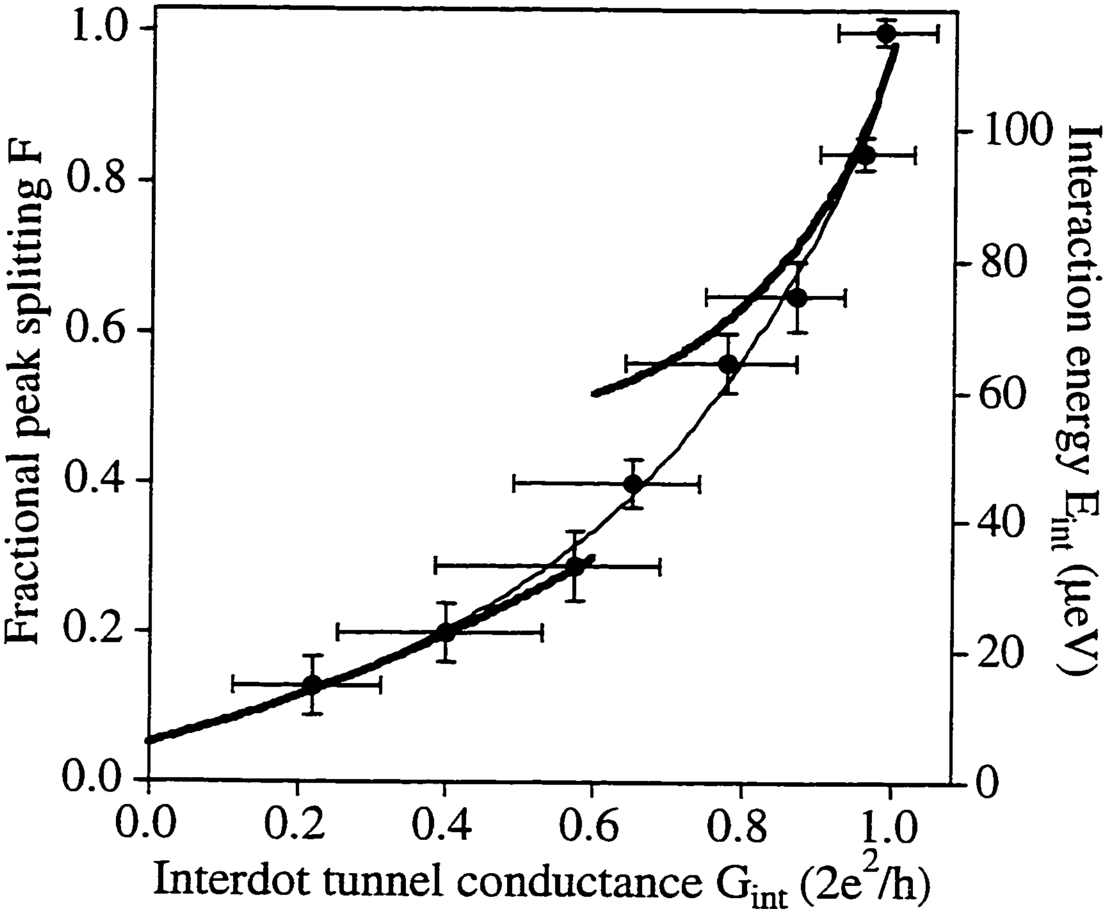

Figure 4.9 Fractional peak splitting plotted vs. interdot tunnel conductance G_{int} (measured separately). Filled circles are data points. Solid lines are theory calculated by Golden *et al.* [1996b]; similar results have been obtained by Matveev *et al.* [1996b]. The dotted line is an interpolation between the values of splitting calculated for the high and low G_{int} limits.

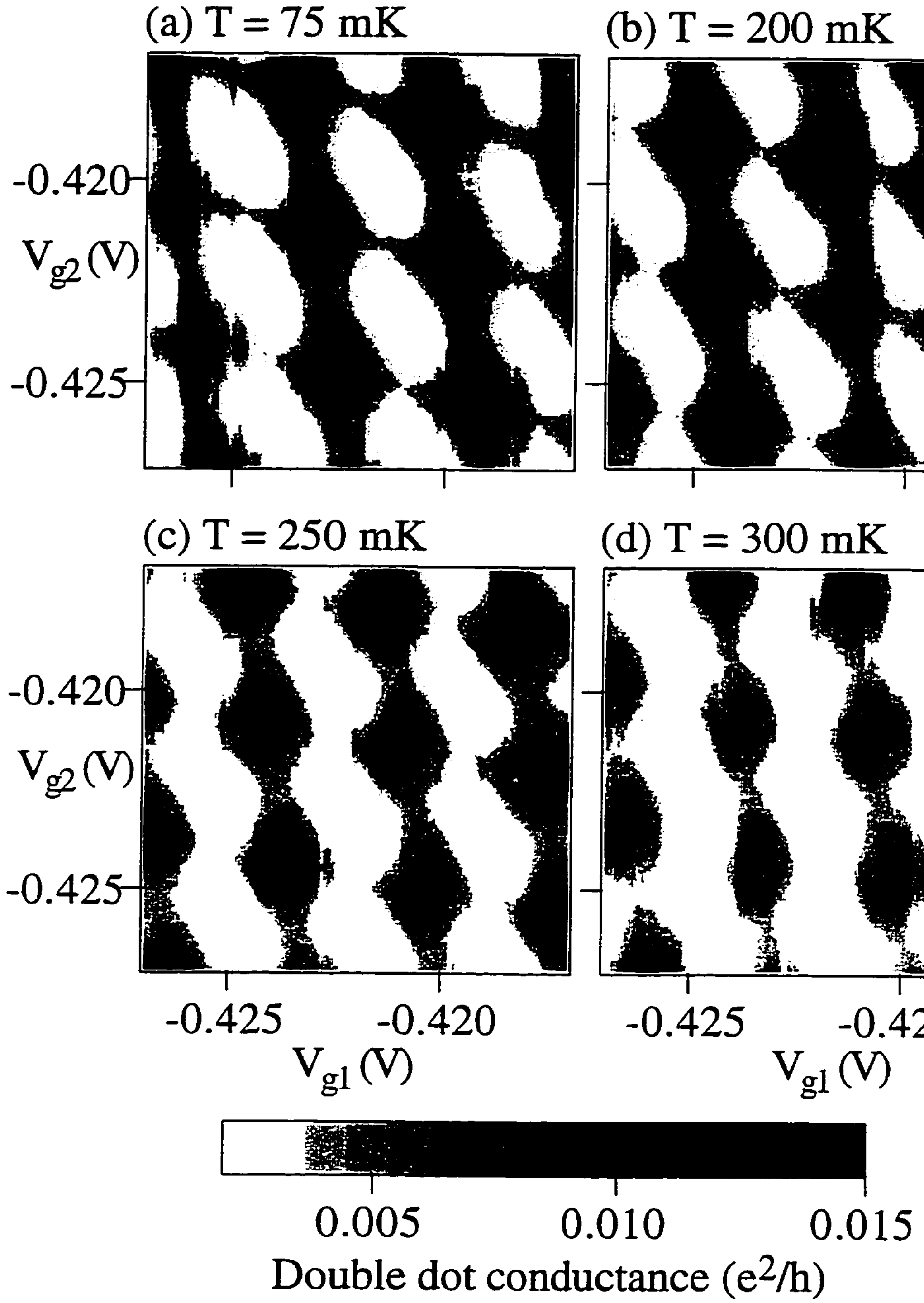

Figure 4.10 Inverted grayscale images of the measured double dot conductance G_{ddot} as a function of the side gate voltages V_{g1} and V_{g2} for an interdot conductance $G_{int} \cong 0.56\ G_0$. Each panel corresponds to a different temperature: (a) 75 mK, (b) 200 mK, (c) 250 mK, and (d) 300 mK.

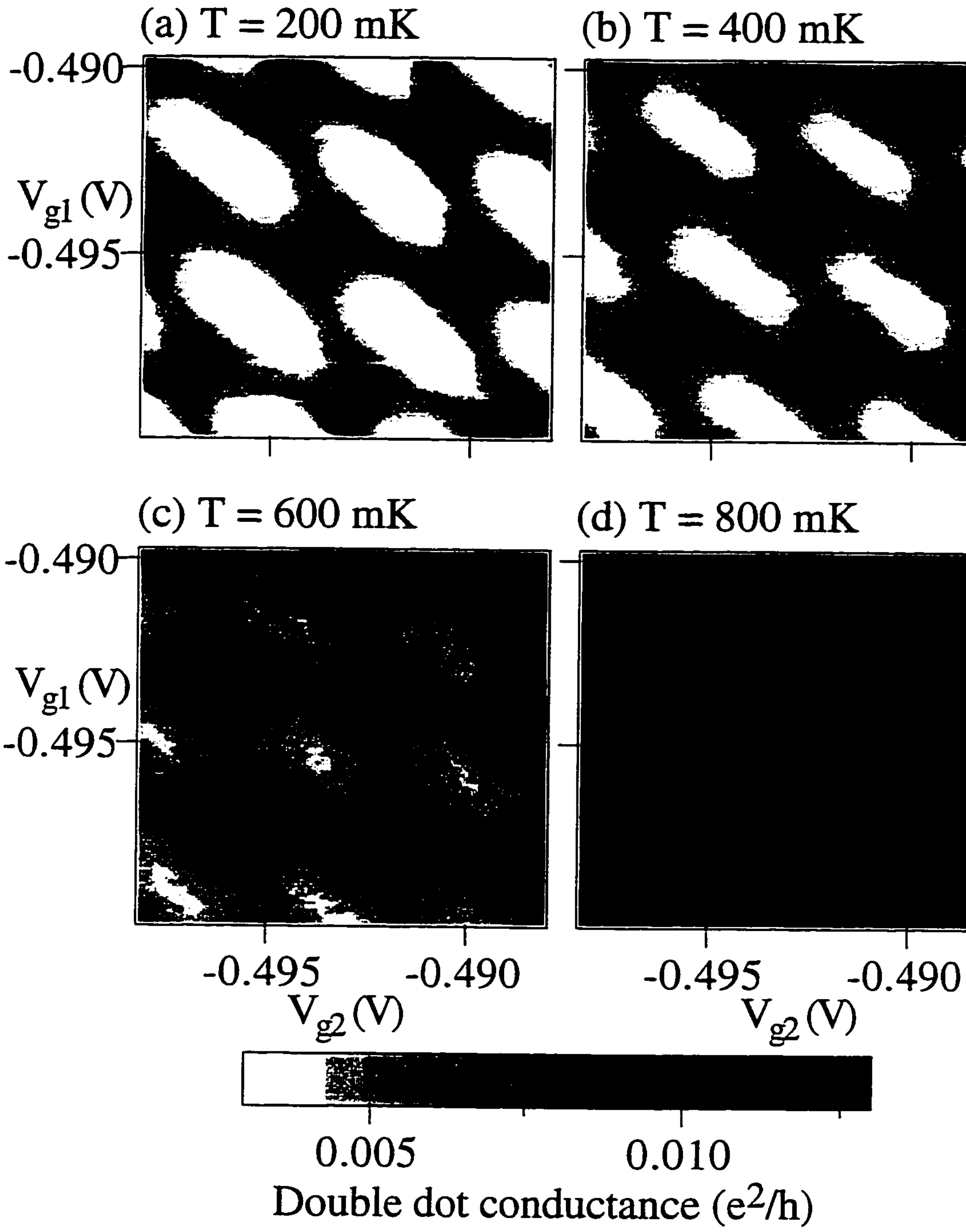

Figure 4.11 Inverted grayscale images of the measured double dot conductance G_{ddot} as a function of the side gate voltages V_{g1} and V_{g2} for an interdot conductance $G_{int} \cong 0.84\ G_0$. Each panel corresponds to a different temperature: (a) 200 mK, (b) 400 mK, (c) 600 mK, and (d) 800 mK.

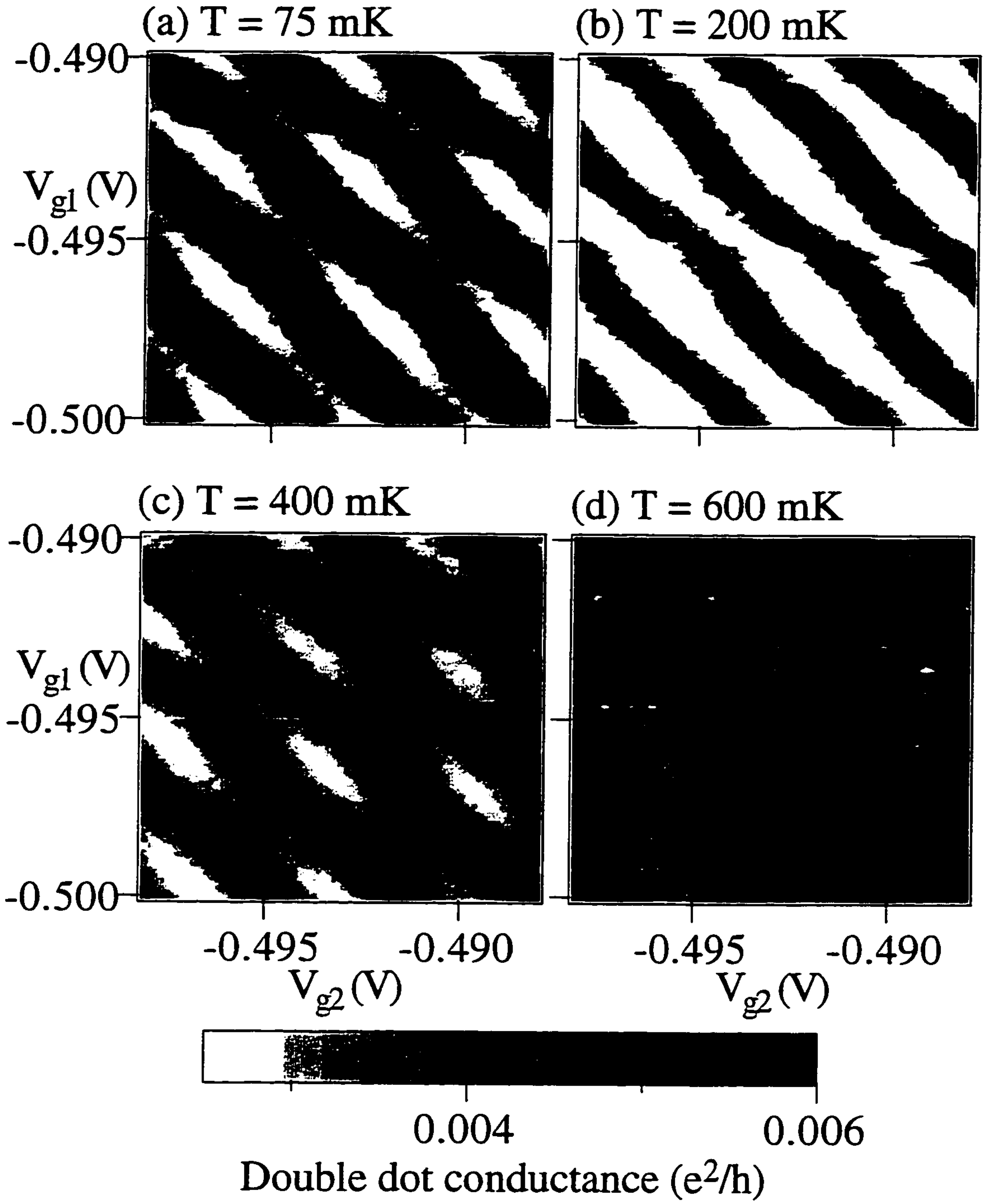

Figure 4.12 Inverted grayscale images of the measured double dot conductance G_{ddot} as a function of the side gate voltages V_{g1} and V_{g2} for an interdot conductance $G_{int} \cong 0.95\ G_0$. Each panel corresponds to a different temperature: (a) 75 mK, (b) 200 mK, (c) 400 mK, and (d) 600 mK.

that the temperature scale for this broadening increases with higher values of interdot conductance, as the peaks to be merged begin from progressively more distant positions.

Peak fits of high resolution data confirm the impression of thermal rounding and shed additional light on transport processes in the double dot system. Figure 4.13a-c plots the conductance G_{ddot} vs. V_{av} for a double dot with $G_{int} \equiv 0.78\ G_0$ at three different temperatures. The circles are the data; the lines are a fit to the sum of two thermally broadened line shapes, as described for single quantum dots in chapter 2. This figure is reproduced from the thesis of Catherine Crouch. There is excellent agreement between the observed shape and the sum of thermally broadened peaks for the three temperatures. This demonstrates that electrons tunnel onto the entire double dot rather than sequentially visiting the lifetime broadened halves.

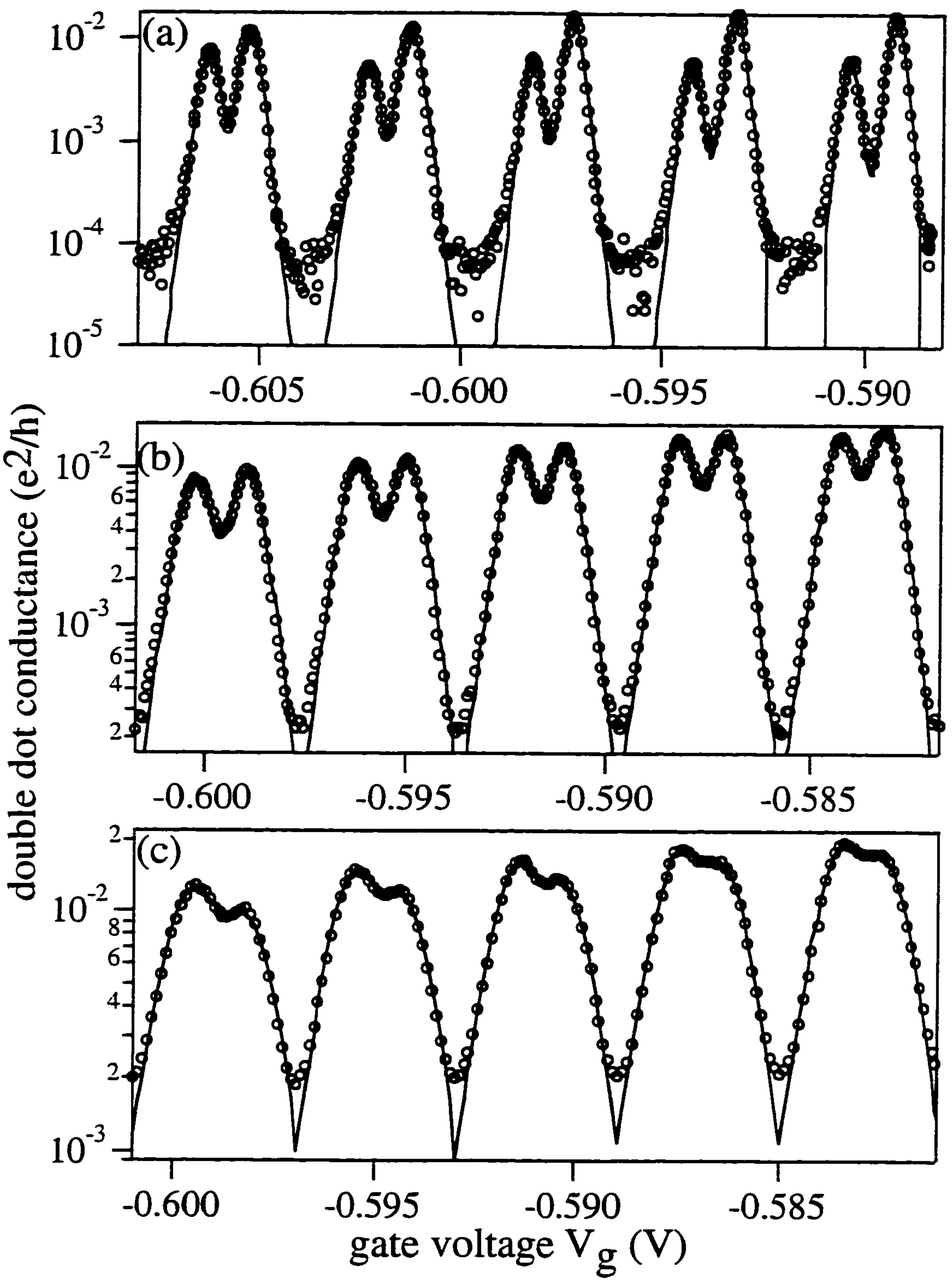

Figure 4.13 Double dot conductance (logarithmic scale) for $g_{int} = 0.78$, fit to the thermally broadened double peak shape (Eq. (5.21)) for temperatures (a) 100 mK, (b) 250 mK, and (c) 400 mK. Open symbols are data points; line is the fit. Reprinted from Crouch [1996a].

Chapter 5

Coupled Dots in the Quantum Hall Regime

This chapter describes experiments on two quantum dots of different sizes connected in series (an "asymmetric double dot") in a strong perpendicular magnetic field. The field is strong enough to place the device in the quantum Hall regime, so electrons occupy Landau levels. Electron transport in this regime differs markedly from the zero field case.

The first part of the chapter discusses measurements of double dot charge relaxation via interdot electron tunneling in a strong field. We describe experiments at a filling factor $\nu = 2$ in detail; then we compare with the central results for filling factors $\nu = 3$ and $\nu = 4$. Finally, we present measurements of how conductance through a double dot responds to small variations in magnetic field.

5.1 Double dot charge relaxation

Chapter 4 presented measurements of how frustrated charge configurations of a double quantum dot are relaxed by electron tunneling between the dots. In zero field with interdot conductance $0 \leq G_{int} \leq 2e^2/h$, this tunneling occurs via two spin channels in the point contact. When electrons of different spin fluctuate in tandem between dots, the balance of charge between the dots fluctuates. When they fluctuate oppositely, the balance of spins fluctuates.

In contrast, in a perpendicular magnetic field only one spin is involved in interdot electron transport for $0 \leq G_{int} \leq e^2/h$; this strongly affects the mechanism for relaxation of frustrated double dot charge configurations. As described in chapter 2, transport in the quantum Hall regime takes place through edge states, and only those edge states that abut the device contacts contribute to the net current [Halperin, 1982]. Similarly, transport through a quantum dot or dots will depend strongly on the edge state(s) that border the point contacts. Figure 5.1a sketches the edge state structure of a double quantum dot at a filling factor $\nu = 3$ with some limited tunneling between the outer edge states on the two dots. For greater interdot tunneling, the topology of the edge states changes, and the two outermost edge states merge into one "figure eight" loop. Figure 5.1b illustrates this situation, with some limited backscattering between the two directions of electron flow in the point contact.

Figure 5.2a is an SEM micrograph of an asymmetric double quantum dot device. The sample wiring is summarized in figure 5.2b. It consists of two quantum dots defined in series by ten independently adjustable electrostatic gates. As in chapter 4, these gates independently control the dot charges and the interdot tunneling rate. Unlike in chapter 4, the two dots have different lithographic sizes, 500 nm x 800 nm and 500 nm x 600 nm. We cool the device in the Kelvinox 100 dilution refrigerator, apply a small ac bias voltage (typically 5 μV_{rms}) across the device, and use low noise lockin techniques to monitor sample conductance under different experimental conditions.

Figure 5.3 plots the two-probe conductance of the bulk chip with no gates energized as a function of magnetic field. This measurement calibrates the filling factor of the bulk material. At low values of magnetic field, the conductance oscillates on top of a declining background. At higher field, the conductance is dominated by the quantum Hall conductance plateaus.

Figure 5.4 is a plot of center point contact conductance G_{qpc2} as a function of the voltage V_{qpc2} applied to the point contact gates. For this measurement and all others through figure 5.7, the perpendicular magnetic field was set at a fixed value of 7 T, which corresponds to a filling factor $\nu = 2$. Conductance decreases stepwise in units of e^2/h from its bulk quantized value of $2e^2/h$ as each edge state separates from its counterpart on the other side of the point contact. The steps are broader and flatter than in zero magnetic field. To calibrate center point contact conductance vs. gate voltage for the actual experimental

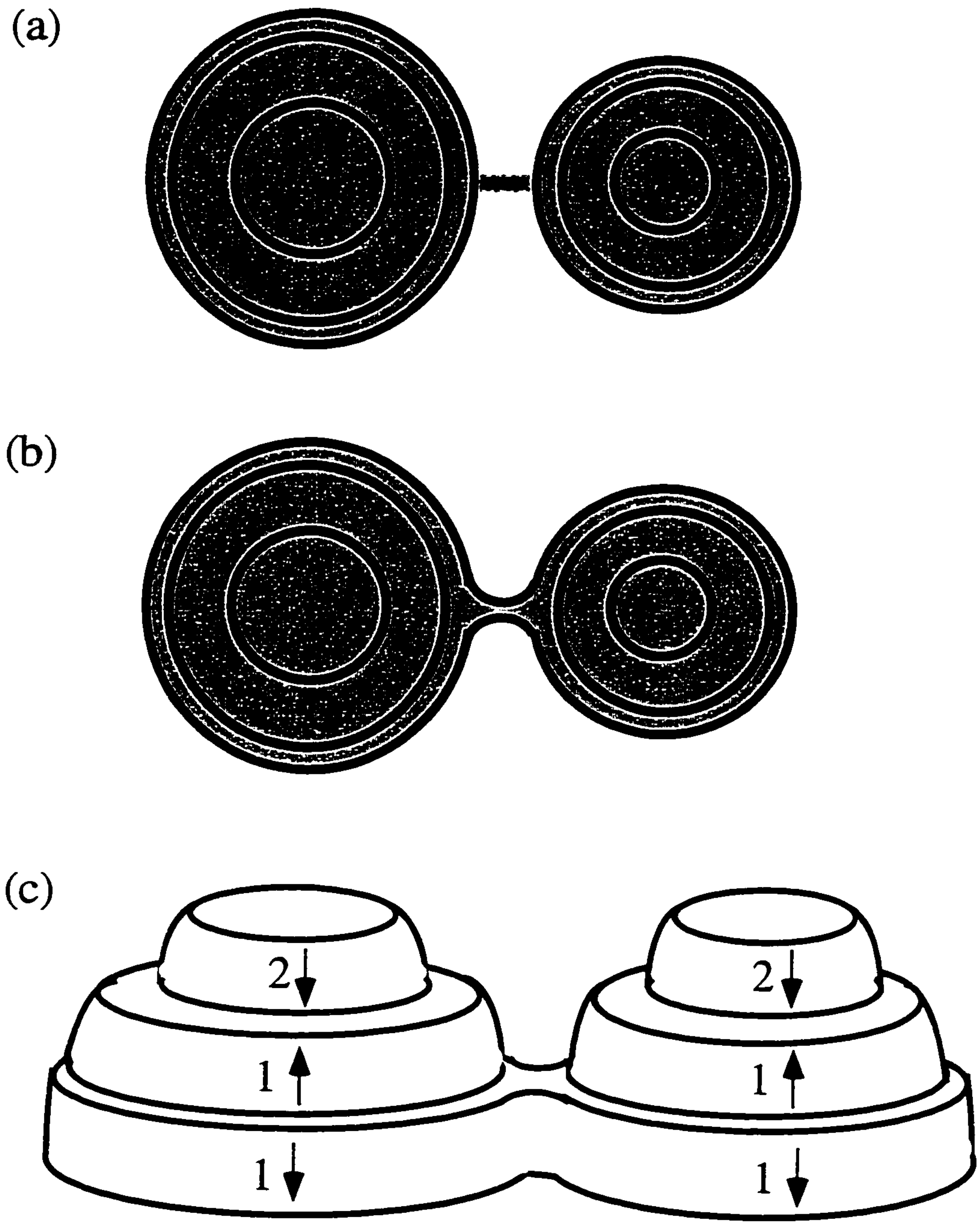

Figure 5.1 (a) Schematic top view of double dot edge state structure for filling factor $\nu = 3$ and interdot conductance $G_{int} << e^2/h$. (b) Schematic top view of similar double dot edge state structure, but with $G_{int} \equiv e^2/h$. (c) Schematic diagram of the electron density profile in the double dot illustrated in (b). The lowest levels in the two dots have joined, while the upper states remain separate.

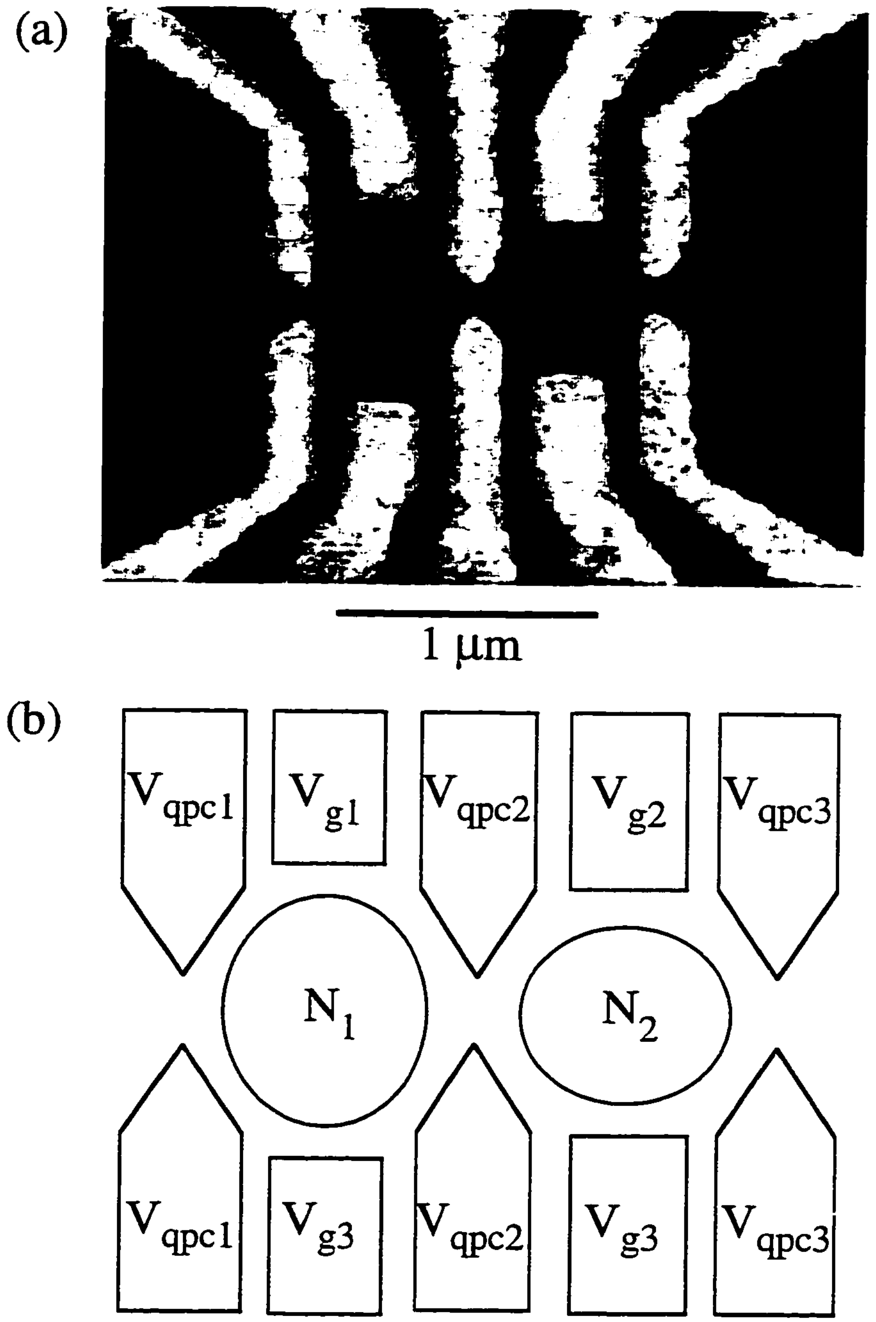

Figure 5.2 (a) Scanning electron micrograph of an asymmetric double quantum dot device. Light regions are the surface gates; dark regions are the wafer surface. (b) Wiring diagram for the device in (a).

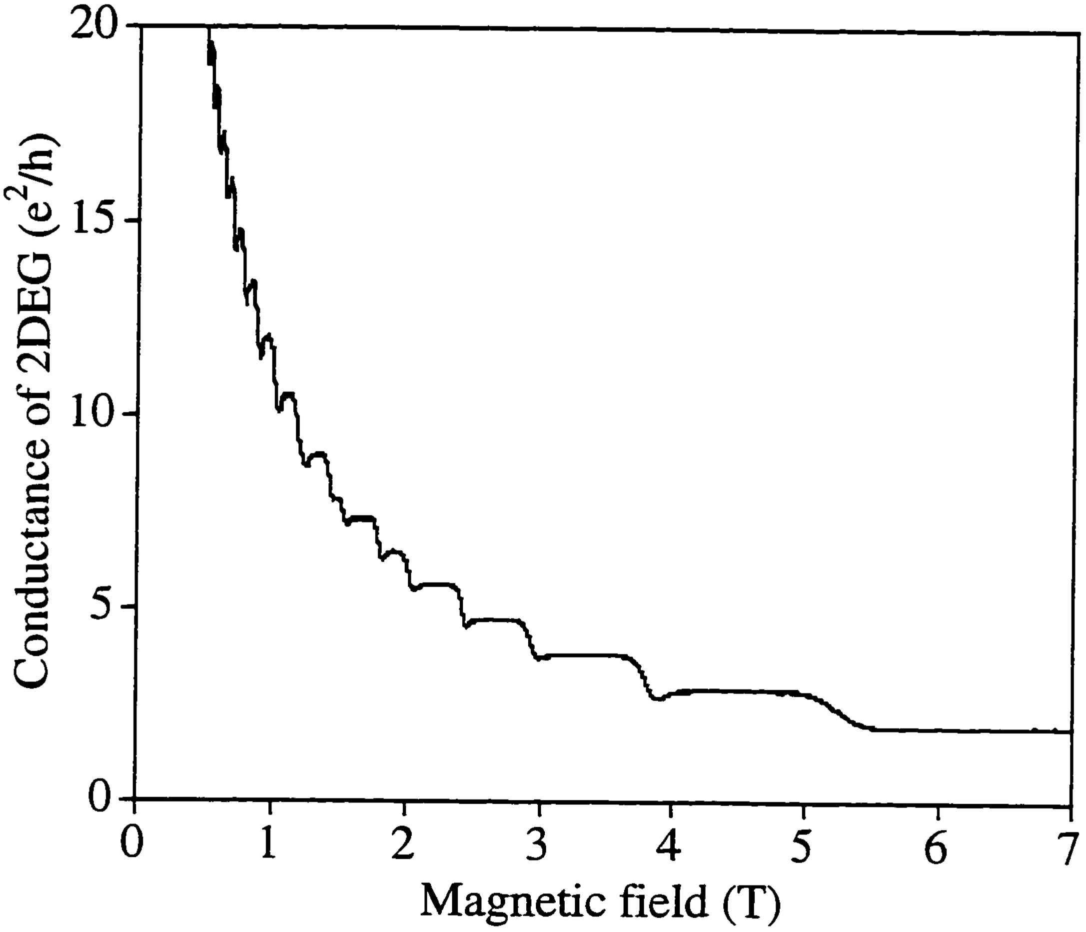

Figure 5.3 Conductance of a millimeter scale 2DEG chip measured as a function of the applied perpendicular magnetic field in a two-probe configuration. Step structure at high fields reflects the Hall plateaus; conductance dips reflect variations of the longitudinal resistivity.

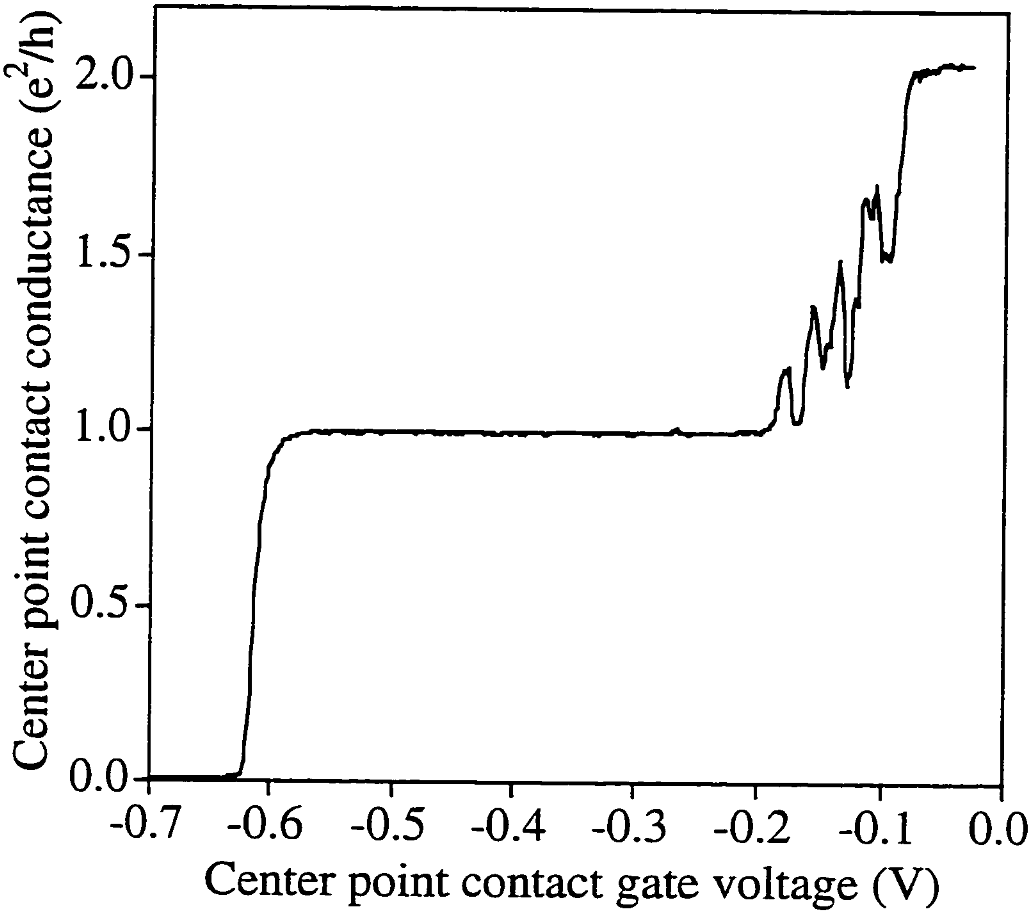

Figure 5.4 Measured conductance of the center point contact plotted vs. center point contact gate voltage V_{qpc2} in a 7 T perpendicular magnetic field ($\nu = 2$).

parameters, we must still account for cross-capacitance between gates by a rigid lateral shift. Current collimation is not a factor in the quantum Hall regime.

Figure 5.5a plots the conductance of dot 1, measured alone, as a function of its side gate voltage V_{g1}; figure 5.5b plots the conductance of dot 2 as a function of V_{g2}. These measurements yield gate capacitances $C_{g1} = 45 \pm 4$ aF and $C_{g2} = 43 \pm 4$ aF for the large and small dots respectively. The large error bars reflect the shifts in peak position visible in figures 5.5a and 5.5b. The shifts and the variable peak heights are consistent with a larger discrete energy level spacing than in the zero field case. Since electrons tunnel into the outer edge state, the discrete level spacing goes as the inverse of the dot perimeter rather than the inverse of the dot area.

As in chapter 4, we use the Coulomb blockade of transport through the entire double dot as a spectroscopic tool to learn about the interdot charge relaxation processes. We energize all ten of the surface gates such that the outer point contacts are in the tunneling regime and the center point contact has a conductance in the range of $0 \leq G_{int} \leq e^2/h$. We then measure conductance through the entire double dot as a function of the side gate voltages V_{g1} and V_{g2}, which are varied in a raster pattern. We repeat this measurement for a series of interdot tunnel conductances ranging from $G_{int} \cong 0$ to $G_{int} \cong e^2/h$.

Figures 5.6a-d summarize the results of this measurement. Each panel is an inverted grayscale image of the measured double dot conductance; dark spots indicate high conductance, and bright areas indicate low conductance. In figure 5.6a ($G_{int} \cong 0.01\ e^2/h$), current flows at an array of points; the points are split in pairs in the $V_{av} = (V_{g1} + V_{g2})/2$ direction. Apart from the large splitting, this is the familiar case of well separated dots with near zero interdot tunnel conductance. In subsequent panels the splitting between points of conductance in the V_{av} direction increases, and lines of conductance grow out from these points along the curves that separate charge configurations with different values of the total double dot charge. By figure 5.6d ($G_{int} \cong 0.96\ e^2/h$), current flows along an array of lines separating regions with different lowest energy values of $N_{tot} = N_1 + N_2$. As in the zero

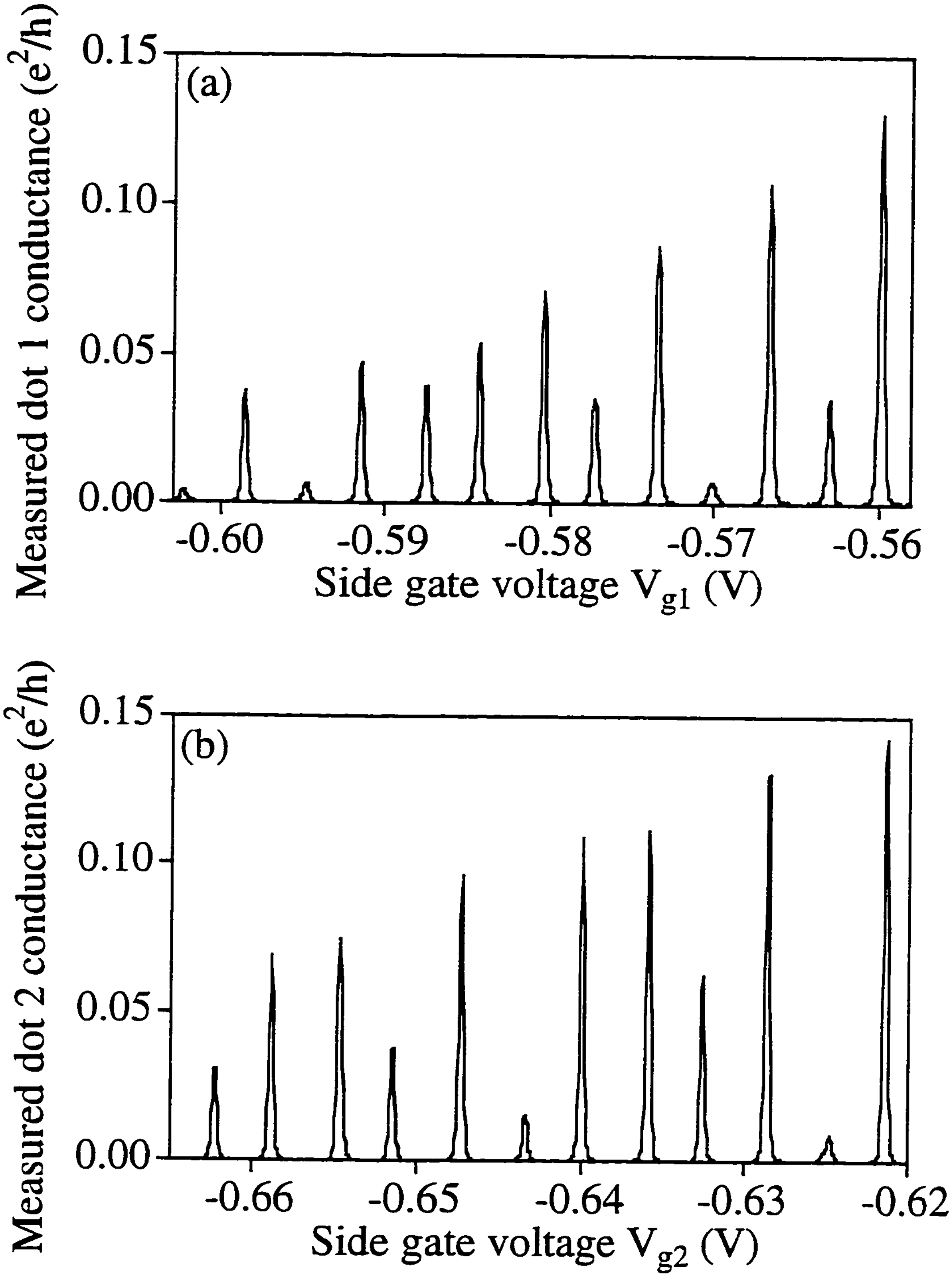

Figure 5.5 (a) Conductance of dot 1 measured as a function of side gate voltage V_{g1} at 7 T ($\nu = 2$). (b) Conductance of dot 2 similarly measured as a function of side gate voltage V_{g2}.

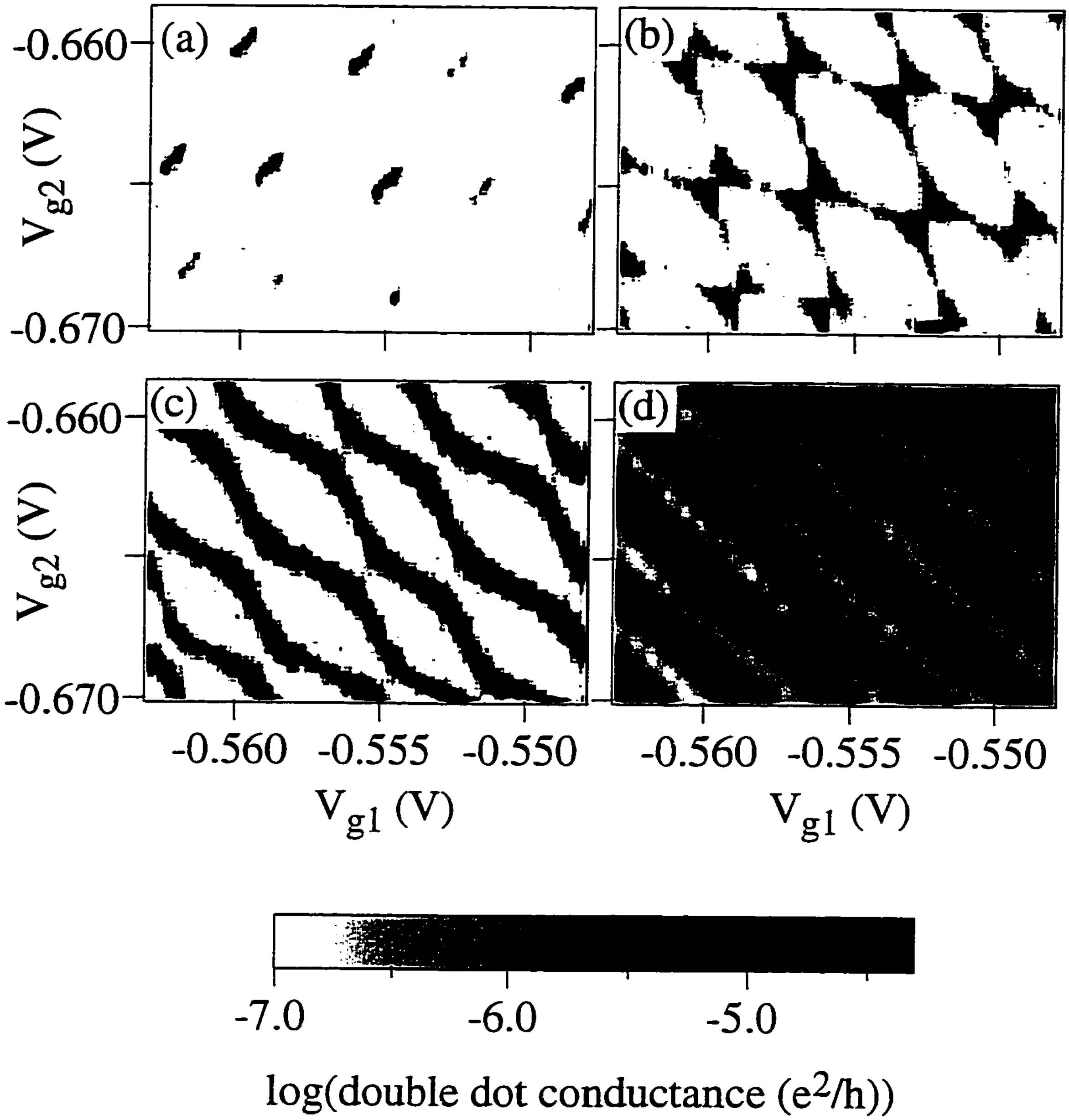

Figure 5.6 Inverted grayscale images of the natural log of the measured double dot conductance plotted vs. side gate voltages V_{g1} and V_{g2}. Data were measured in a 7 T perpendicular magnetic field ($\nu = 2$) for interdot tunnel conductances (a) $G_{int} = 0.01\ e^2/h$, (b) $0.21\ e^2/h$, (c) $0.68e^2/h$, and (d) $0.96\ e^2/h$.

field case, this topological change from an array of points to an array of lines indicates that the transition from completely separate dots to completely joined dots is complete.

There is a strong qualitative similarity between this transition in zero magnetic field, as described in chapter 4, and the transition in the strong perpendicular field case described here. It is important to note, however, that there is a large quantitative difference between these data and the observations in zero field: the transition is complete when there is one e^2/h of interdot tunnel conductance, in contrast to $2e^2/h$ for the zero field case. This indicates that frustrated configurations of double dot charge are completely relaxed when just the outer edge state in the two dots has joined up.

Several of the images in figure 5.6 do not display perfect uniformity in the splitting between neighboring points. In figure 5.6d, for example, neighboring lines occasionally approach each other more closely than in the rest of the diagram. These points of close approach are not distributed with the periodicity of the initial array, so we do not associate them with the transition from separate to joined dots. These features are a result of the magnetic field, and their origin will become evident from measurements described in the following section.

Measurements of the fractional peak splitting shed light on the large separation between conductance points in figure 5.6a. Fractional peak splitting is again defined as the ratio of the peak splitting to the periodicity of the array, $F = 2\Delta V_s/\Delta V_p$. Figure 5.7 is a plot of the fractional peak splitting F (left axis) and the center point contact conductance G_{qpc2} (right axis) vs. the center point contact voltage V_{qpc2}.[1] The saturation of the fractional peak splitting at a finite value as the interdot tunnel conductance goes to zero indicates a residual interaction between the dots that is not due to interdot tunneling. The residual interaction is substantially greater than the capacitive interaction observed in zero magnetic field.

---

[1] The point contact conductance has been laterally shifted to account for the effect of energizing the outer point contact gates to pinchoff; the point contact gates were calibrated as inducing a shift of about 2.5 mV in the positive direction for each 100 mV of additional negative voltage applied to the point contact gates.

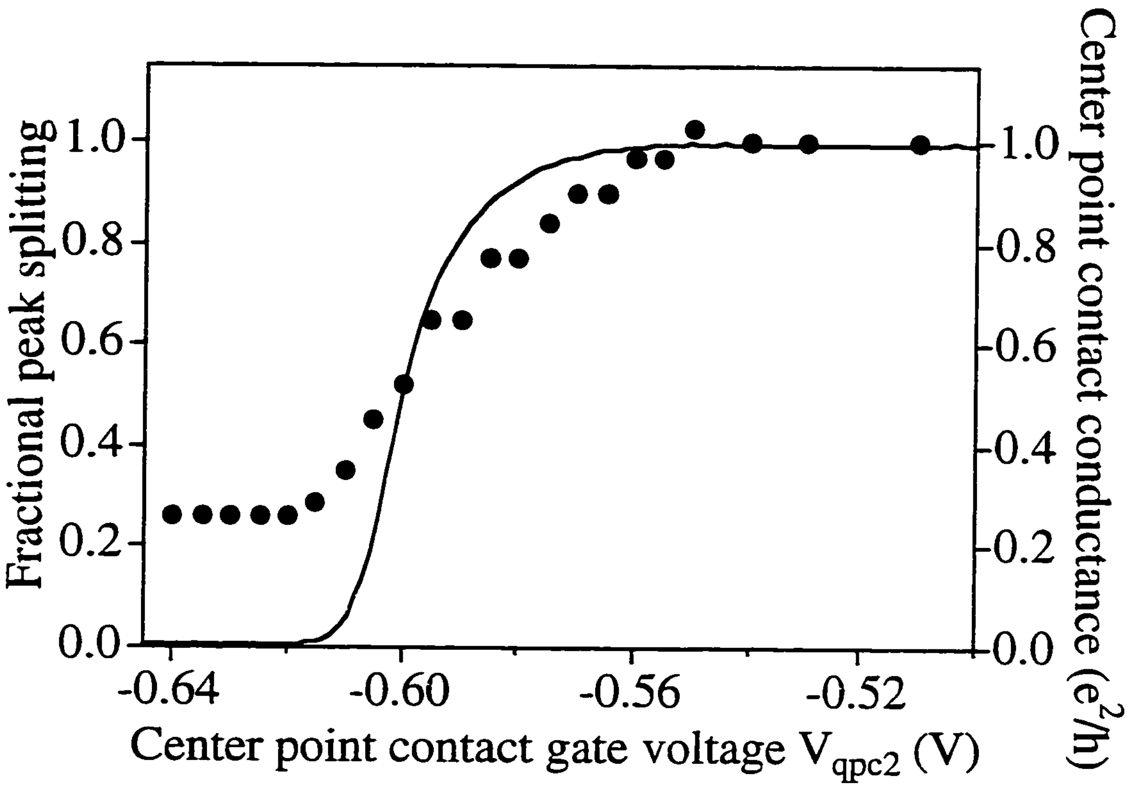

Figure 5.7 Fractional peak splitting (dots) and center point contact conductance (line) plotted vs. center point contact gate voltage. The conductance is laterally shifted to account for the influence of the other gates. The finite value saturation of the splitting at $G_{int} = 0$ reflects an interdot interaction besides electron tunneling.

Figure 5.8 plots the measured fractional peak splitting as a function of interdot tunnel conductance for three different filling factors: $\nu = 2$ (filled circles), $\nu = 3$ (open circles), and $\nu = 4$ (filled triangles).[2] Also plotted are theoretical calculations by Golden *et al.* [1996a; 1996b] of fractional peak splitting for the case of one conducting channel for the low and high interdot tunnel conductance limits. Matveev *et al.* find similar results [1996a]. The calculations have been scaled by an additional interaction energy to match the residual splitting, as described in Golden [1997]. The functional forms for the theory are given by

$$F \cong 0.1404 N_{ch} g + 0.1491 N_{ch} g^2 - 0.009798 (N_{ch})^2 g^2 + \dots \qquad (5.1)$$

for the low interdot conductance limit, with $N_{ch} = 1$, and

$$F \cong 1 - \frac{8e^{\gamma}}{\pi^2} \sqrt{1-g} \qquad (5.2)$$

for the limit of interdot conductance $g = G_{int}/(e^2/h)$ near one, where $\gamma \cong 0.577$ is the Euler-Mascheroni constant.

Again we note that for all three filling factors, the transition is complete when the interdot tunnel conductance $G_{int} = e^2/h$. For the $\nu = 2$ and $\nu = 3$ cases, it is not feasible to increase the interdot tunnel conductance to $G_{int} > e^2/h$ because the tremendous change in point contact voltage required to do so would either (a) bring the point contact out of depletion or (b) cause difficulties with cross capacitance. We can access $G_{int} \cong 2e^2/h$ for $\nu = 4$. We find that the charging diagram and fractional peak splitting remain saturated at their $G_{int} \cong e^2/h$ value as the interdot tunnel conductance increases to two edge channels in the constriction, in agreement with theory.

---

[2] The $\nu = 2$ and $\nu = 4$ data were measured on one cooldown; $\nu = 3$ was examined in the same sample on a separate occasion.

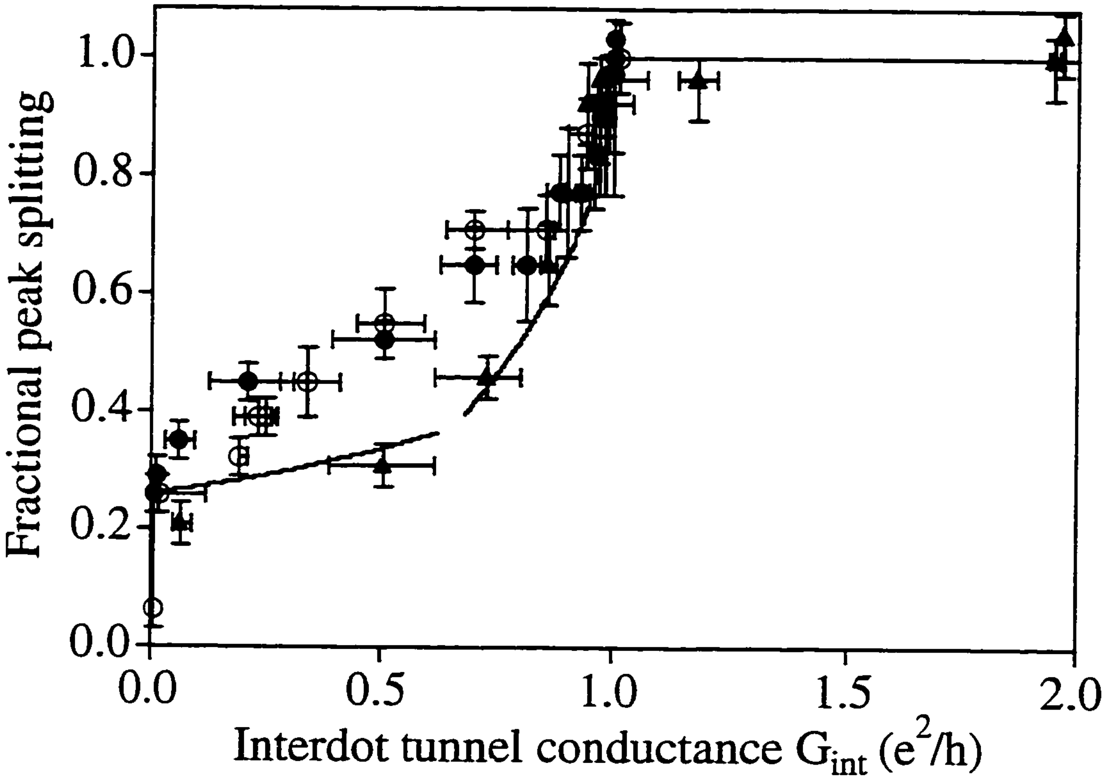

Figure 5.8 Fractional peak splitting plotted vs. interdot tunnel conductance G_{int} in units of e^2/h. Measured data are for $\nu = 2$ (filled circles), $\nu = 3$ (hollow circles), and $\nu = 4$ (filled triangles). Lines are theoretical fractional peak splitting calculated by Golden *et al.* for the low and high interdot tunnel conductance limits [1996a, b]; Matveev *et al.* find similar results [1996a, b]. The theory has been scaled to include an additional interaction energy that is not due to tunneling.

The saturation of splitting in the $\nu = 2$ measurements appears as a finite offset in splitting as the interdot tunnel conductance G_{int} goes to zero. The offset is apparent for all three filling factors, but it is less pronounced for $\nu = 4$ than for the other values.[3] In all three cases, the offset is much larger than in the zero field case. The observed interaction energy could reflect an increased interdot capacitance in the edge state regime; the splitting corresponds to an interdot capacitance $C_{int} \cong 120$ aF. This is roughly consistent with the interdot capacitance estimated from the slopes of the current-voltage characteristic boundaries in the strong field regime (100 aF - 150 aF). Estimates of the capacitance between two edge state lines of charge also produce a similar value of about 75 aF.

5.2 Double dot conductance as a function of magnetic field

The experiments of the preceding section demonstrate that transport through a double quantum dot changes dramatically in the presence of a perpendicular magnetic field. To better understand the effect of field, we have measured transport through a double quantum dot as a function of a strong and varying perpendicular magnetic field. These measurements are described in this section.

Studies of single quantum dots in strong, perpendicular magnetic fields have uncovered a rich variety of phenomena [McEuen *et al.*, 1991; McEuen *et al.*, 1992; McEuen *et al.*, 1993; Klein *et al.*, 1995; Klein *et al.*, 1996; Zhitenev *et al.*, 1997]. The lowest energy configuration of the system depends on field; for example, as magnetic field increases electrons may be redistributed from higher to lower Landau levels. The magnetic field scale of such redistributions is related to the change in field required to thread an additional flux quantum through the dot area. These events trace out changes in the lowest energy

---

[3] The one $\nu = 3$ point with very low splitting was measured from strongly suppressed peaks. The apparent lack of splitting may mean that one half of the split peak was shorter than the other and could not be seen in the noise.

configuration of the system and are clearly reflected in modulations of conductance peak height and variations in conductance peak position.

The present experiments use conductance through a double quantum dot as a similar probe of the energy and electron distribution of the double dot system. We use the same device as described in section 5.1, the asymmetric double quantum dot. The asymmetry is critical for this experiment because quantum dots of different sizes have distinct characteristic field scales for the addition of flux quanta to the dot area. The lithographic sizes of 500 nm x 600 nm and 500 nm x 800 nm combine with about 75 nm of depletion width beyond the gates to produce dot areas of about 0.158 μm^2 and 0.228 μm^2 respectively. With the device described above, the characteristic field scales for the individual dots, for the double dot as a whole, and for higher harmonics are all distinguishable.

Figure 5.9a is an inverted grayscale image of conductance measured through dot 1 alone, plotted vs. side gate voltage V_{g1} on the vertical axis and magnetic field on the horizontal axis. Figure 5.9b is a similar image of dot 2 conductance plotted vs. side gate voltage V_{g2} on the vertical axis and magnetic field on the horizontal axis. Such images have been observed previously, as noted above; we include them as a calibration for our double dot device. The data were obtained by repeatedly measuring dot conductance as a function of side gate voltage using the automated data acquisition system. The magnetic field was continuously varied by an Oxford magnet power supply. The field is approximately 3.2 T, corresponding to a bulk filling factor $\nu = 4$. Both the height and the position of the conductance peaks vary with magnetic field; the peaks move in a zigzag pattern that correlates with the peak height modulations. The peaks move gradually as the magnetic field shifts the energy of the dot. The sudden returns to the initial peak position signal that electrons have been redistributed to minimize the energy. The pronounced peak height modulation indicates that redistribution affects the accessibility of states in the dot.

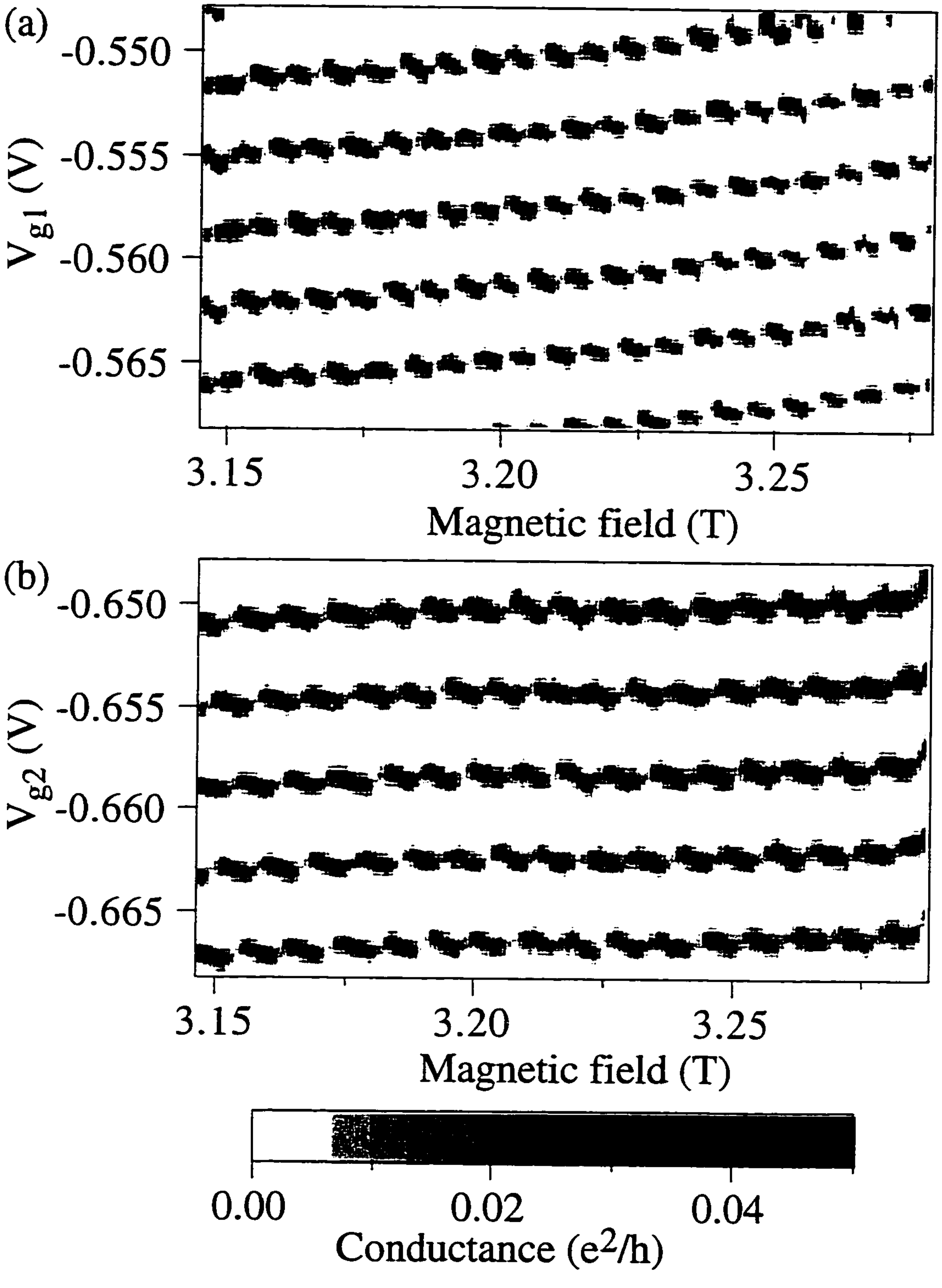

Figure 5.9 Measured conductance of (a) dot 1 and (b) dot 2 as a function of side gate voltage on the vertical axis and magnetic field on the horizontal axis. Conductance peak heights and positions vary with magnetic field.

Note also the alternating pattern of tall and short peaks, a possible indication of the addition of alternate spins.

The period of the oscillations at $\nu = 4$ is 6.6 mT for dot 1 and 8.75 mT for dot 2. We can calculate the period corresponding to threading one flux quantum through the known dot areas from the relation $\Delta B A_{dot} = h/e$. With a total 150 nm depletion width as assumed above[4], this yields periods of 18.2 mT for dot 1 and 26.2 mT for dot 2. The calculated periods are 2.8 and 3.0 times the observed periods for dots 1 and 2 respectively. Similar measurements at filling factor $\nu = 3$ yield periods of 8.3 mT for dot 1 and 11.5 mT for dot 2. The calculated periods are 2.2 and 2.3 times the observed periods at $\nu = 3$. The decreasing period with increasing filling factor is consistent with the large number of ways that electrons can redistribute themselves among many Landau levels.

We have made corresponding measurements on the entire asymmetric double dot. All ten gates were energized to place the double dot in the Coulomb blockade regime, with the value of the interdot tunnel conductance calibrated by the measurements described in the previous section. We used the computer to repeatedly measure conductance through the entire double dot as a function of the side gate voltages $V_{g1} = V_{g2}$ while varying the magnet current continuously. We repeated this measurement for a series of interdot conductances ranging from $G_{int} \cong 0$ to $G_{int} \cong 2e^2/h$.

Figures 5.10a-c plot double dot conductance in inverse grayscale as a function of the side gate voltages $V_{g1} = V_{g2}$ on the vertical axis (corresponding to a diagonal slice through the charging diagram) and the magnetic field on the horizontal axis. Figure 5.10a corresponds to $G_{int} \cong 0.20\ e^2/h$. A vertical slice through the data reveals the series of narrowly split peaks that we expect for a double dot with low interdot conductance. As the magnetic field is varied, these peaks evolve in both position and height. The structure is qualitatively similar to that for the single quantum dots; peak amplitude is strongly

---

[4] This depletion width varies some with applied gate voltage and is not truly a constant. Variations are small enough to make this approximation reasonable for dots of this size.

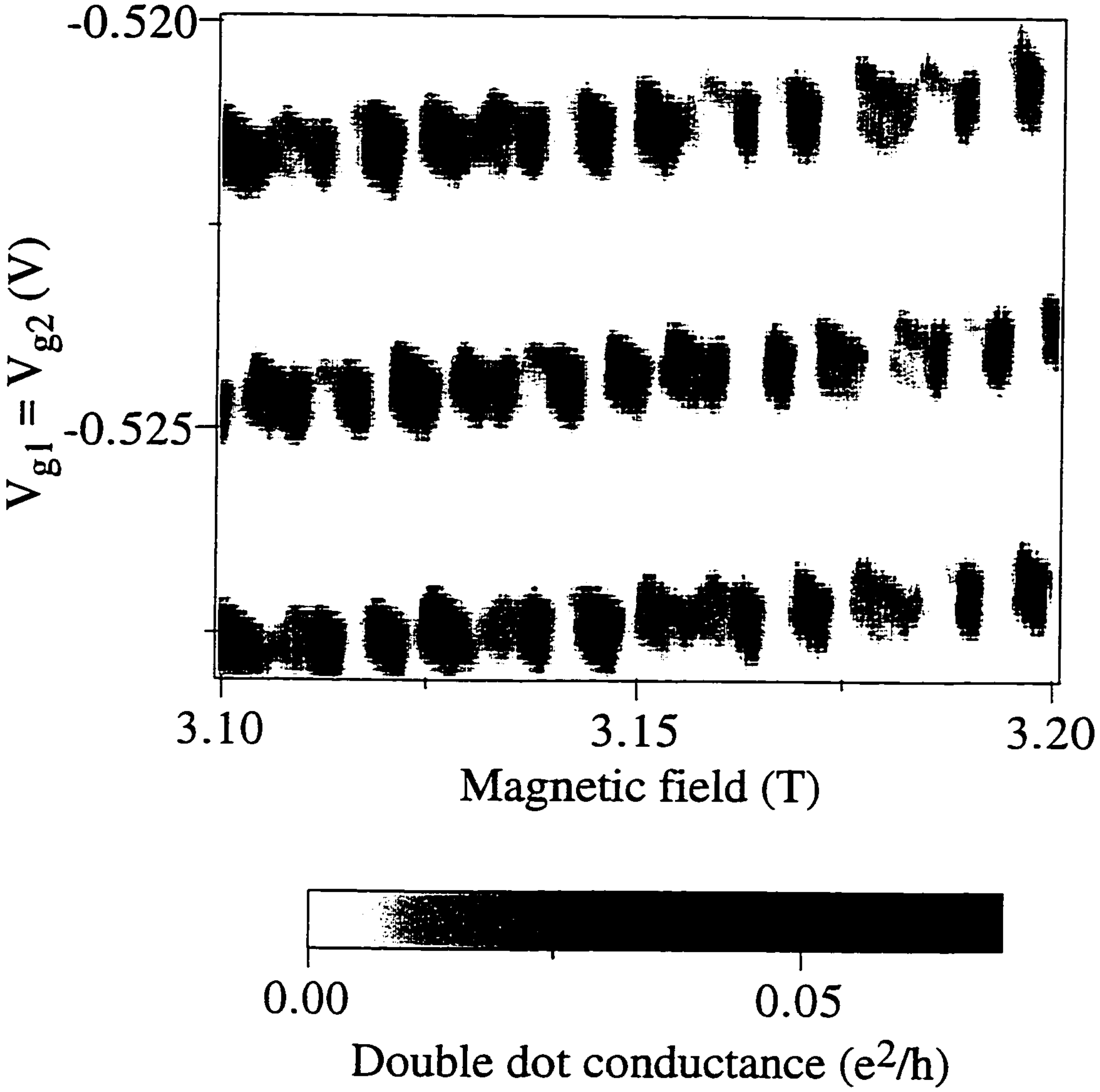

Figure 5.10 (a) Inverted grayscale image of double dot conductance measured as a function of $V_{g1} = V_{g2}$ and perpendicular magnetic field. Interdot tunnel conductance $G_{int} \cong .20\ e^2/h$.

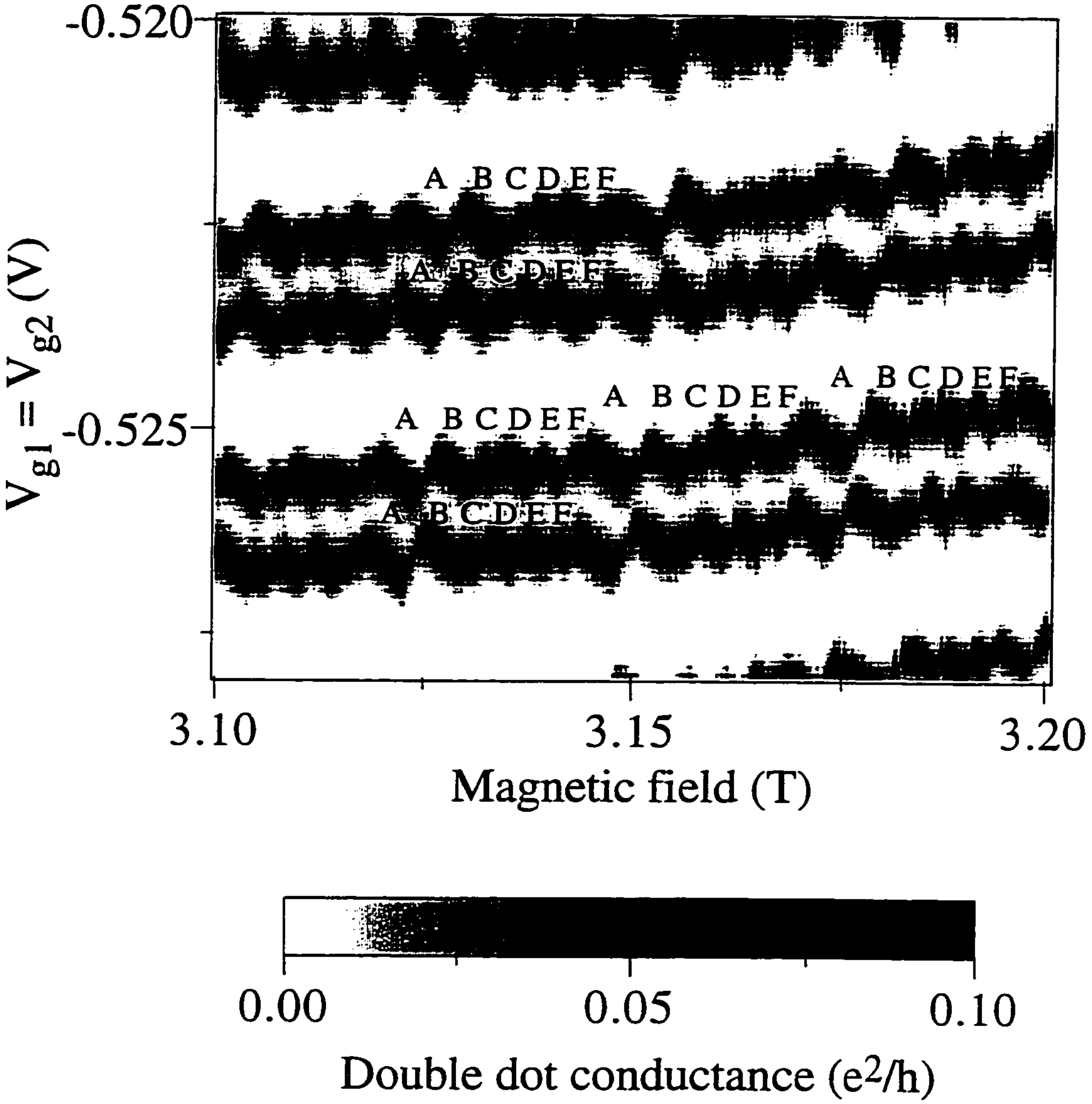

Figure 5.10 (b) Inverted grayscale image of double dot conductance measured as a function of $V_{g1} = V_{g2}$ and perpendicular magnetic field. Letters A, B, C, D, E, and F mark the peak position shifts that compose a repeating segment. Interdot tunnel conductance $G_{int} \cong 0.85\ e^2/h$.

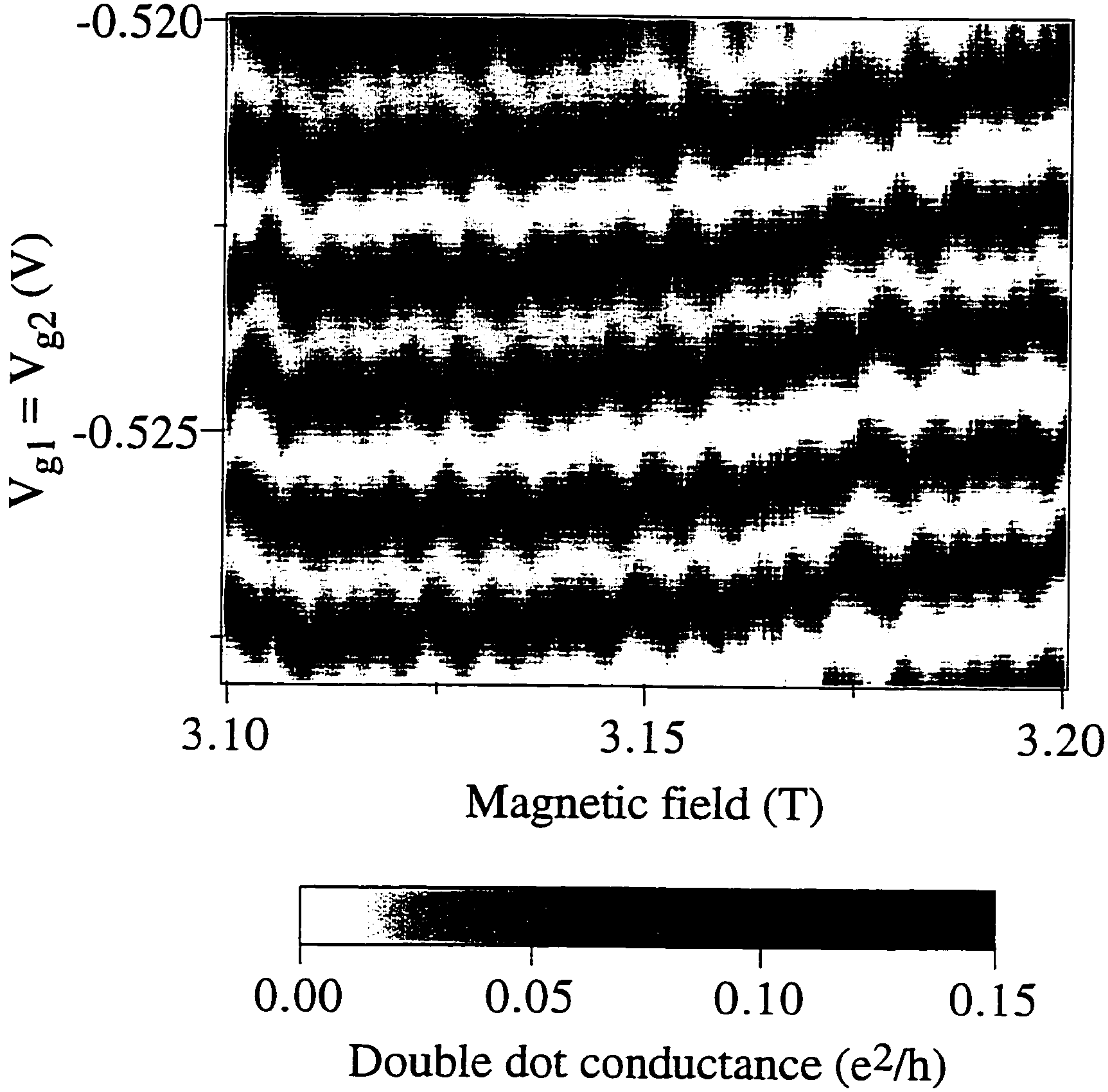

Figure 5.10 (c) Inverted grayscale image of double dot conductance measured as a function of $V_{g1} = V_{g2}$ and perpendicular magnetic field. Interdot tunnel conductance $G_{int} \cong 1.03\ e^2/h$.

modulated, and we retain a zigzag pattern in the peak positions. Unlike the single dot case, conductance is suppressed over ranges of magnetic field, producing blank spaces in the zigzag pattern. The zigzags are no longer even, but at this small splitting it is difficult to distinguish the details of the peak evolution.

The pattern is easier to discern in figures 5.10b and c, which correspond to interdot conductances of $G_{int} \cong 0.85\ e^2/h$ and $G_{int} \cong 1.03\ e^2/h$ respectively. Comparing the two component peaks that comprise a single split peak, we see that the shifts in peak position track each other closely. Furthermore, the shifts form a pattern in which a given segment repeats with magnetic field. The repeating segment consists of six distinct peak position shifts, which are marked in figure 5.10b by the series of letters A, B, C, D, E, and F. This sequence appears in similar form in figure 5.10c and also in measurements with G_{int} near $2e^2/h$. In figure 5.10b, we see about four repetitions of the pattern as we track a given peak in magnetic field; measurements over a broad field range confirm that the pattern continues to repeat.[5] The length of the repeated segment is measured at 25.6 mT, which is 3.9 ± 0.1 times the observed period for dot 1 and 3.0 ± 0.2 times the measured period for dot 2.[6] The periods are nearly constant with changing interdot tunnel conductance; small variations are expected because the dot areas change as the center point contact voltage is adjusted.

The repeating pattern is also maintained from one pair of split peaks to the next, but the corresponding peaks do not occur at exactly the same magnetic field. Figures 5.10b and c show that the pattern repeats at higher magnetic field and at less negative gate voltage (or at lower magnetic field and more negative gate voltage). The pattern is shifted both within a given peak pair and between neighboring pairs, for an overall visual effect of sloping bands of corresponding peaks. The sign of the slope makes sense, if we interpret correspondence

---

[5] At a higher filling factor ($\nu = 5$), the pattern appears to change, as one would expect. A different Landau level structure minimizes its energy through a different series of depopulation events.

[6] The observed periods for the individual dots shifts when the full double dot is energized because of cross capacitance from the additional gates. The resulting periods are 6.55 ± 0.15 mT for dot 1 and 8.55 ± 0.5 mT for dot 2.

of peaks as meaning that the double dot has similar structure at those values of field and gate voltage. Increasing the field decreases the spatial size of the flux quanta and packs the electrons more tightly. Adding additional charge compensates by increasing the radius.

The consistency of the pattern indicates that there is a specific sequence of adjustments in the electron distribution that minimizes the energy of the system as additional flux quanta are added. The energy minimization sequence appears independent of the exact number of electrons or flux quanta (for a given filling factor). Experiments on single dots have found that transport features may correlate over ranges of magnetic field or gate voltage [see for example Zhitenev *et al.*, 1997; Stewart *et al.*, 1997]. It is noteworthy that the more complicated double dot system also locks into a long range pattern.

Figure 5.11 illustrates a likely source of the observed pattern of double dot conductance modulations. Recall that the conductance peaks for individual dots shift and undergo peak height modulations as the magnetic field varies. This behavior is shown schematically by the sets of solid lines labeled dot 2 and dot 1, which represent conductance peaks; the peaks shift at different frequencies for the two different sized dots. If we superpose these two structures, postulating that the double dot conductance is modulated each time a single dot undergoes a conductance modulation, we obtain the pattern shown in the third line. This pattern is similar to the observed double dot conductance pattern, and segments are marked with the letters A - F.

The repeated pattern of double dot conductance modulations suggests a frequency locking effect. In the simplest picture of non-interacting dots, the pattern would repeat only to the extent that the two periods have a rational ratio. The measured ratio of the periods of the two dots is 0.77 ± 0.06, which is approximately a rational ratio of three to four. It would be possible to observe a robust pattern if the periods had a perfect rational ratio, but the periods do vary with changing gate voltages. A more likely explanation is a frequency locking effect, in which the double dot conductance modulations are not just the sum of the single dot modulations. Rather, interactions between dots could lock the double dot

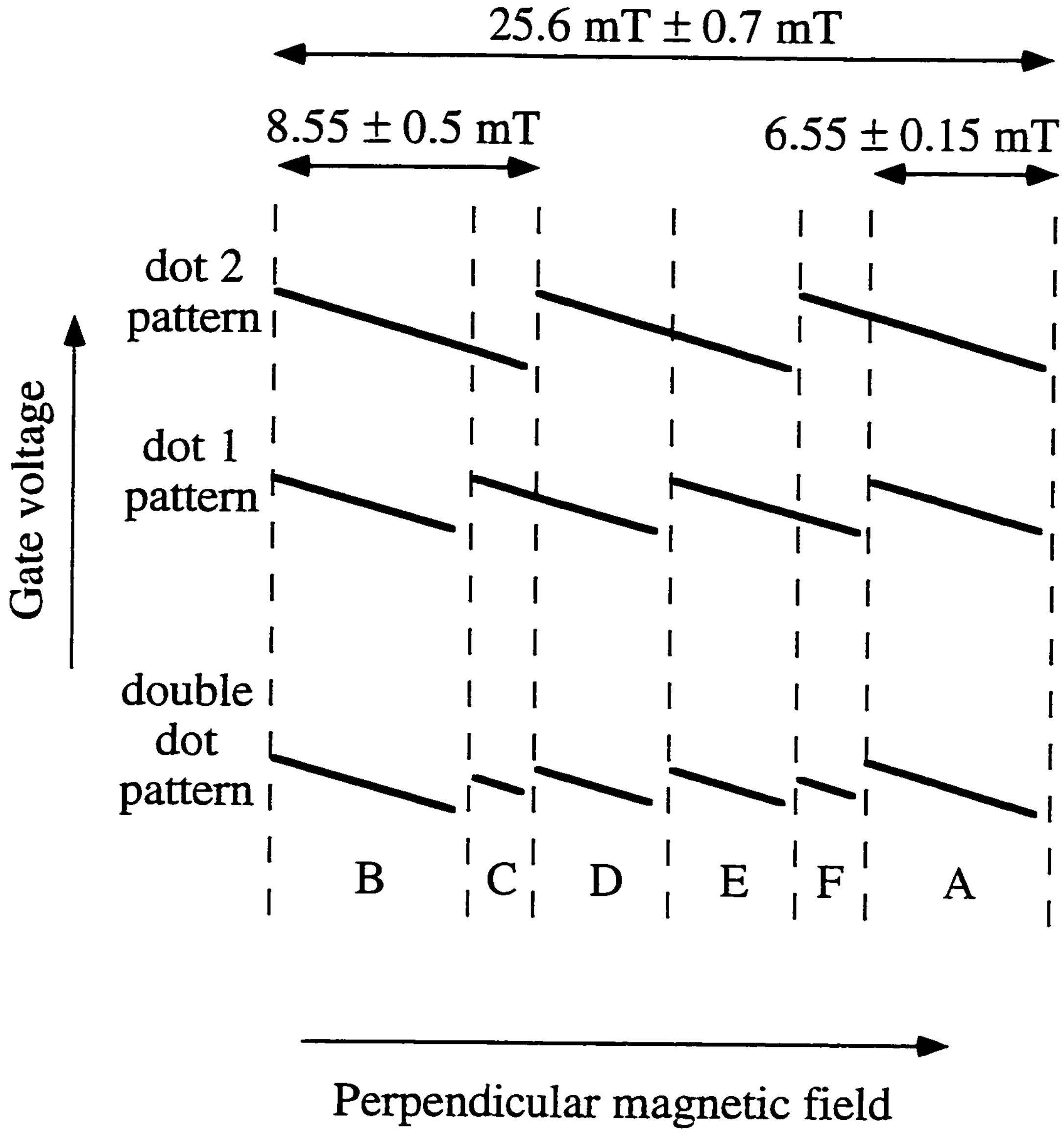

Figure 5.11 Schematic diagram of the formation of the double dot conductance peak pattern. Thick lines represent conductance peaks for dot 2, dot 1, and for the double dot. As in the data, the vertical axis is gate voltage, and the horizontal axis is perpendicular magnetic field; the three cases are offset from each other for visibility. The periods of conductance modulation for the individual dots are known from experiments to have a near 3:4 ratio. The double dot pattern shown here would result if the double dot conductance peaks undergo a shift and modulation each time the conductance of an individual dot is modulated. The pattern of double dot modulations is in qualitative agreement with the observed pattern. The pattern would repeat either if the single dot periods have a perfect, rational 3:4 ratio or if a frequency locking effect drives them to a common frequency.

conductance variations onto the frequency that corresponds to a near (but not quite) rational frequency ratio. This possible frequency locking behavior merits further study.

The sloping bands of peaks account for the occasional anomalous splittings observed in the charging diagrams of the preceding section. Depending on the exact magnetic field and gate voltage, a diagonal slice through the charging diagram may cross a region where the split peaks are zigzagging in tandem. Because of the horizontal (magnetic field) offset between corresponding zigzags, it may also catch a region where one peak is moving up and the other down, which causes the anomalous splittings.

As the interdot conductance increases, we expect the double dot to behave increasingly like a single large dot, in which electrons may be readjusted among Landau levels when flux quanta are added to the combined area of the two dots. Such processes would take place on a shorter magnetic field scale, corresponding to the larger area. A visual examination suggests that figure 5.10a, with its small interdot conductance, has fewer rapid oscillations than figures 5.10b and c, with their higher interdot conductance. We quantify the frequency of the peak modulations by taking power spectra. To be unbiased in our choice of representative data, we take spectra in magnetic field for each gate voltage value and average them together to get a spectrum for the entire diagram.

Figures 5.12a-c plot three power spectra vs. inverse change in magnetic field for interdot tunnel conductances $G_{int} \cong 0.20\ e^2/h$, $0.85\ e^2/h$, and $0.98\ e^2/h$ respectively. The peaks corresponding to the periods of the two dots are marked. The combined area peaks occur precisely at the sum frequency and are also marked. The combined area peak is suppressed relative to the individual dot peaks in figure 5.12a but increases in relative magnitude for larger interdot tunnel conductance.

The power spectra make it clear that short field scale features that correspond to the entire dot area are present. We are, however, limited in what we can glean from the relative magnitudes of the peaks. Figure 5.12 suggests that the height of the peak corresponding to the entire dot area increases as interdot tunnel conductance joins the dots together.

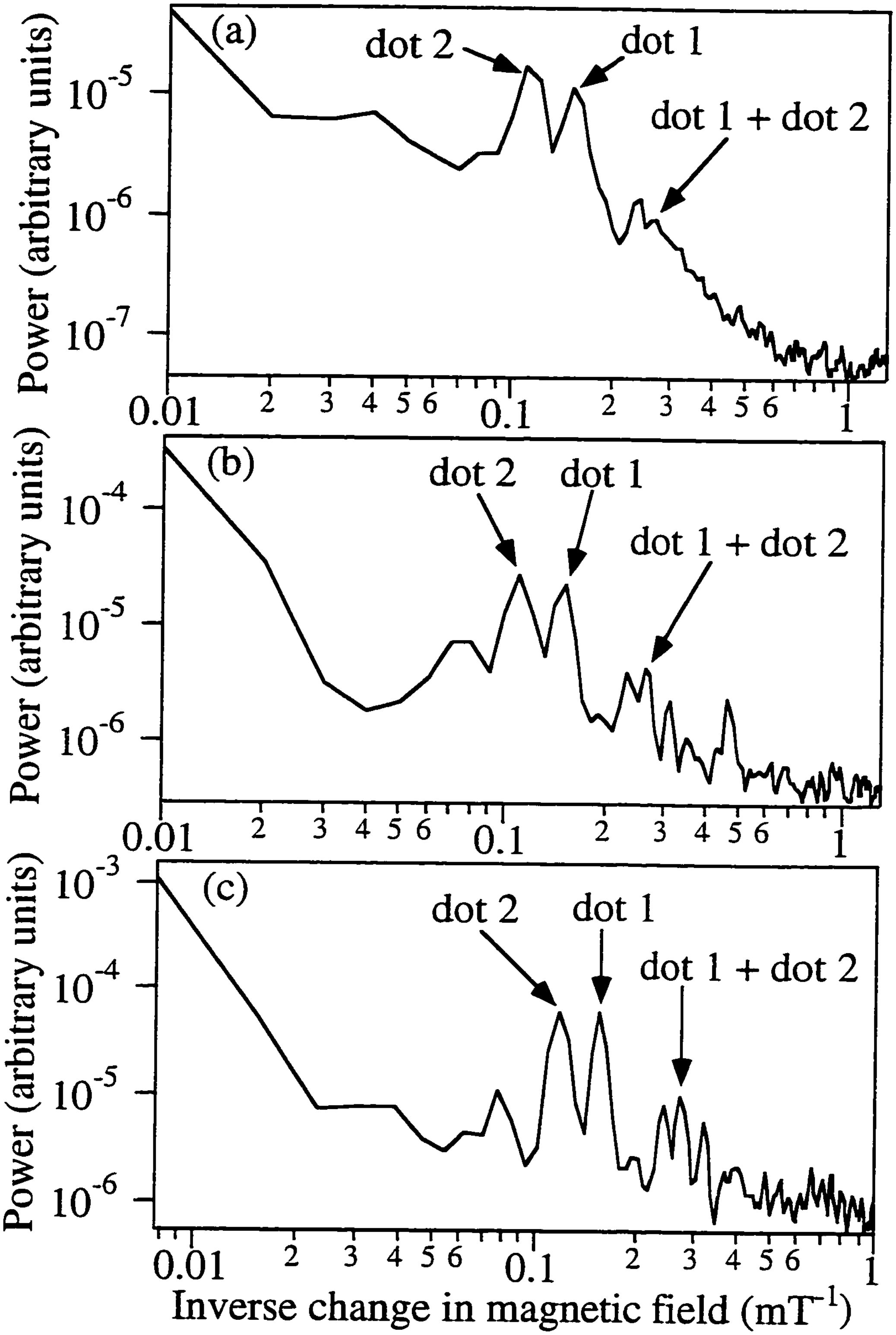

Figure 5.12 Power spectra of the double dot conductance vs. magnetic field, averaged over measured values of $V_{g1} = V_{g2}$ for interdot conductance (a) 0.20 e^2/h, (b) 0.85 e^2/h, and (c) 0.98 e^2/h.

Unfortunately, there is a second factor that contributes to the observed pattern: the degree to which $V_{g1} = V_{g2}$ crosses the points of narrowest splitting in the charging diagram. If the gate capacitances C_{g1} and C_{g2} are poorly matched, varying $V_{g1} = V_{g2}$ does not produce a diagonal slice through the diagram. Even when $V_{g1} = V_{g2}$ is diagonal, as in this case, the background charge can shift that diagonal line so that it passes between sets of points. This difficulty has been noticed in previous experiments [Waugh, 1994]. When this occurs, the observed splitting is broader, and pairs of peaks correspond to the Coulomb blockade being lifted first for one dot and then for the other rather than being lifted for both dots simultaneously.

Figure 5.13 is an inverted grayscale image of conductance through a double dot for which $V_{g1} = V_{g2}$ misses the points of minimum splitting. The vertical axis is again the gate voltage $V_{g1} = V_{g2}$, and the horizontal axis is magnetic field. The oscillations of pairs of peaks are not locked together in this case; rather, the two peaks exhibit the distinct frequencies of dot 1 and dot 2. A visual assessment of these data is accurate; the power spectrum does not pick up a component corresponding to the total area of the entire double dot.

When $V_{g1} = V_{g2}$ misses the points of minimum splitting in the charging diagram, it is often more subtle than in figure 5.13 and manifests itself as a peak splitting that is just slightly too large. Such subtle off-diagonality also reduces the magnitude of the peak corresponding to the combined dot area. To quantify the magnitude of the different frequency components, one would need to ensure that the data cut directly through the point of minimum splitting. For the data described here, the results include a convolution of the two effects.

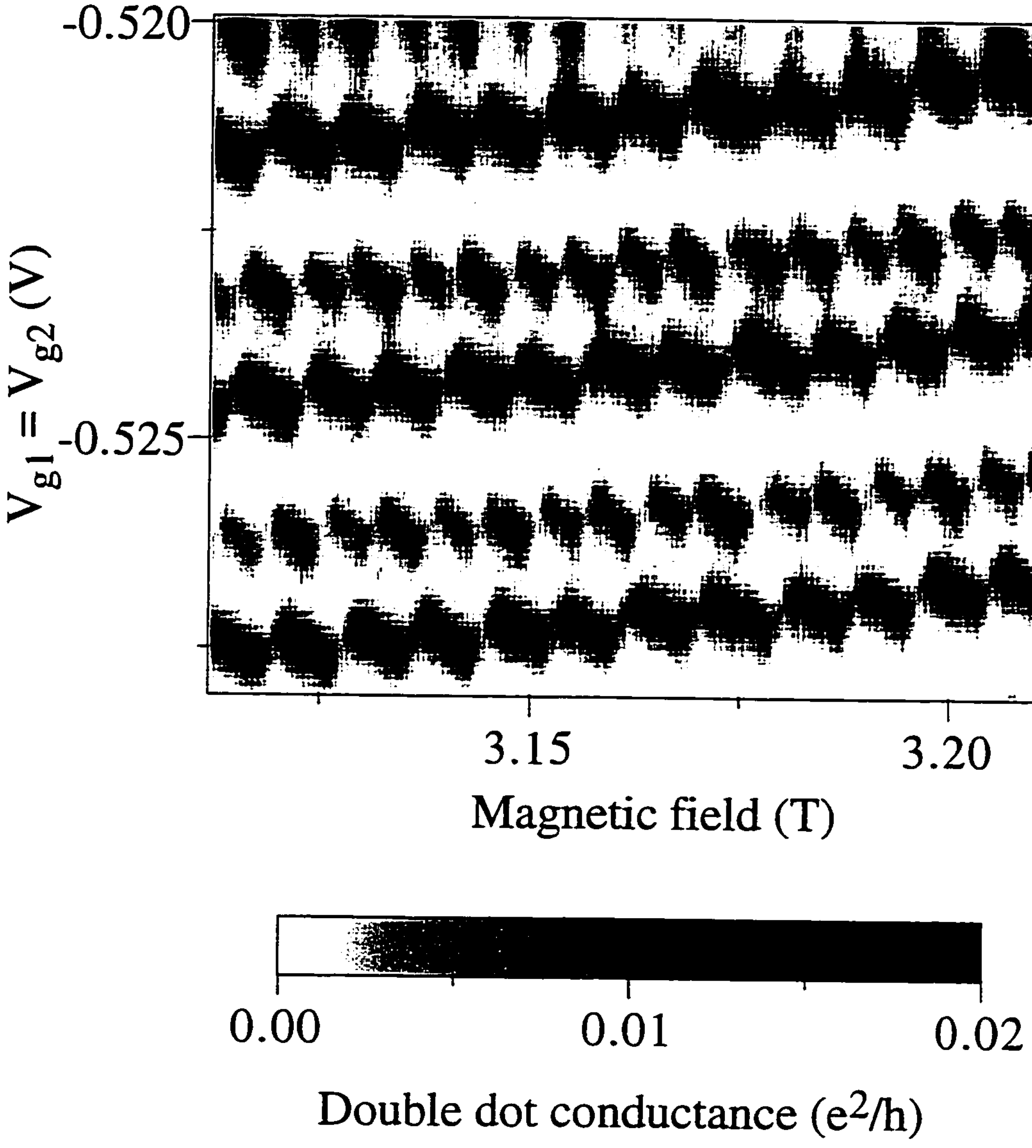

Figure 5.13 Inverted grayscale image of conductance through a double dot plotted as a function of side gate voltages on the vertical axis and magnetic field on the horizontal axis. Each peak zigzags with the characteristic frequency of one of the constituent dots. This reflects the fact that the gate voltages do not follow the line of minimum peak splitting through the charging diagram. Interdot conductance $G_{int} \cong 0.66\ e^2/h$.

Chapter 6

Conclusions and Future Directions

In this thesis we have used Coulomb blockade spectroscopy to study systems of coupled quantum dots and the effects of interactions among dots. For our devices, we find that electron tunneling dominates interdot interactions. We have quantified the effects of electron tunneling by measuring the charging diagram and interaction energy as we progressively join two dots via electron tunneling channels. This is analogous to forming an "artificial molecule" from two separate "artificial atoms" by introducing charge sharing. In the process, we have seen how the effects of charge quantization in many body systems are reduced by electron tunneling, with the complete destruction of quantization effects for an interdot tunnel conductance of two conductance quanta, or $2e^2/h$.

We have also used the Coulomb blockade to study how the behavior of a coupled quantum dot system depends on the perpendicular magnetic field. The existence of Landau levels and edge states in a strong field has pronounced consequences for tunneling interactions and transport in coupled quantum dots. We have observed the destruction of quantization effects at an interdot tunnel conductance of one conductance quantum, or e^2/h, in the strong field regime, as well as an increase in residual interaction energy. Finally, we have examined how transport through a double dot changes with small variations of the magnetic field; this reflects how the electron distribution is adjusted to minimize the energy of the system. We have observed that for sufficient interdot tunneling, electron redistributions occur in a precise pattern that repeats with changing field and with the addition of charge to the system. The robust periodicity suggests a frequency locking effect.

There are several promising directions for future studies of coupled dots. The first is directly related to the magnetic field measurements in chapter 5, in which we observed the minimization of double dot energy by electron redistribution. It would be interesting to examine such patterns at different values of the filling factor ν with the goal of understanding the detailed sequence of redistribution events. One could ask whether the repeating patterns correspond to a frequency locking effect and how strongly the system locks for different dot periods and degrees of interdot interaction. One could use lower density material and look at lower filling factor, where the list of possible redistribution events is shorter and the observed patterns could be correspondingly less complex.

One could also look at spin dependent transport, which would be relevant, for example, for the quantum computing proposal of Loss *et al.* [1997]. Possible experiments include additional high field work, the measurement of smaller devices, and examination of different configurations of quantum dots, such as ring structures. Phase coherence is another issue that remains to be addressed. Single dot phase coherence has been examined using interferometer devices [Yacoby *et al.*, 1995; Schuster *et al.*, 1997], but how well phase coherence is maintained during transport through systems of coupled dots remains an open question.

Appendix A

Automated Data Acquisition System

The fast data-taker is a combination of hardware and software that controls two voltages in an experiment and measures up to eight quantities as a function of those voltages. Measurement and control occur in two separate circuits synchronized by digital timing signals. A National Instruments MIO-16X board controlled by LabView measures voltages by direct 16-bit A/D conversion; a National Instruments DIO-32F board controlled by LabView drives two 18-bit D/A converters (AD1139K).

The fast data-taker can operate in any one of three modes. First, it can vary one voltage (the sweep) from a pre-defined initial value to a pre-defined final value, measuring up to 8 quantities as a function of the sweep voltage. This mode is rarely used, since Read N DMMs performs the same task better under most circumstances. Second, it can perform that same operation repeatedly, for example while some other parameter is adjusted either continuously or by hand. This is useful for tuning devices. Third (and most commonly), it can vary two voltages in a raster pattern, incrementing the second (step) voltage between sweeps. This mode acquires two-dimensional blocks of data at much faster speeds than are possible manually. A measurement that took five hours manually can be performed faster (ten minutes) and with much better resolution. The increase in speed often makes it possible to beat charge noise.

Hardware

The hardware is shown schematically in chapter 3, where the fast data-taker was briefly discussed. A Power Macintosh 7100/80 computer houses three National Instruments data acquisition boards, the MIO-16X, the DIO-32F, and DMA-2800. The MIO-16X does timing and A/D conversions. The DIO-32F provides digital inputs to the external D/A converters. The DMA-2800 permits direct memory access, so the computer can output a predetermined sequence of values with strict timing.

An external box (the "output box") contains the AD1139K D/A converters and their associated circuitry. Digital input from the DIO-32F enters the output box through a ribbon cable. Each line goes through a TTL to CMOS high-speed optocoupler (Quality Technology's 74OL6010); the high signal is brought up to 5 V by 5 kΩ pull-up resistors. The digital signals then go to the D/A converters. The resulting analog signal is buffered and emerges from the box. Also entering the output box are the timing signals generated by the MIO-16X to synchronize the data acquisition. The timing directs signals to the appropriate D/A converter and instructs the D/A modules when it is time to perform a conversion. The output box is powered by a set of +24 V, +12 V, -12 V, and -24 V batteries with a common ground and a +12 V battery with a separate ground.

The channels to be measured pass through a small Pomona box (the "input box") with eight differential signal lines entering from the sample via BNC connectors and leaving to the computer via twinax and ribbon cable. Differential lines 0 through 3 are for measuring floating signals; their ground lines are tied to the computer's analog ground by 100 kΩ resistors to protect the board inputs. Differential lines 4 through 7 are for measuring signals referenced to ground. Because they lack resistors to ground, ground loops are minimized.

Figure A.1 summarizes the circuitry that follows the output box. First is an optional voltage divider. The D/A converters have a voltage range of ±10 V; the minimum step size before division is 76 μV. With the divider, one may put out a larger signal than is needed and divide it down, improving resolution and minimizing noise. The "diode protection box" follows the divider and uses crossed diodes to limit the voltage applied to the sample. (The default output of the external voltage control circuitry is +10 V, which will destroy the vast majority of our samples; thus limiting positive voltages is particularly useful.) The

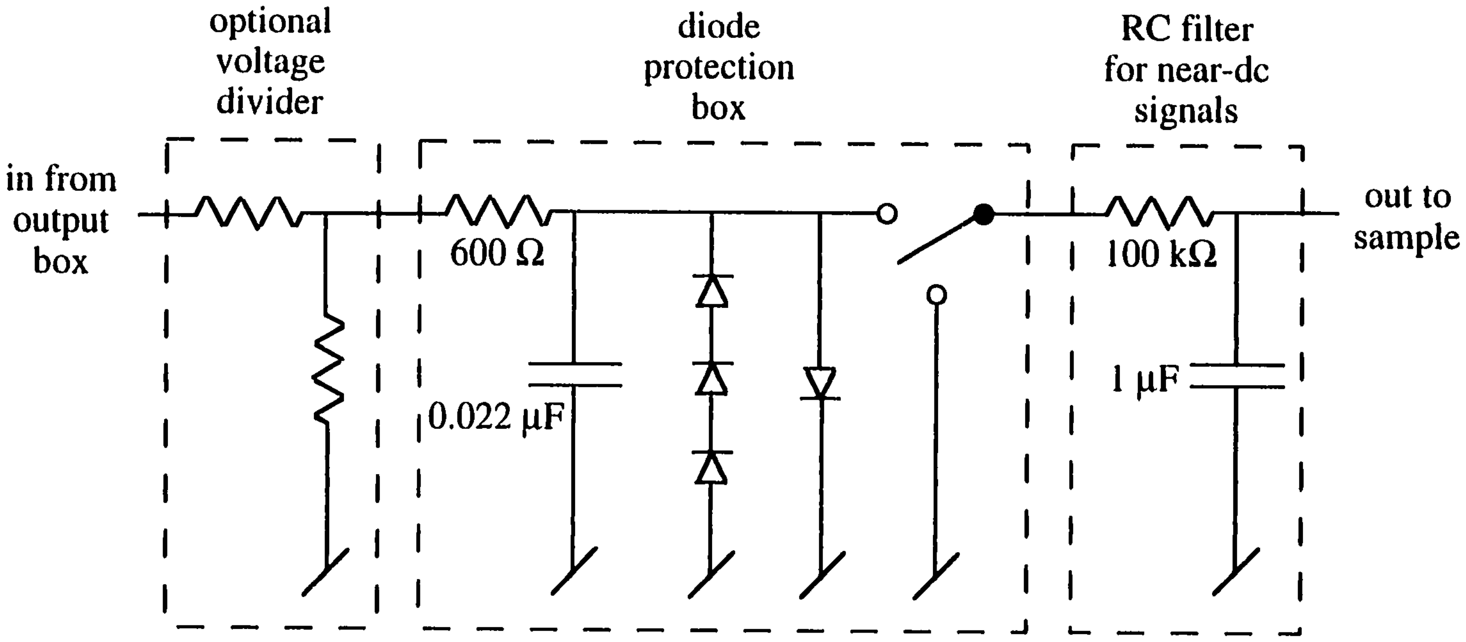

Figure A.1 Diagram of the protective circuitry that shields the sample from damaging signals from the output box. The optional voltage divider improves effective resolution and divides down noise. The diode protection box includes a high frequency RC filter, crossed diodes to limit large positive or negative signals, and a make before break switch to connect the sample to either the output signal or ground, as appropriate. The final RC filter is used for near dc signals and effectively rounds voltage steps or spikes that could otherwise damage the sample.

diode protection box also incorporates an RC filter with an RC time constant of 13 μs to help limit voltage spikes. The third component of the diode protection box is a make before break switch that connects the sample either to ground or to the output voltage. The final box is an RC filter with a low frequency rolloff, which provides additional protection against voltage spikes in near dc signals.

Software

The software is a LabView program called, in its most recent iteration, "fast data-taker 5-13-97". The program is documented in Figure A.2 at the end of the appendix.

Operating instructions

1. Connect the DIO-32F port on the back of the computer to the output box with the ribbon cable. Connect the MIO-16X port on the back of the computer to the input and output boxes using the bundled twinax cable.
2. Connect the output signals ("sweep axis to sample" and "step axis to sample") from the output box to appropriate voltage dividers and then to the diode protection box input. The diode protection box should be grounded. The output of the diode box goes to the sample, the measurement channels, a multimeter, etc. Filter the signals before they hit the sample. Finally, before the voltages go to the sample, pass them through an RC filter.
3. Connect the signals to be measured to the input box.
4. Plug the fully charged batteries into the output box.
5. Verify the NI-DAQ control panel settings. Set the MIO-16XL to ADC with bipolar, differential 20 V inputs and 42 μs speed. The channel gains may be chosen to match the signal size. For signals smaller than 1 V, a gain of 10 is appropriate, while larger signals require a gain of 1. Set the DIO-32F channels for latched output.

6. Set the software parameters.

Channel: the numbered port on the input box to which you attached a signal to be measured.

Gain: the numerical factor by which your signal should be divided to put it in your desired units.

Initial and final sweep voltages: self explanatory, in Volts.

Voltage between points: self explanatory, in milliVolts.

Time between points: usually set at 30 ms or 10 ms, with comparable lockin time constant.

Number of time to average each data point: best set to one. Use a lockin amplifier to do your averaging.

Single scan/repeated scan/2D scan: sets mode to single, repeat, or raster scan.

Initial and final step voltages: self explanatory, in Volts.

Voltage between points: self-explanatory, in milliVolts.

File save parameters: must be set prior to starting the program. Insert a semicolon before the file name.

If you want to save the step values....: gives you the option of recording the value on the step axis for posterity. Set to "no" to prevent the computer from crashing from lack of memory, and note the voltage range by hand.

Y axis, X axis: identifies the data to be plotted on the graph by stating the index of those quantities in the Measurement parameters array.

Use array of graphs?: Set to "no".

Go/Pause: pauses data acquisition between sweeps but not during sweeps.

Plot options: permit you to display y vs. x, y vs. index, etc. Index plots usually look best.

7. Leaving the diode protection box on "ground", float your sample and set all of the non-computer controlled gates to their proper values. Use a lockin amplifier if you would

normally do so. Start the program. The computer will prompt you when it is time to set the diode protection box to "connect". Following the instructions protects your sample. Either let the program run to completion or stop it using the big stop button on the front panel. Do not stop the program with the hard-wired LabView stop button, or it will shock your sample with +10 V and fail to reset the boards.

8. Process the data. The data are saved in one large file with alternating columns of the parameters that you told the computer to measure. The utility "table eaten data" in LabView transforms two alternating columns into a solid table composed of one set of columns (the data that you wanted). It may then be imported into Igor or SpyGlass.

Troubleshooting

1. There is 0 V coming out of the output box, and I expected to see the default +10 V.

   Check that batteries are plugged in and battery fuses are intact.

2. There is a random voltage coming out of the output box, and I expected to see the default +10 V.

   Check that batteries are adequately charged.

   Try running Device Reset.vi on both the MIO-16X and DIO-32F boards.

   Check that the optocouplers in the output box are functional.

3. The software gave me an error that it wasn't measuring anything and I was wasting my time.

   This is an unexplained bug. Try adjusting the initial, final, and increment voltages so that they are not such round numbers (i.e. -1.000 V changes to -1.013 V).

4. After I started the program, it took forever to start measuring anything.

   The program takes a long time to set itself up if the sweep is very long. Try reducing the number of sweep points.

5. The program finished taking all the data and then crashed.

For some reason you ran out of memory. If you are currently looking at an error message or if the computer is hung up and has been for some time, then turn the switch on the diode protection box to ground. Then press the LabView stop button (not the usual stop button).

There is a switch on the front panel that says, "If you want to save the step values, set on yes." When it is set on yes, the program opens the data file and moves numbers around after the measurements are all complete. This is memory intensive and can result in this type of crash. If you set the switch on no, this crash is less likely, though you can still crash if you try to take too much data. If the memory limitations cramp your style, buy more.

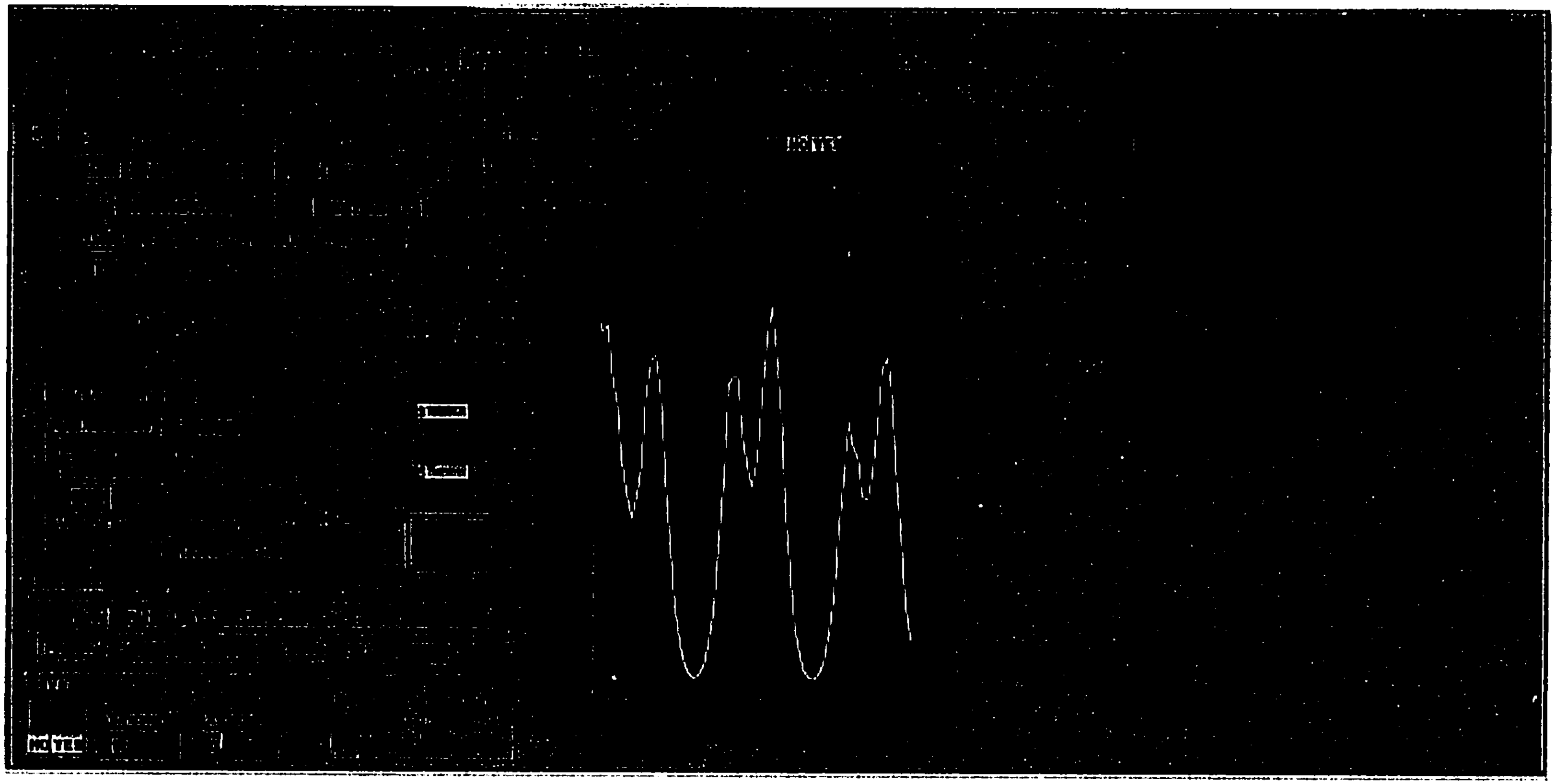

Figure A.2 Documentation of the LabView program "fast data-taker 5-13-97", which controls the high speed data acquisition hardware.

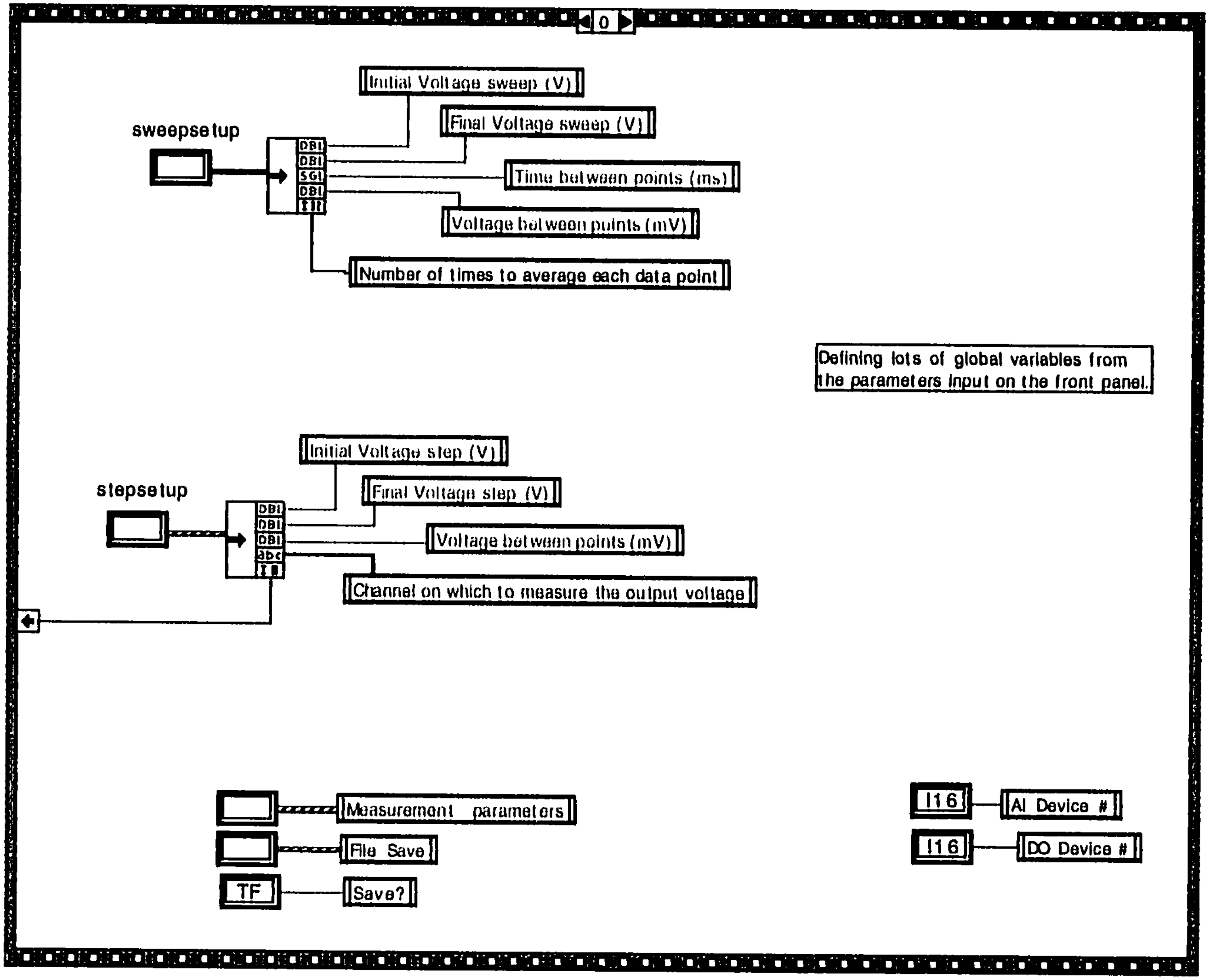
0
sweepsetup
DBl
DBl
SGl
DBl
I16
Initial Voltage sweep (V)
Final Voltage sweep (V)
Time between points (ms)
Voltage between points (mV)
Number of times to average each data point
Defining lots of global variables from the parameters input on the front panel.
stepsetup
DBl
DBl
DBl
abc
I8
Initial Voltage step (V)
Final Voltage step (V)
Voltage between points (mV)
Channel on which to measure the output voltage
Measurement parameters
File Save
TF
Save?
I16
AI Device #
I16
DO Device #

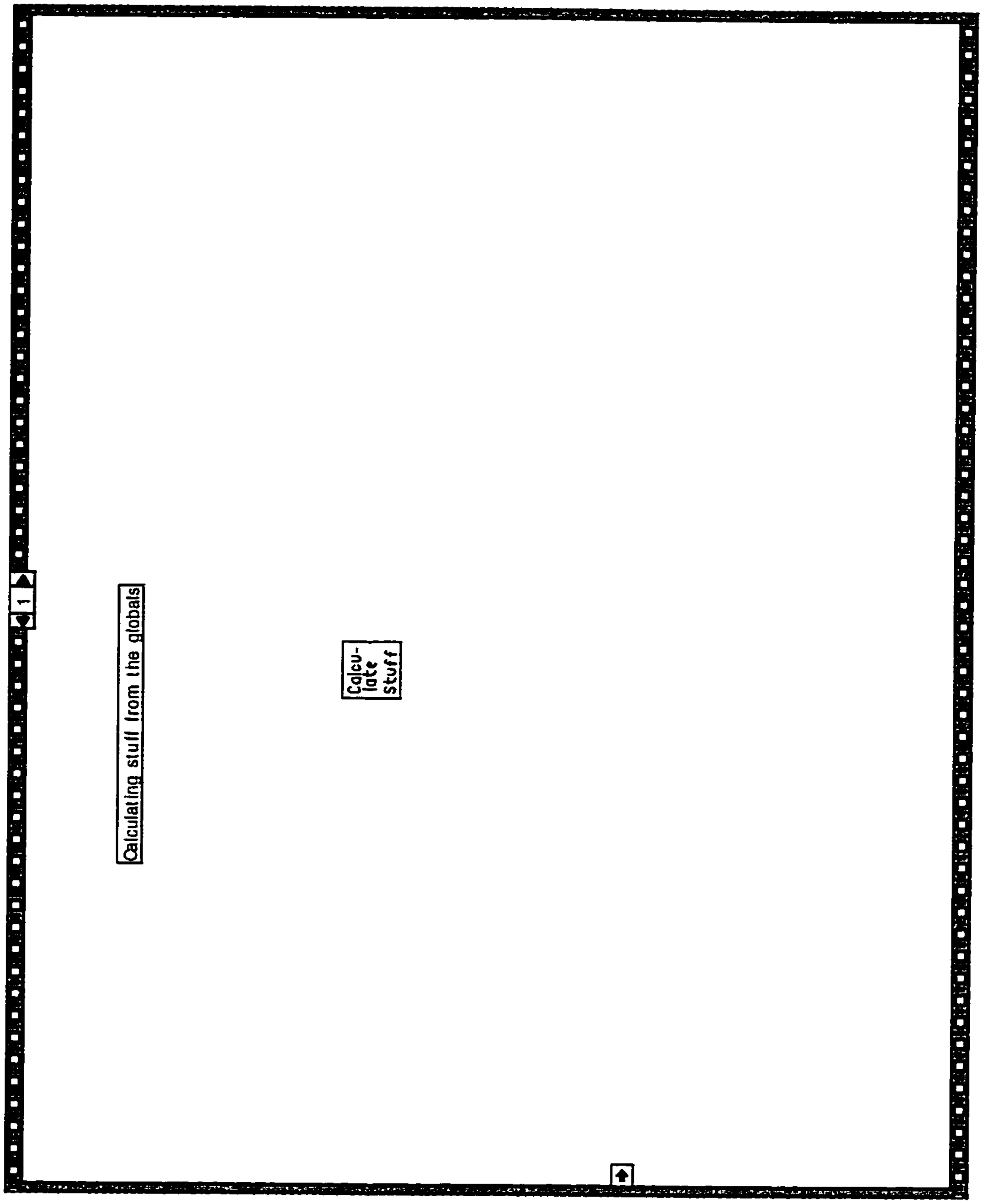
1
Calculating stuff from the globals
Calcu-
late
Stuff

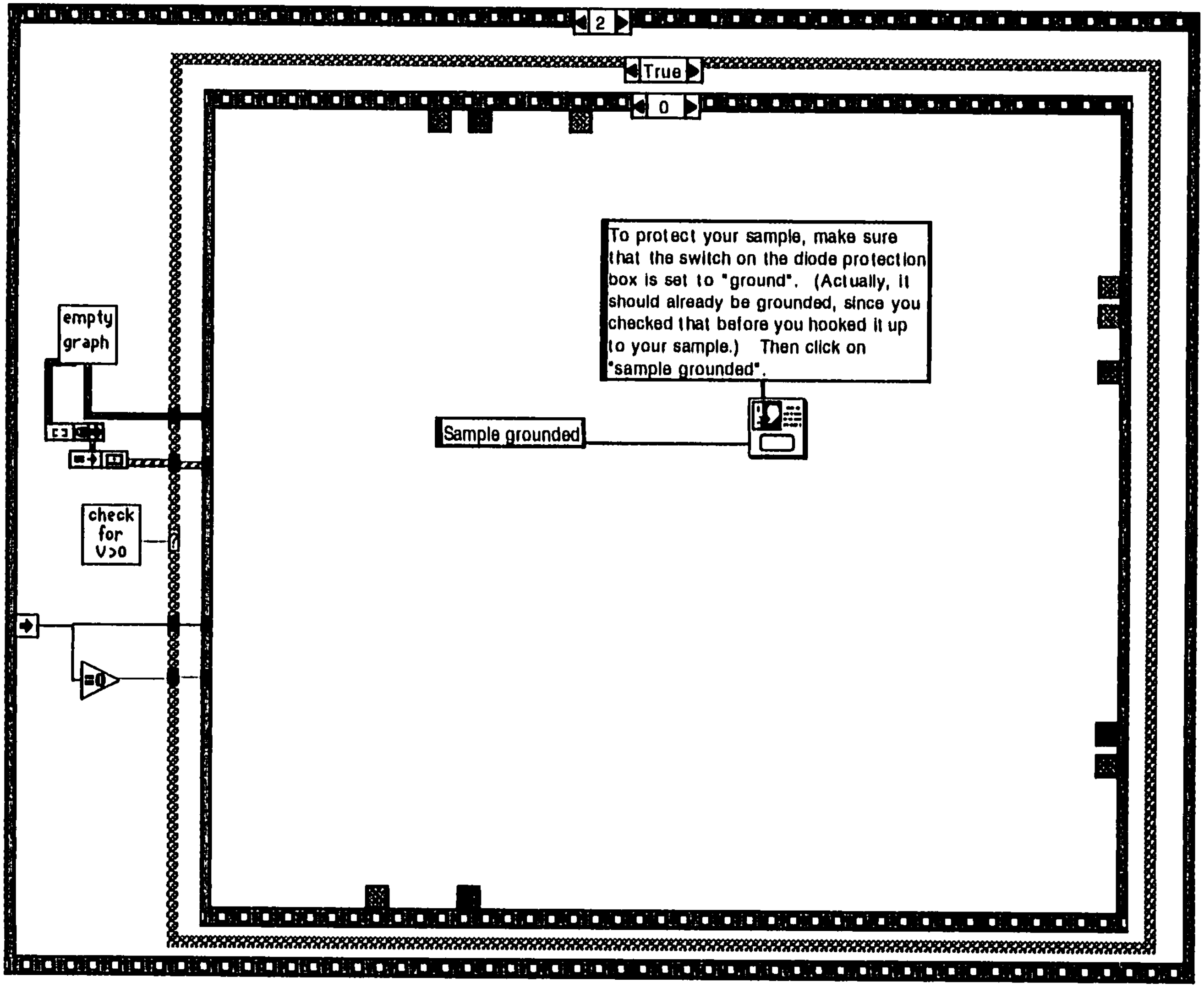

To protect your sample, make sure that the switch on the diode protection box is set to "ground". (Actually, it should already be grounded, since you checked that before you hooked it up to your sample.) Then click on "sample grounded".

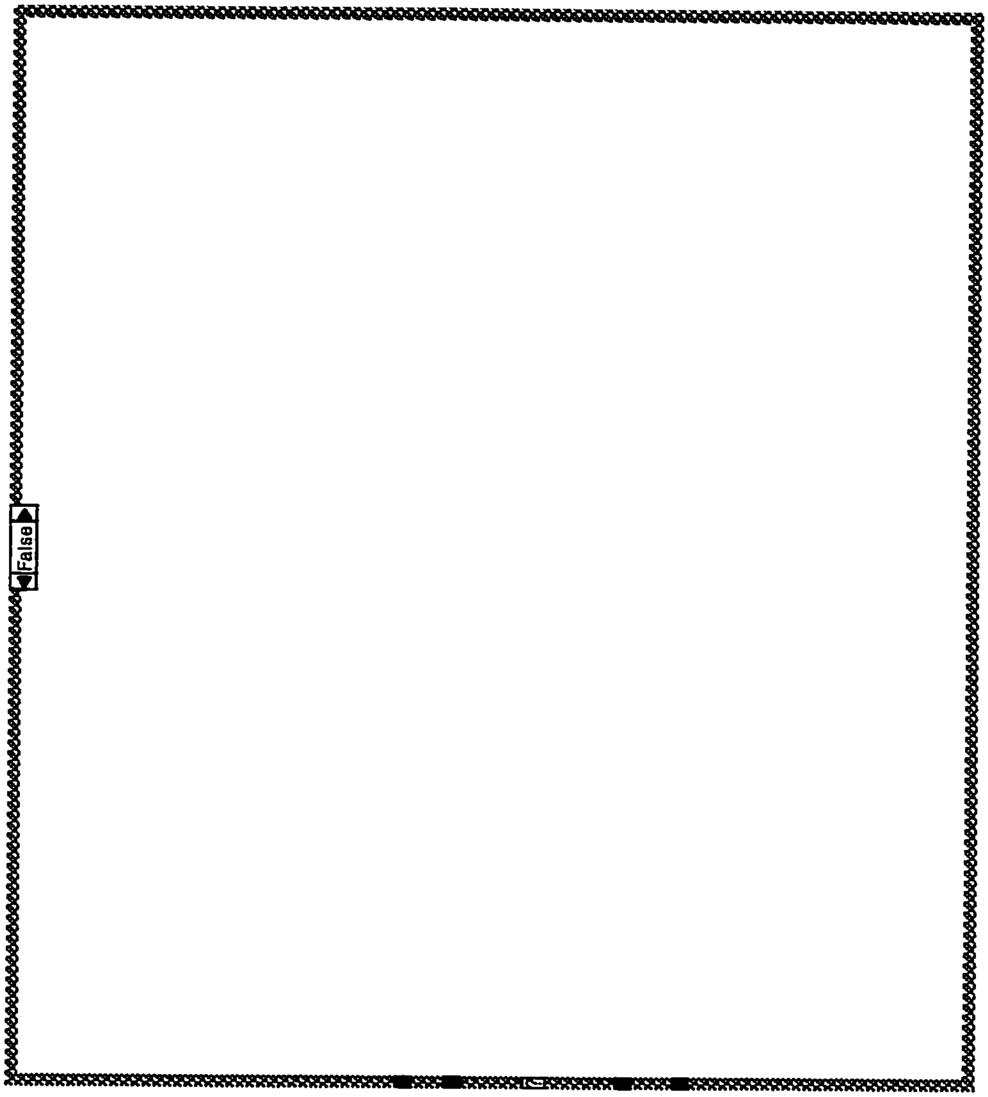
False

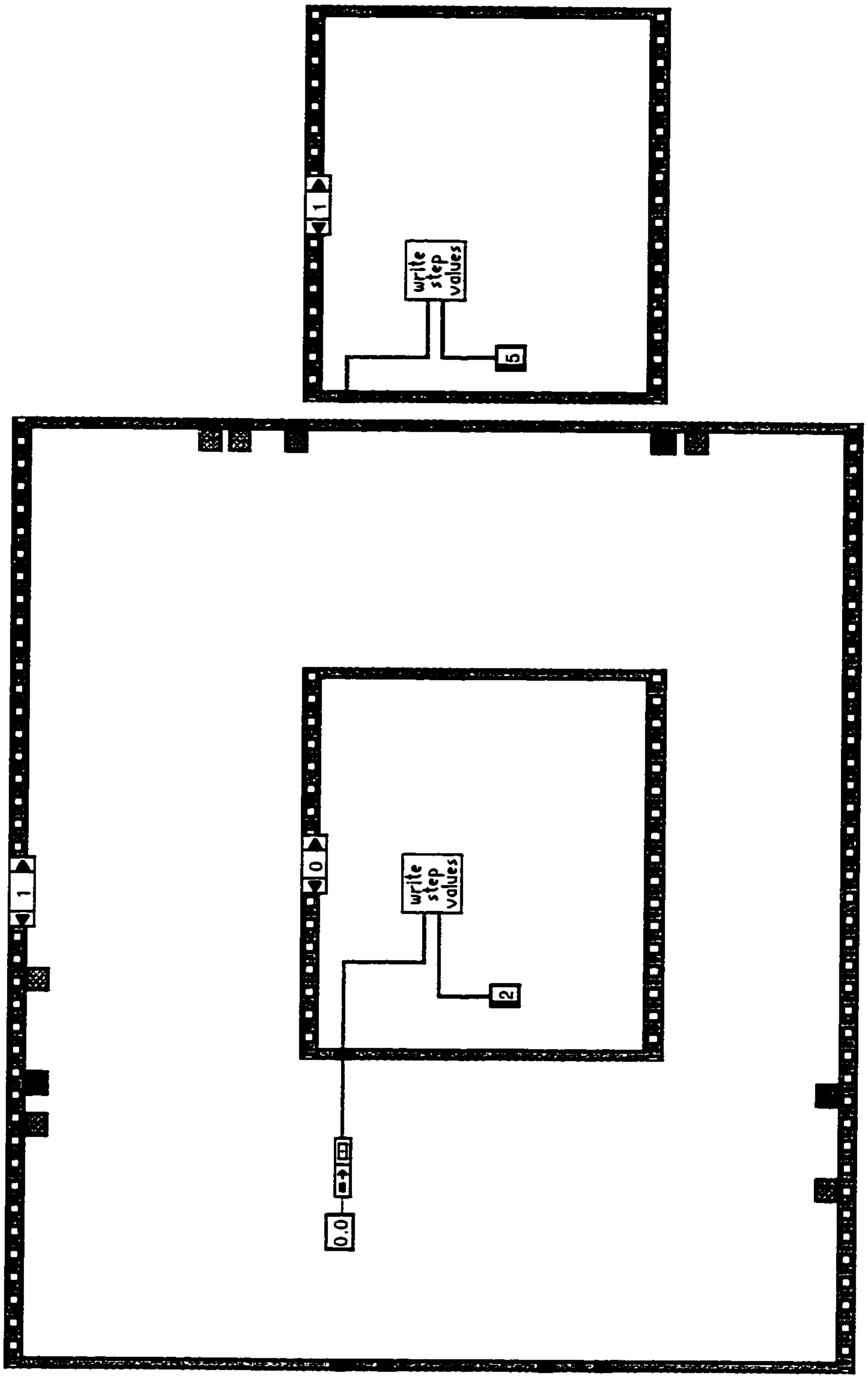
1
write step values
5
1
0
write step values
2
0.0

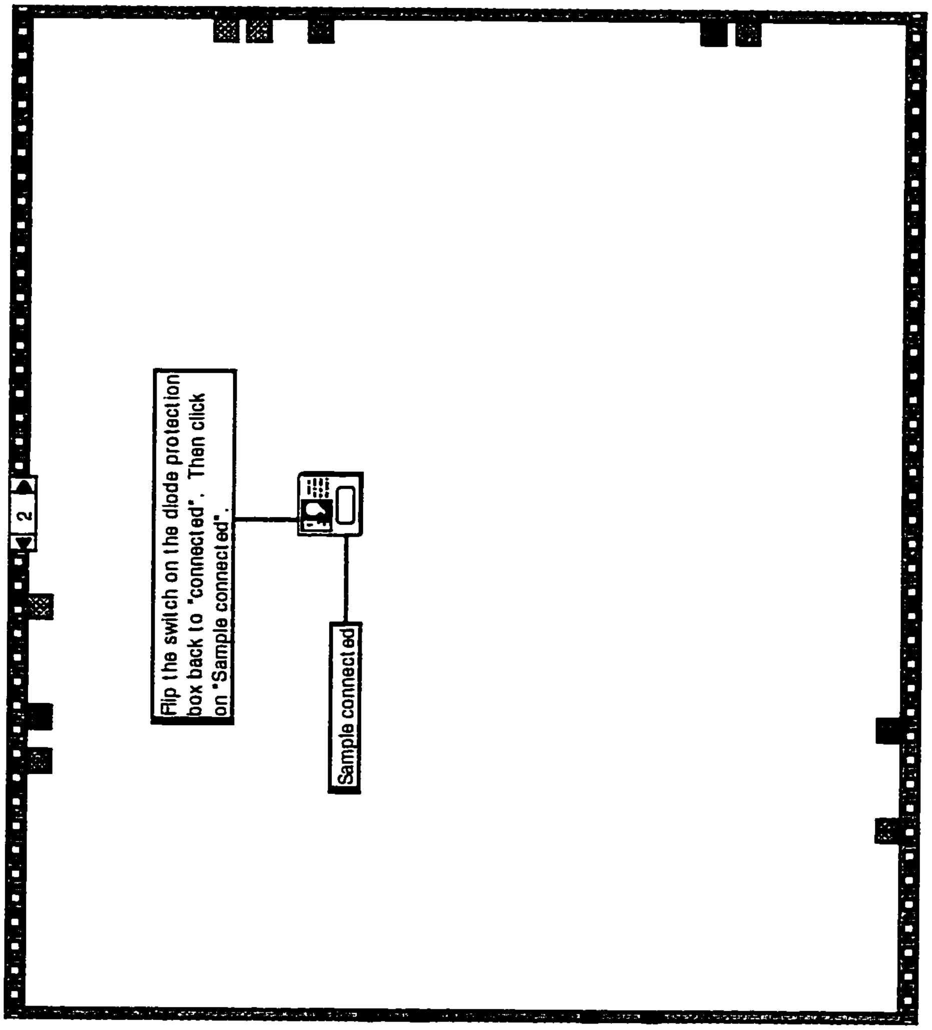

Flip the switch on the diode protection box back to "connected". Then click on "Sample connected".

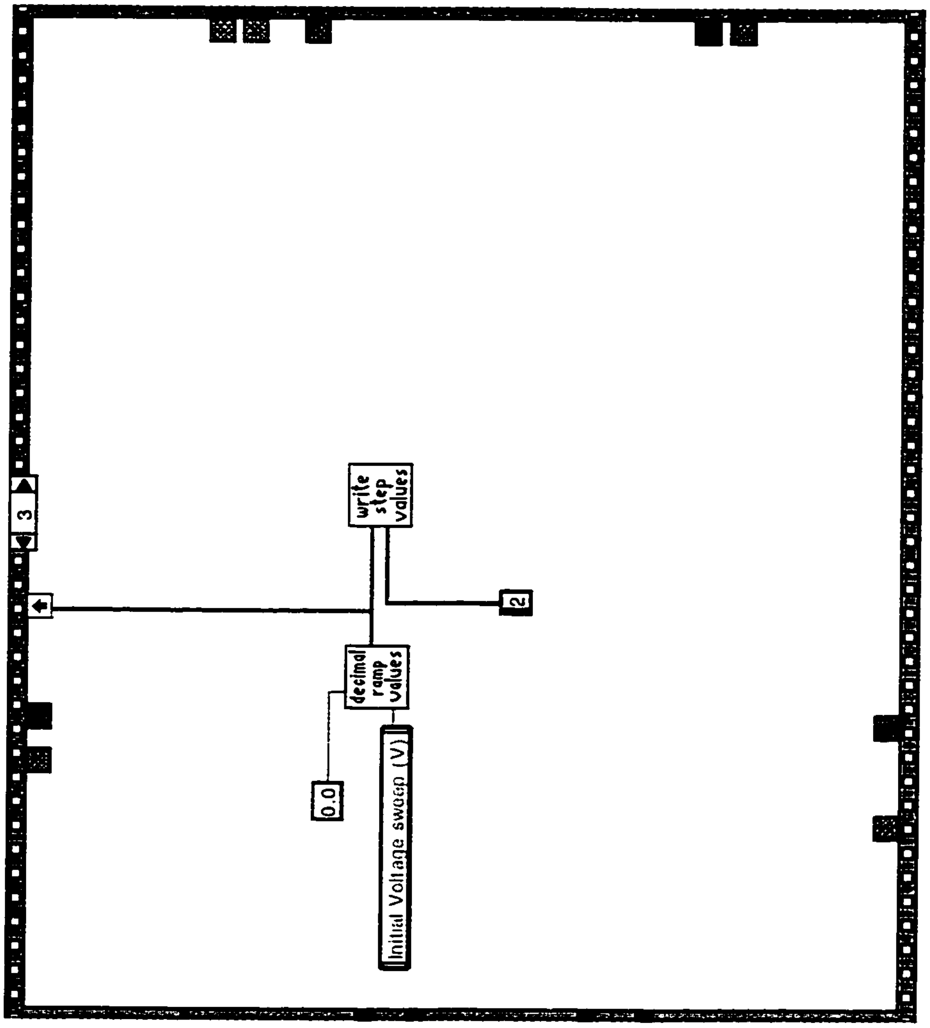
3
write step values
decimal ramp values
0.0
Initial Voltage sweep (V)
2

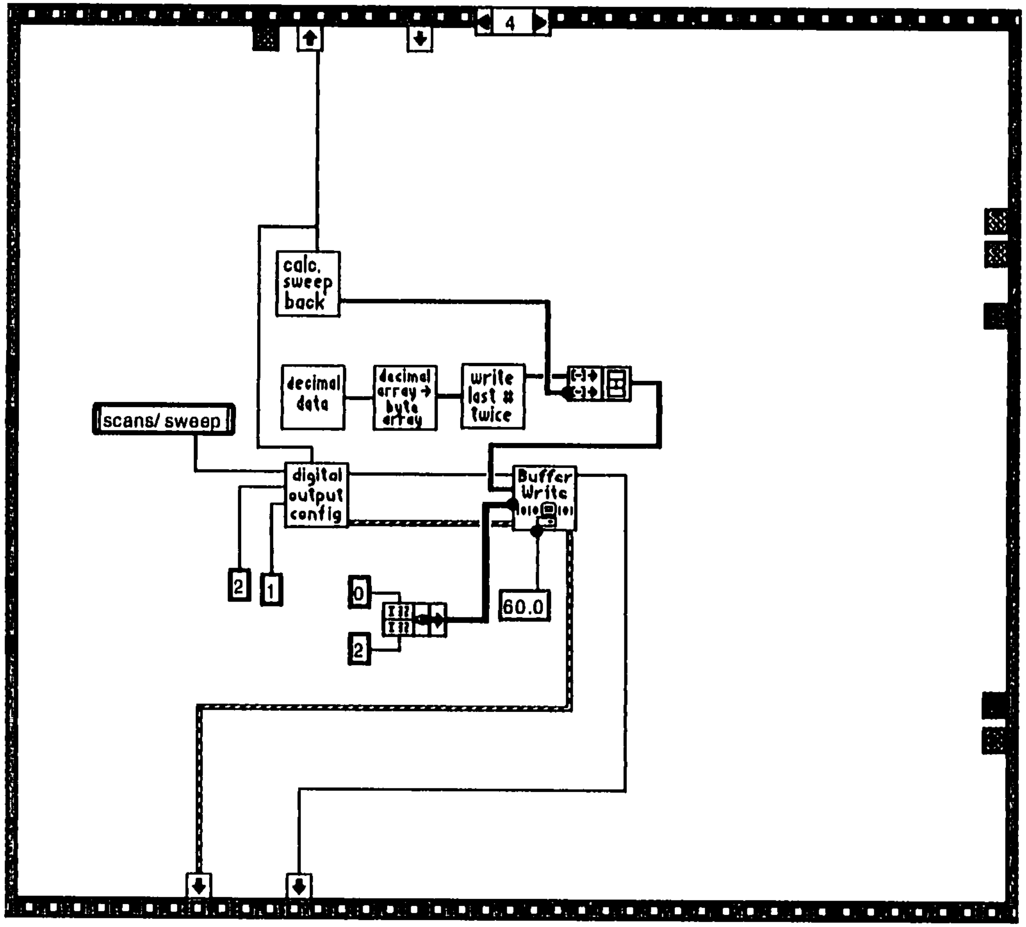
4
calc. sweep back
decimal data
decimal array → byte array
write last # twice
scans/ sweep
digital output config
Buffer Write
0
2
60.0
2
1

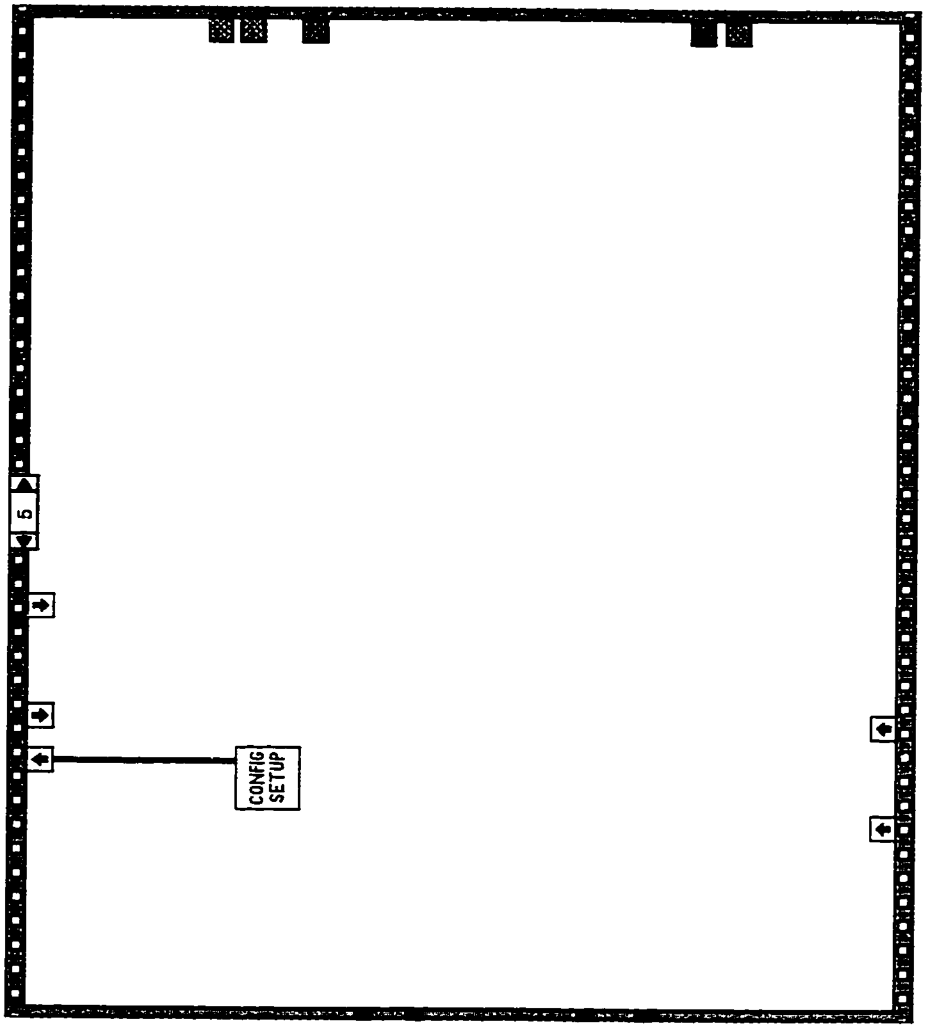
5
CONFIG SETUP

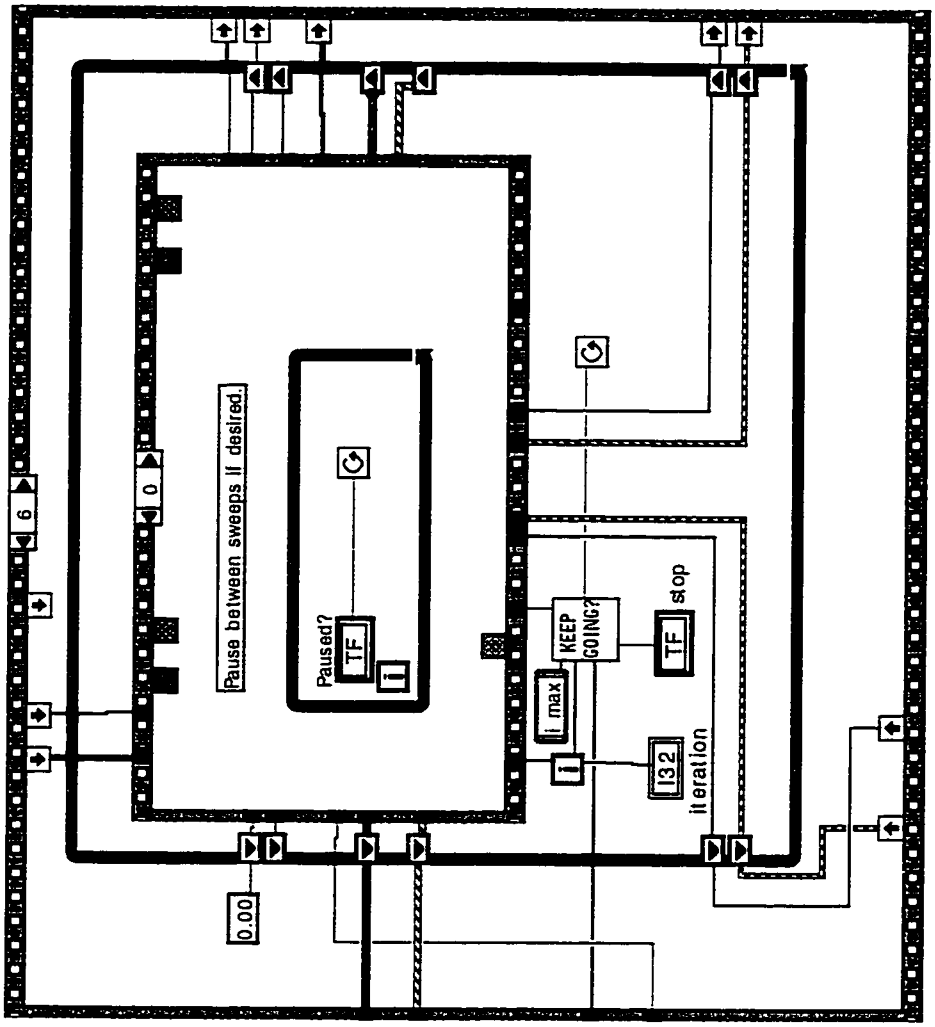
6
0
Pause between sweeps if desired.
Paused?
TF
i
KEEP GOING?
stop
TF
i max
i
I32
iteration
0.00

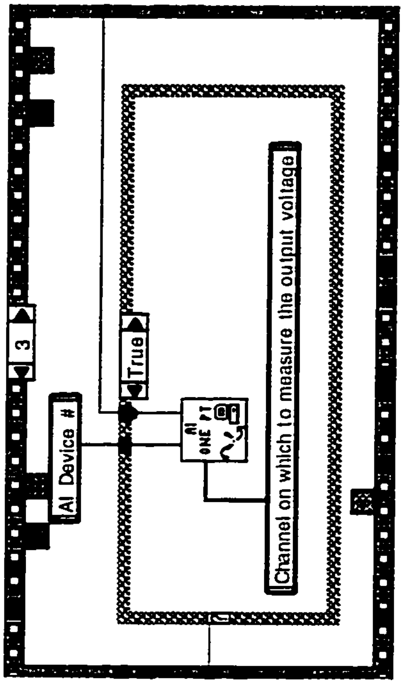
3
AI Device #
True
AI ONE PT
Channel on which to measure the output voltage

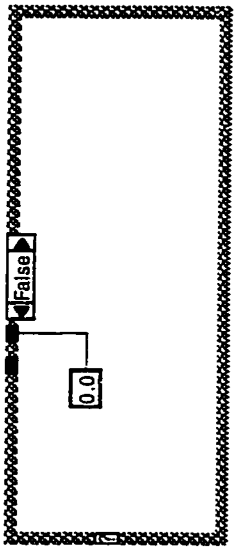
False
0.0

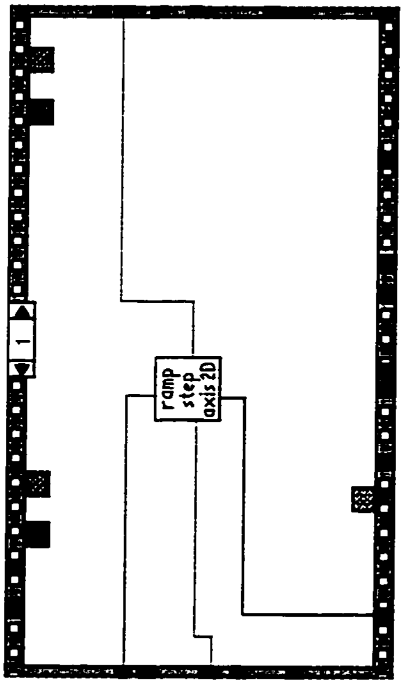
1
ramp step axis 2D

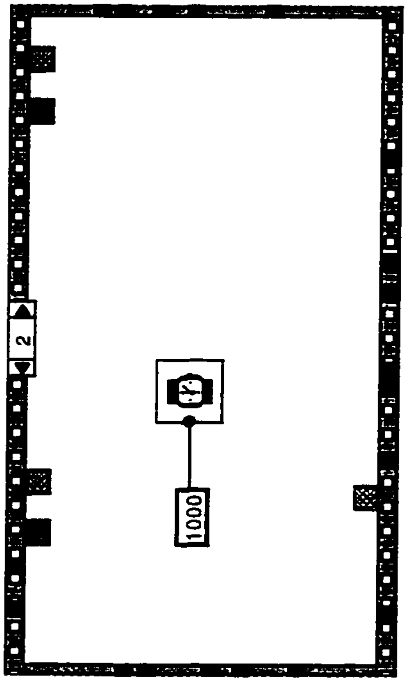
2
1000

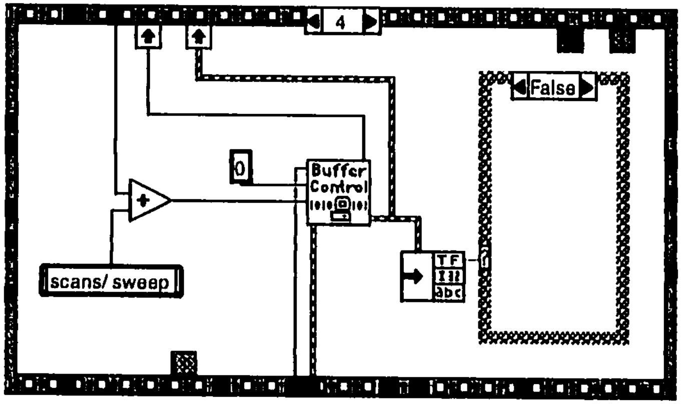
4
False
0
Buffer Control
TF
scans/ sweep

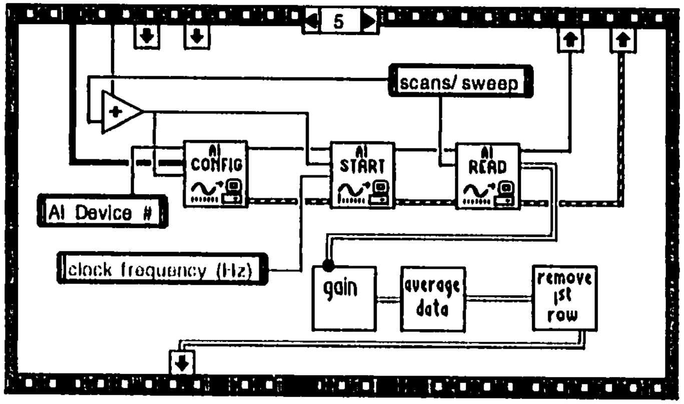
5
scans/ sweep
AI CONFIG
AI START
AI READ
AI Device #
clock frequency (Hz)
gain
average data
remove 1st row

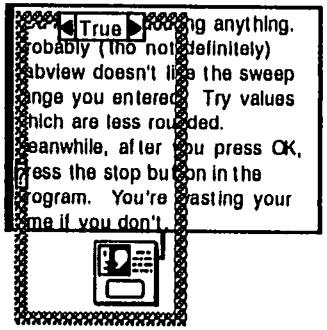
True
g anything.
obably (tho not definitely)
abview doesn't like the sweep
nge you entered. Try values
hich are less rounded.
eanwhile, after you press OK,
ess the stop button in the
ogram. You're wasting your
me if you don't.

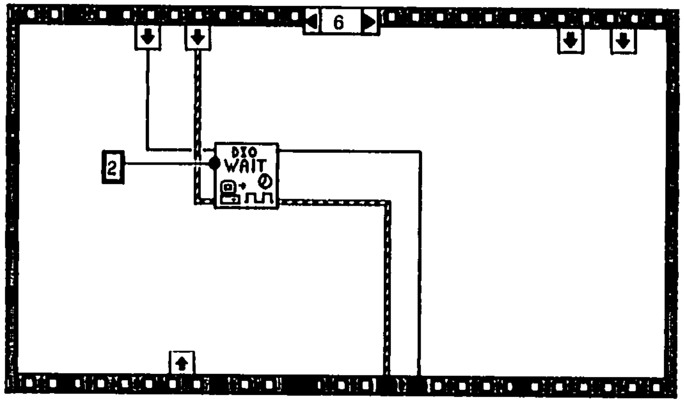
6
2
DIO WAIT

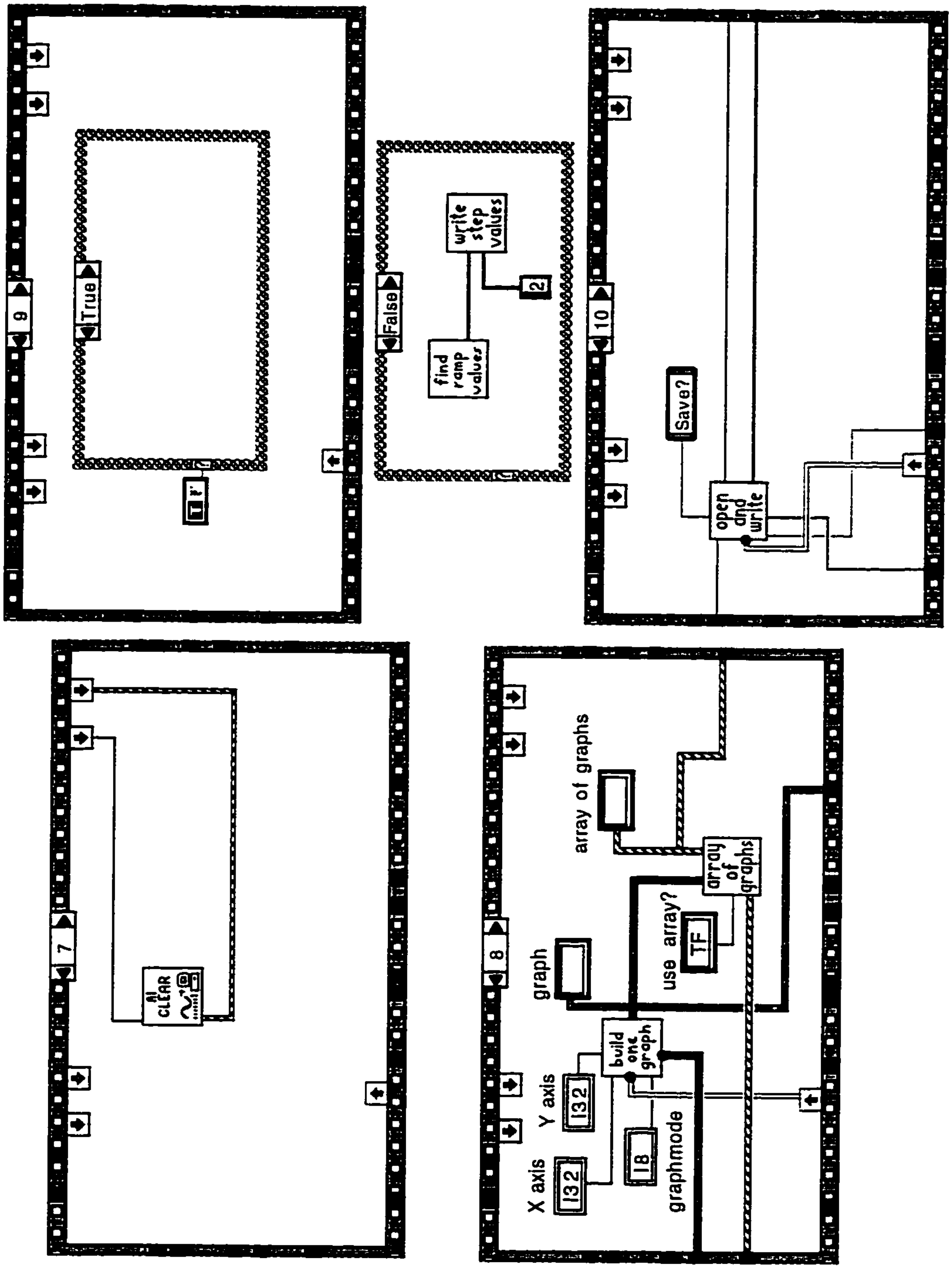
9
True
False
find ramp values
write step values
2
10
Save?
open and write
7
AI CLEAR
8
X axis
Y axis
I32
I32
I8
graphmode
build one graph
graph
use array?
TF
array of graphs
array of graphs

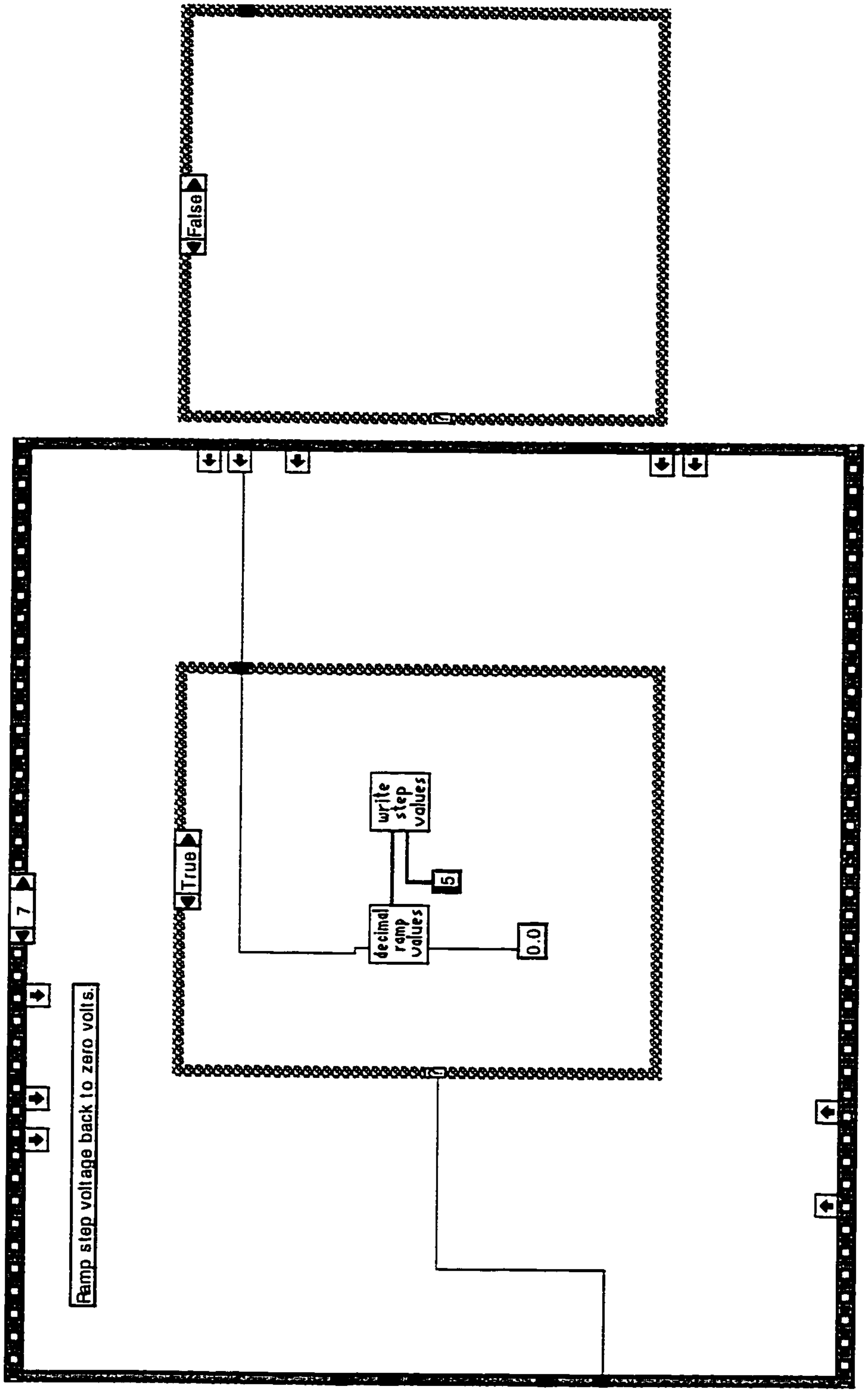
False
7
Ramp step voltage back to zero volts.
True
decimal ramp values
write step values
5
0.0

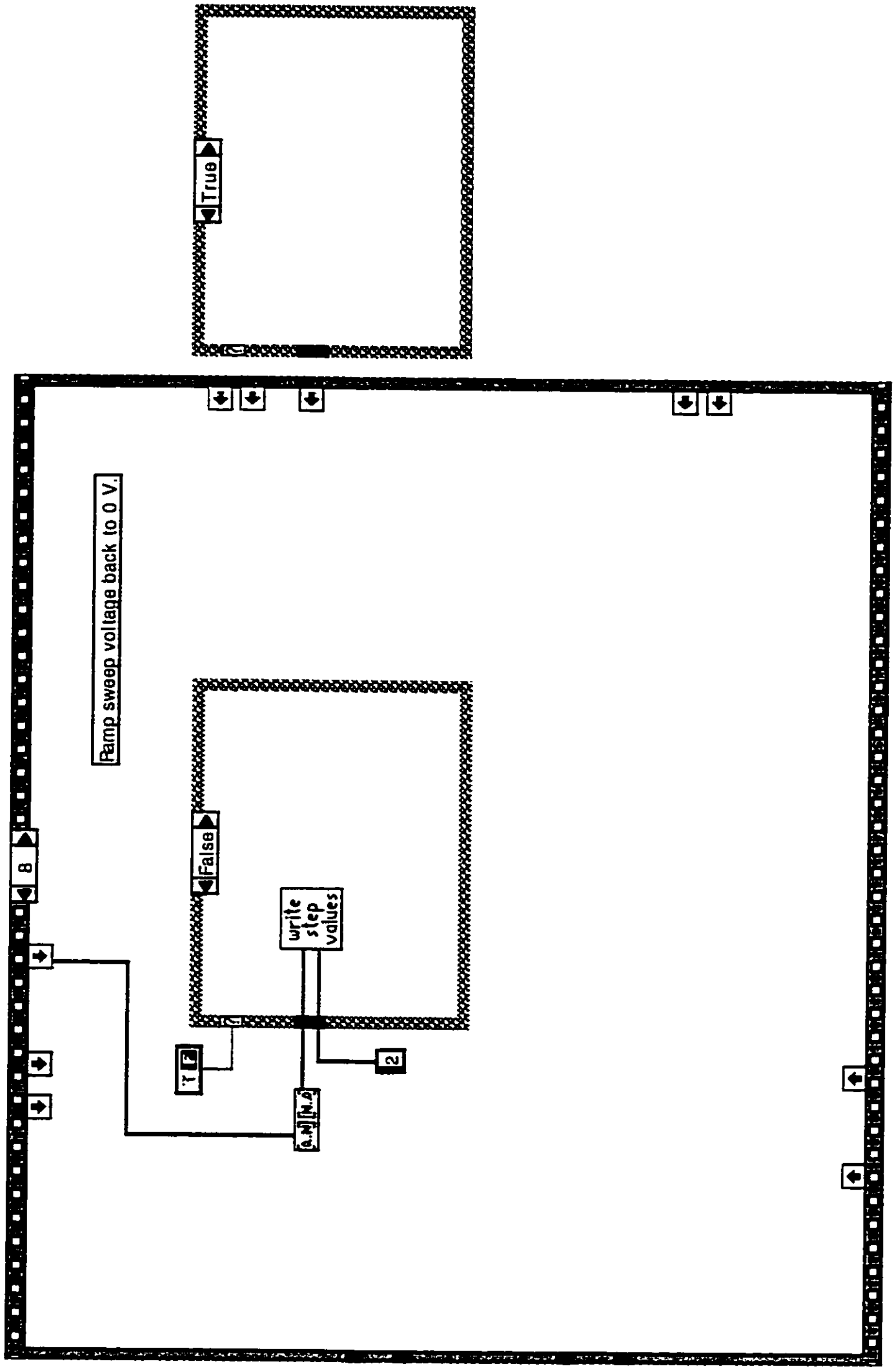
True
8
Ramp sweep voltage back to 0 V.
False
write step values
2

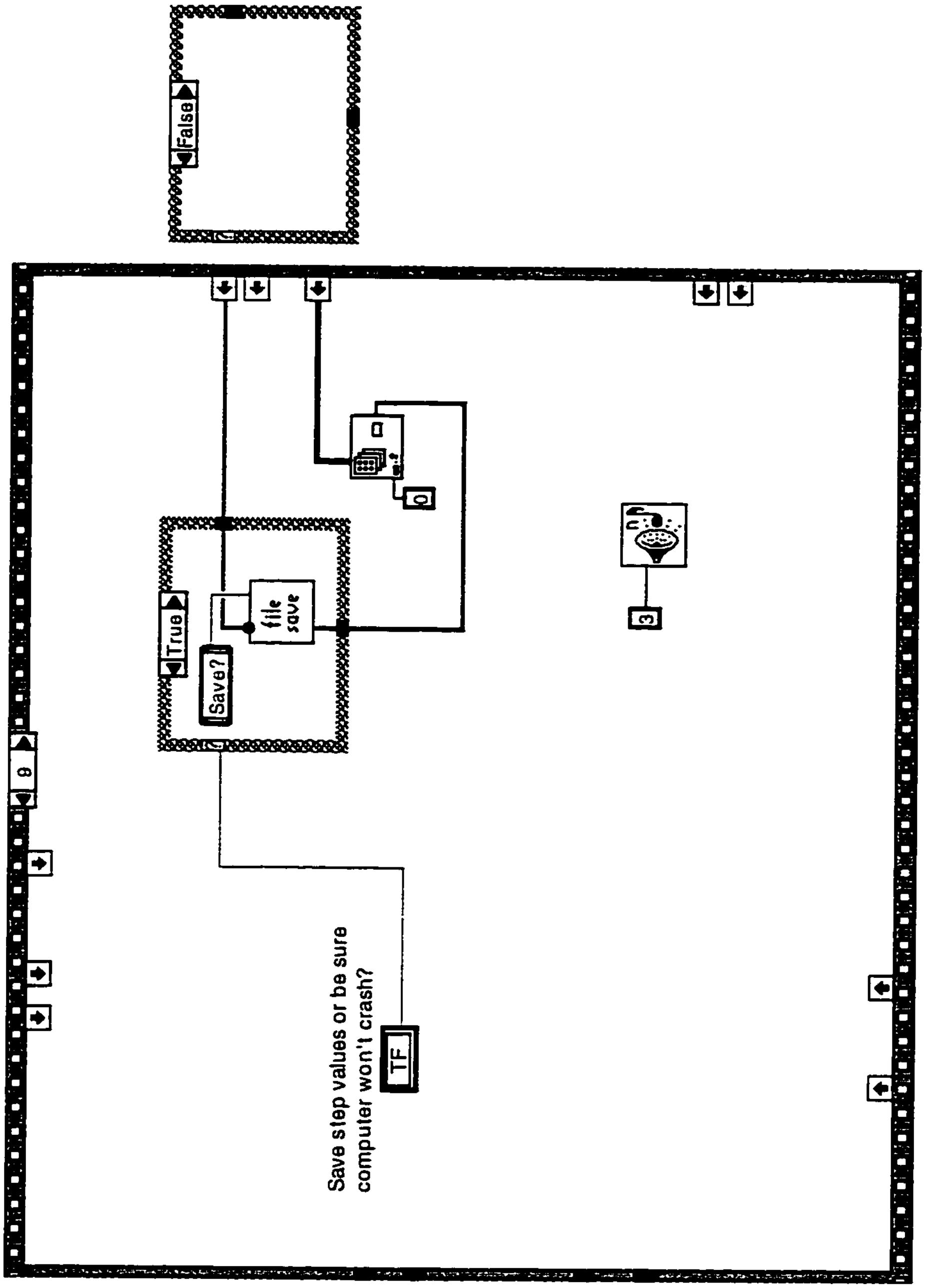
False
8
True
Save?
file save
0
3
Save step values or be sure computer won't crash?
TF

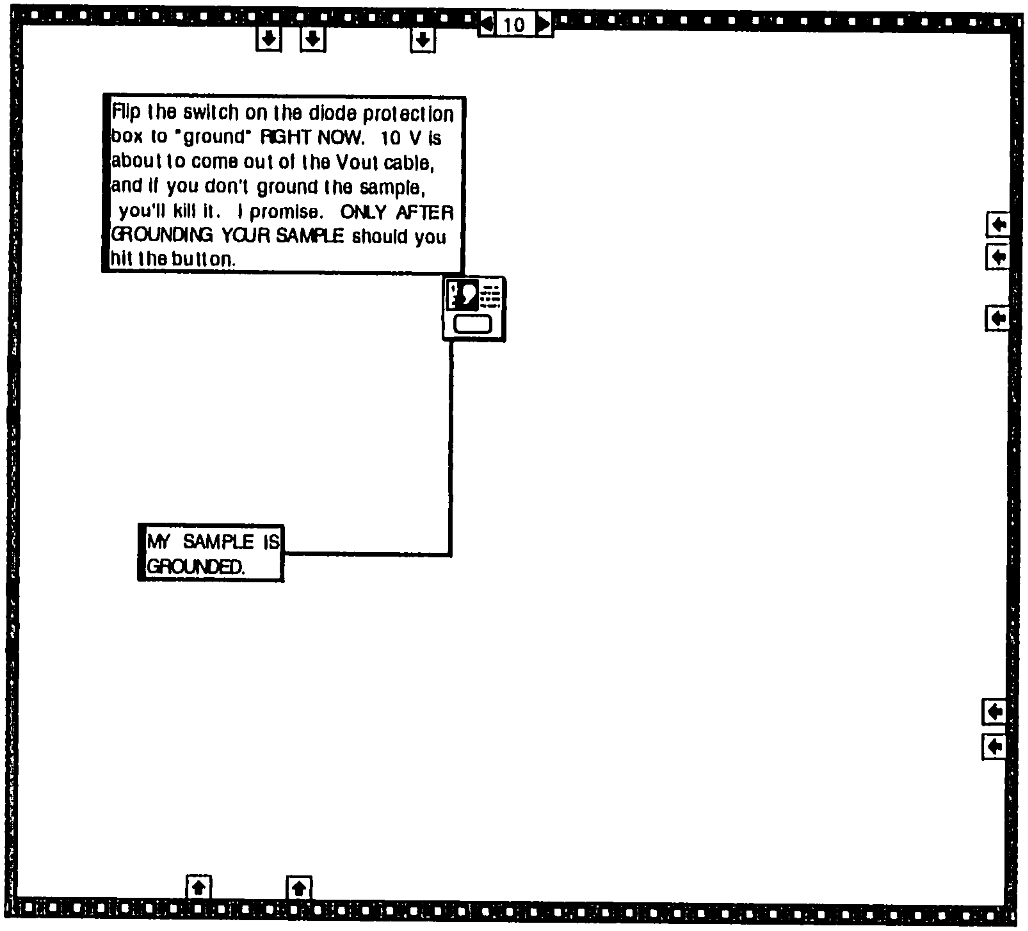

Flip the switch on the diode protection box to "ground" RIGHT NOW. 10 V is about to come out of the Vout cable, and if you don't ground the sample, you'll kill it. I promise. ONLY AFTER GROUNDING YOUR SAMPLE should you hit the button.

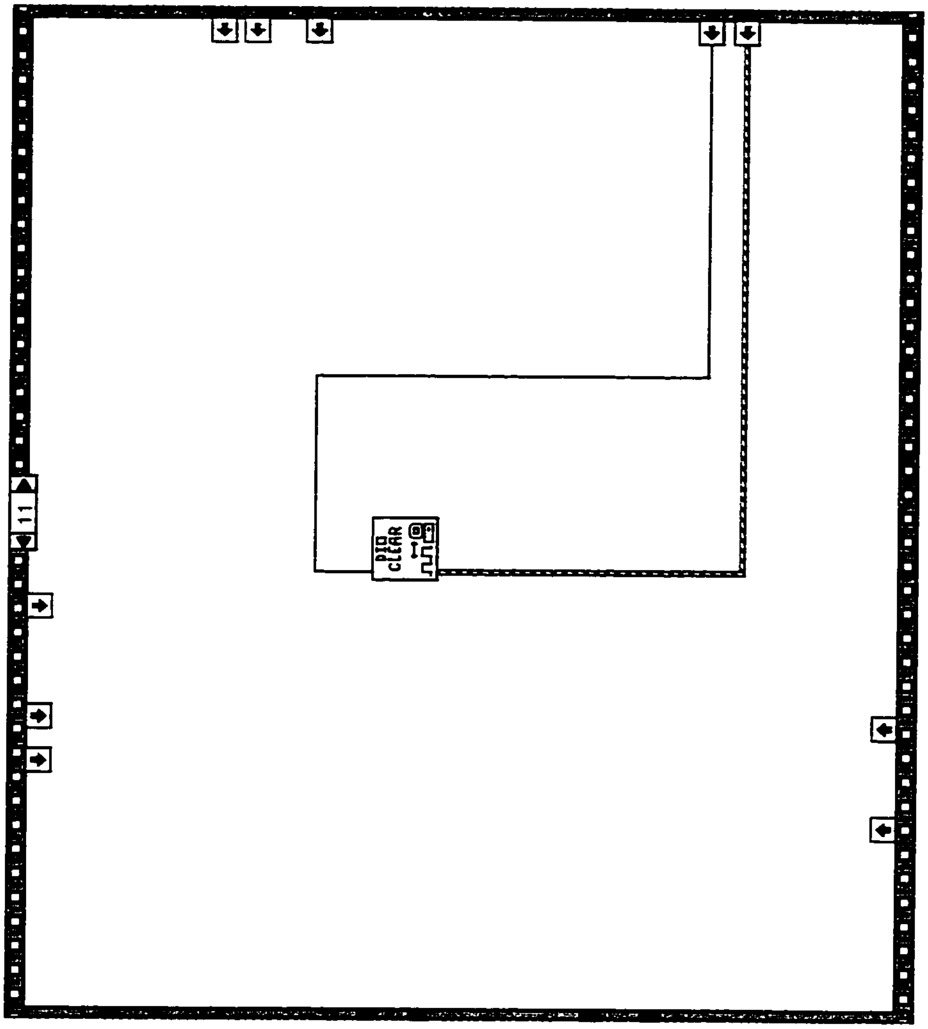
11
DIO
CLEAR

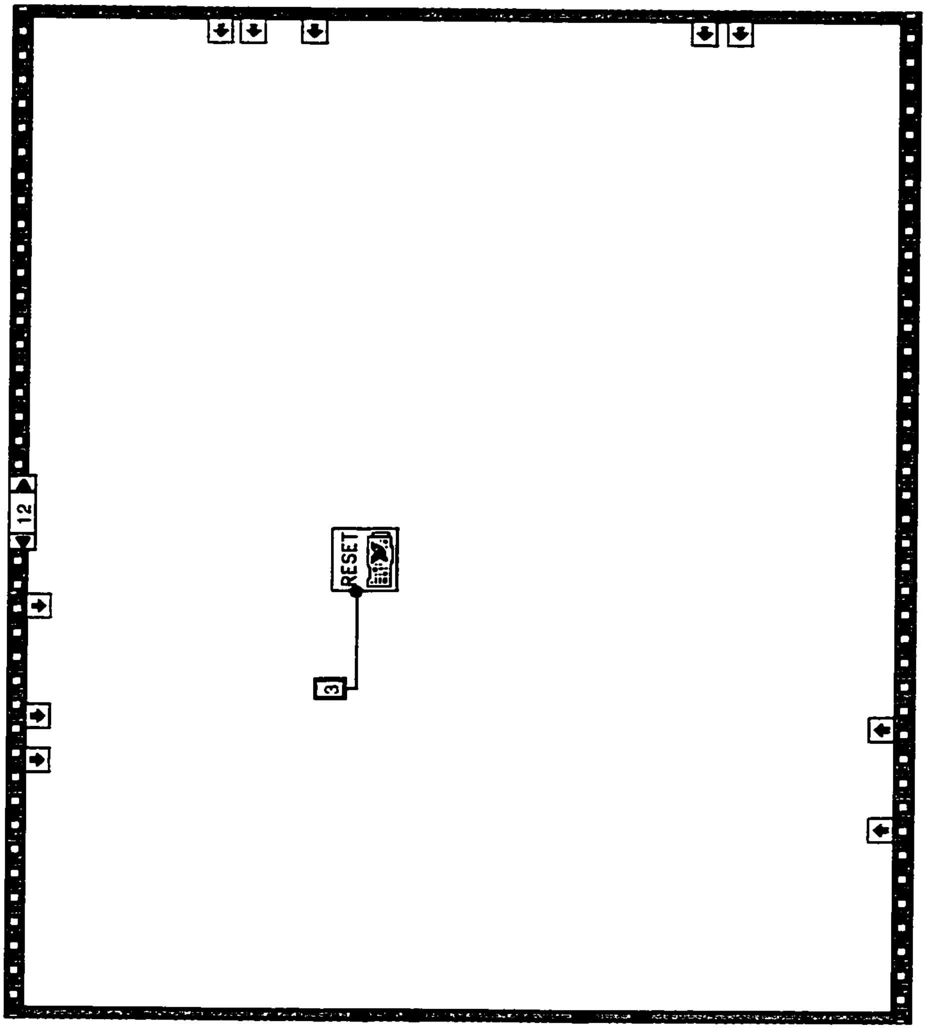
12
RESET
3

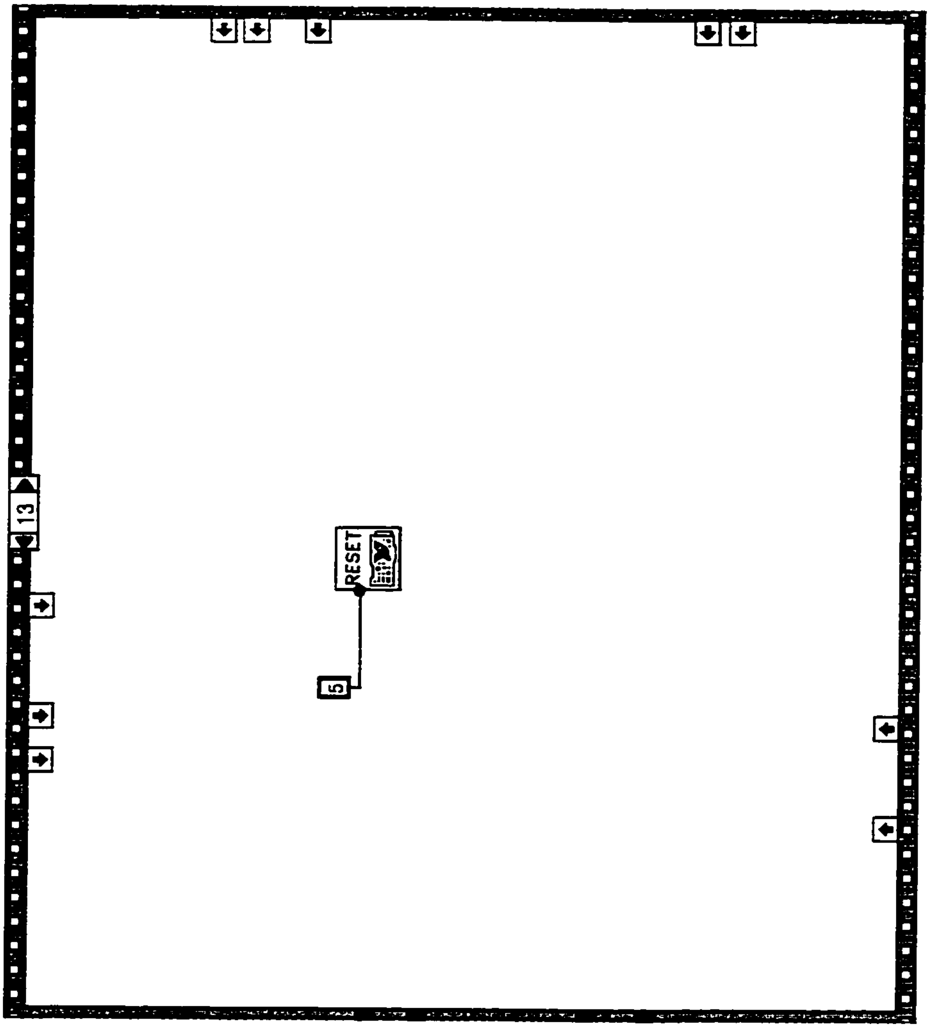
13
RESET
5

References

Adourian, A.S., C. Livermore, R.M. Westervelt, K.L. Campman, and A.C. Gossard (1996a). "Single-electron charging in parallel coupled quantum dots," *Superlattices and Microstructures* **20**, 411.

Adourian, A.S. (1996b). "Single electron transport in parallel coupled quantum dot nanostructures," Ph.D. thesis, Harvard University.

Altschuler, B.L., P.A. Lee, and R.A. Webb, eds. (1991). *Mesoscopic Phenomena in Solids* (North-Holland Elsevier Science Publishers B.V., Amsterdam).

Ashoori, R.C., H.L. Stormer, J.S. Weiner, L.N. Pfeiffer, S.J. Pearton, K.W. Baldwin, and K.W. West (1992). "Single-Electron Capacitance Spectroscopy of Discrete Quantum Levels," *Phys. Rev. Lett.* **68**, 3088.

Ashoori, R.C., H.L. Stormer, J.S. Weiner, L.N. Pfeiffer, K.W. Baldwin, and K.W. West (1993). "N-Electron Gorund State Energies of a Quantum Dot in a Magnetic Field," *Phys. Rev. Lett.* **71**, 613.

Averin, D.V., and K.K. Likharev (1991). "Single Electronics: A Correlated Transfer of Single Electrons and Cooper Pairs in Systems of Small Tunnel Junctions," in *Mesoscopic Phenomena in Solids*, eds. B.L. Altschuler, P.A. Lee, and R.A. Webb (Elsevier), p. 173-271.

Baskey, J.H. (1994). "Transport and capacitance measurements of electron multilayers in wide parabolic quantum wells," Ph.D. thesis, Harvard University.

Beenakker, C.W.J. and H. van Houten (1989). "Magnetotransport and nonadditivity of point-contact resistances in series," *Phys. Rev. B* **39**, 10445.

Beenakker, C.W. and H. van Houten (1991). "Quantum transport in semiconductor nanostructures," in Solid State Physics, vol. 44, ed. H. Ehrenreich and D. Turnbull (Academic Press, San Diego), 1.

Berry, M.J. (1994). "Mesoscopic transport and quantum chaos in ballistic quantum billiards," Ph.D. thesis, Harvard University.

Beton, P.H., B.R. Snell, P.C. Main, A. Neves, J.R. Owers-Bradley, L. Eaves, M. Henini, O.H. Hughes, S.P. Beaumont, and C.D.W. Wilkinson (1989). *J. Phys. Condens. Matter* **1**, 7505.

Blick, R.H., R.J. Haug, J. Weis, D. Pfannkuche, K. v. Klitzing, and K. Eberl (1996). "Single electron tunneling through a double quantum dot: The artificial molecule," *Phys. Rev. B* **53**, 7899.

Crouch, C.H. (1996a). "Single electron transport and charge quantization in coupled quantum dots," Ph.D. thesis, Harvard University.

Crouch, C.H., C. Livermore, F.R. Waugh, R.M. Westervelt, K.L. Campman, and A.C. Gossard (1996b). "Coulomb gap of coupled quantum dots with adjustable interdot tunneling," *Surface Science* **361/362**, 631.

Crouch, C.H., C. Livermore, R.M. Westervelt, K.L. Campman, and A.C. Gossard (1996c). "Coulomb oscillations in partially open quantum dots," *Superlattices and Microstructures* **20**, 377.

Crouch, C.H., C. Livermore, R.M. Westervelt, K.L. Campman, and A.C. Gossard (1997). "Evolution of the Coulomb gap in tunnel-coupled quantum dots," *Appl. Phys. Lett.* **71**, 817.

Dingle, R., H.L. Stormer, A.C. Gossard, and W. Wiegman (1978). *Appl. Phys. Lett.* **7**, 665.

Dixon, D., L.P. Kouwenhouven, P.L. McEuen, Y. Nagamune, J. Motohisa, and H. Sakaki (1996). "Linear and nonlinear transport through coupled quantum dots," *Surf. Sci.* **361/362**, 636.

Dresselhaus, P.D., L. Ji, J.E. Siyuan Han Lukens, and K.K. Likharev (1994). "Measurement of single electron lifetimes in a multijunction trap," *Phys. Rev. Lett.* **72**, 3226.

Eriksson, M.A. (1997). "Cryogenic Scanning Probe Microscopy for Semiconductor Nanostructures," Ph.D. thesis, Harvard University.

Falci, G., G. Schon, G.T. Zimanzi (1995). *Phys. Rev. Lett.* **74**, 3257.

Foxman, E.B., P.L. McEuen, U. Meirav, N.S. Wingreen, Y. Meir, P.A. Belk, N.R. Belk, and M.A. Kastner (1993). "Effects of quantum levels on transport through a Coulomb island," *Phys. Rev. B* **47**, 10020.

Furusaki, A. and K.A. Matveev (1995). "Coulomb blockade oscillations of conductance in the regime of strong tunneling," *Phys. Rev. Lett.* **75**, 709.

Glazman, L.I. and K.A. Matveev (1990). *Sov. Phys. JETP* **71**, 1031.

Golden, John M. and B.I. Halperin (1996a). "Relation between barrier conductance and Coulomb blockade peak splitting for tunnel-coupled quantum dots," *Phys. Rev. B* **53**, 3893.

Golden, John M. and B.I. Halperin (1996b). *Phys. Rev. B* **54**, 16 757.

Golden, John M. (1997). "Coulomb Blockade of Tunnel-Coupled Quantum Dots," Ph.D. thesis, Harvard University.

Grabert, H. and M.H. Devoret, eds. (1992). *Single Charge Tunneling*, NATO ASI Series B, Vol. 294 (Plenum: New York).

Halperin, B.I. (1982). *Phys. Rev. Lett.* **60**, 1542.

Hergenrother, J.M. (1995). "Parity effects and charge transport in the single-electron transistor," Ph.D. thesis, Harvard University.

Herman, M.A. and H. Sitter, 1989. *Molecular Beam Epitaxy: Fundamentals and Current Status* (Springer-Verlag, Berlin).

Hofmann, F., T. Heinzel, D.A. Wharam, J.P. Kotthaus, G. Bohm, W. Klein, G. Trankle, and G. Weimann (1995). "Single electron switching in a parallel quantum dot," *Phys. Rev. B* **51**, 13872.

Hopkins, P.F. (1994). Ph.D. thesis, Harvard University.

Kastner, M.A. (1992). "The single-electron transistor," *Rev. Mod. Phys.* **64**, 849.

Kastner, M.A. (1993). "Artificial atoms," *Physics Today* **46(1)**, 24.

Katine, J.A. (1996). "Electronic quantum interference in ballistic microstructures," Ph.D. thesis, Harvard University.

Kemerink, M. and L.W. Molenkamp (1994). "Stochastic Coulomb blockade in a double quantum dot," *Appl. Phys. Lett.* **65**, 1012.

Klein, O., C. de C. Chamon, D. Tang, D.M. Abusch-Magder, U. Meirav, X.-G. Wen, M.A. Kastner, and S.J. Wind (1995). "Exchange effects in an artificial atom at high magnetic fields," *Phys. Rev. Lett.* **74**, 785.

Klein, O., D. Goldhaber-Gordon, C. de C. Chamon, and M.A. Kastner (1996). "Magnetic-field dependence of the level spacing of a small electron droplet," *Phys. Rev. B* **53**, R4221.

Korotkov, A.N., R.H. Chen, and K.K. Likharev (1995). "Possible performance of capacitively coupled single-electron transistors in digital circuits," *J. of Appl. Phys.* **78**, 2520.

Kulkarni, A.K. and J.T. Lukowski (1986). "Effect of annealing process parameters on the properties of AuGe ohmic contacts to GaAs," *J. Appl. Phys.* **59**, 2901.

Lent, C.S., P.D. Tougaw, and W. Porod (1993). "Bistable saturation in coupled quantum dots for quantum cellular automata," *Appl. Phys. Lett.* **62**, 714.

Livermore, C., C.H. Crouch, R.M. Westervelt, K.L. Campman, and A.C. Gossard (1996). "The Coulomb Blockade in Coupled Quantum Dots," *Science* **274**, 1332.

Livermore, C., C.H. Crouch, R.M. Westervelt, K.L. Campman, and A.C. Gossard (1996). "Conductance peak splitting in charge polarized coupled quantum dots," *Superlattices and Microstructures* **20**, 633.

Loss, D. and D.P. DiVincenzo (1998). "Quantum computation with quantum dots," *Phys. Rev. A* **57**, 120.

Lounasmaa, O.V. (1974). *Experimental Principles and Methods Below 1 K* (Academic Press, New York).

Mar, D.J. (1994). Ph.D. thesis, Harvard University.

Matveev, K.A. (1991). *Sov. Phys. JETP* **72**, 892 (1991).

Matveev, K.A. (1995). *Phys. Rev. B* **51**, 1743.

Matveev, K.A., L.I. Glazman, and H.U. Baranger (1996a). "Tunneling spectroscopy of quantum charge fluctuations in the Coulomb blockade," *Phys. Rev. B* **53**, 1034.

Matveev, K.A., L.I. Glazman, and H.U. Baranger (1996b). *Phys. Rev. B* **54**, 5637.

McEuen, P.L., E.B. Foxman, U. Meirav, M.A. Kastner, Yigal Meir, Ned S. Wingreen, and S.J. Wind (1991). "Transport Spectroscopy of a Coulomb Island in the Quantum Hall Regime," *Phys. Rev. Lett.* **66**, 1926.

McEuen, P.L., E.B. Foxman, J.M. Kinaret, U. Meirav, M.A. Kastner, N.S. Wingreen, and S.J. Wind (1992). *Phys. Rev. B* **45**, 11419.

McEuen, P.L., N.S. Wingreen, E.B. Foxman, J. Kinaret, U. Meirav, M.A. Kastner, Y. Meir, and S.J. Wind (1993). *Physica B* **70**, 70.

Molenkamp, L.W. and Karsten Flensberg (1995). "Scaling of the Coulomb Blockade," *Physica B* **218**, 269.

Pothier, H., P. Lafarge, P.F. Orfila, C. Urbina, D. Esteve, and M.H. Devoret (1991). "Single electron pump fabricated with ultrasmall normal tunnel junctions," *Physica B* **169**, 573.

Rimberg, A.J. (1992). Ph.D. thesis, Harvard University.

Ruzin, I.M., V. Chandrasekhar, E.I. Levin, and L.I. Glazman (1992). "Stochastic Coulomb blockade in a double-dot system," *Phys. Rev. B* **45**, 13469.

Schuster, R., E. Buks, M. Heiblum, D. Mahalu, V. Umansky, and H. Shtrikman (1997). "Phase measurement in a quantum dot via a double-slit interference measurement," *Nature* **385**, 417.

Stafford, C.A. and S. Das Sarma (1994). "Collective Coulomb Blockade in an Array of Quantum Dots: A Mott-Hubbard Approach," *Phys. Rev. Lett.* **72**, 3590.

Stewart, D.R., D. Sprinzak, C.M. Marcus, C.I. Duruoz, and J.S. Harris, Jr. (1997). "Correlations between ground and excited states spectra of a quantum dot," *Science* **278**, 1784.

Tarucha, S., D.G. Austing, T. Honda, R.J. van der Hage, and L.P. Kouwenhouven (1996). "Shell Filling and Spin Effects in a Few Electron Quantum Dot," *Phys. Rev. Lett.* **77**, 3613.

Thornton, T.J., M. Pepper, H. Ahmed, D. Andrews, and G.J. Davies (1986). *Phys. Rev. Lett.* **56**, 1198.

Tighe, T.S. (1993). Ph.D. thesis, Harvard University.

Tinkham, M. (1996). *Introduction to Superconductivity*, 2nd. ed. (New York: McGraw-Hill).

Tucker, J.R. (1992). "Complementary digital logic based on the 'Coulomb blockade'," *J. of Appl. Phys.* **72**, 4399.

Van der Vaart, N.C., M.P. de Ruyter van Steveninck, L.P. Kouwenhoven, A.T. Johnson, Y.V. Nazarov, C.J.P.M. Harmans, and C.T. Foxon (1994). "Time-Resolved Tunneling of Single Electrons between Landau Levels in a Quantum Dot," *Phys. Rev. Lett.* **73**, 320.

Van der Vaart, N.C. *et al.* (1995). *Phys. Rev. Lett.* **74**, 4702.

Van der Vaart, N.C. (1995). Ph.D. thesis, Delft Technical University.

Van Houten, H., C.W.J. Beenakker, and A.A.M. Staring (1992). In *Single Charge Tunneling*, edited by H. Grabert and M.H. Devoret; NATO ASI Series B, Vol. 294 (Plenum: New York).

Waugh, F.R. (1994). "Novel architectures and devices for computing," Ph.D. thesis, Harvard University.

Waugh, F.R., M.J. Berry, D.J. Mar, R.M. Westervelt, K.L. Campman, and A.C. Gossard (1995). "Single-Electron Charging in Double and Triple Quantum Dots with Tunable Coupling," *Phys. Rev. Lett.* **75**, 705.

Waugh, F.R., M.J. Berry, C.H. Crouch, C. Livermore, D.J. Mar, R.M. Westervelt, K.L. Campman, and A.C. Gossard (1996). "Measuring interactions between tunnel-coupled quantum dots," *Phys. Rev. B* **53**, 1413.

Weis, J., R.J. Haug, K. v. Klitzing, and K. Ploog (1993). "Competing Channels in Single-Electron Tunneling through a Quantum Dot," *Phys. Rev. Lett.* **71**, 4019.

Wharam, D.A., M. Pepper, H. Ahmed, J.E.F. Frost, D.G. Hasko, D.C. Peacock, D.A. Ritchie, and G.A.C. Jones (1988). *J. Phys. C* **21**, L887.

Yacoby, A., M. Heiblum, D. Mahalu, and Hadas Shtrikman (1995). "Coherence and Phase Sensitive Measurements in a Quantum Dot," *Phys. Rev. Lett.* **74**, 4047.

Yang, Scott (1995). Ph.D. thesis, Harvard University.

Yeyati, A. Levy and M. Buttiker (1995). "Aharonov-Bohm oscillations in a mesoscopic ring with a quantum dot," *Phys. Rev. B* **52**, R14360.

Zheng, H.Z., H.P. Wei, D.C. Tsui, and G. Weimann, *Phys. Rev. B* **34**, 5635 (1986).

Zhitenev, N.B., R.C. Ashoori, L.N. Pfeiffer, and K.W. West (1997). "Periodic and Aperiodic Bunching in the Addition Spectra of Quantum Dots," *Phys. Rev. Lett.* **79**, 2308.

IMAGE EVALUATION TEST TARGET (QA-3)

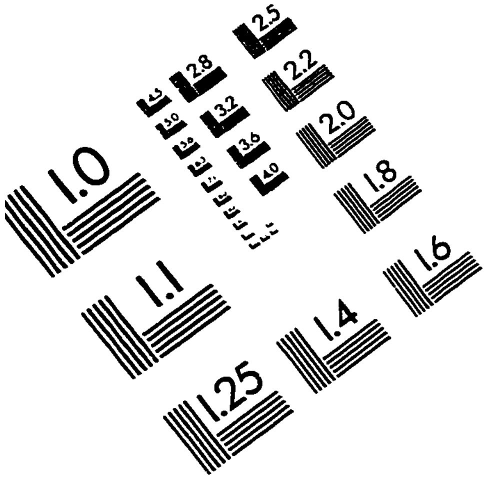

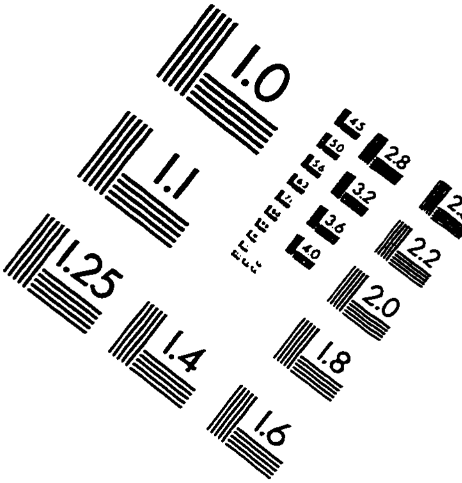

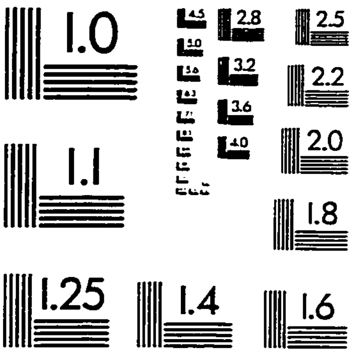

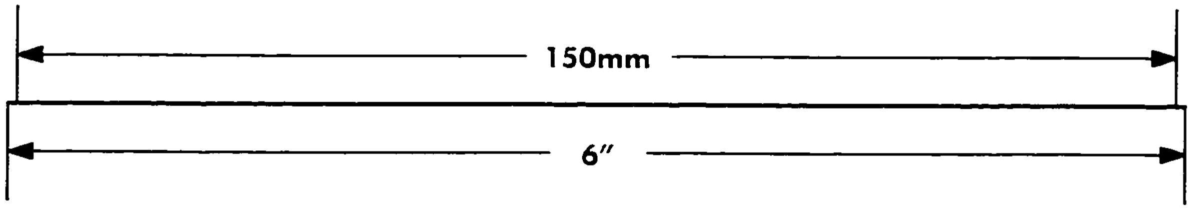

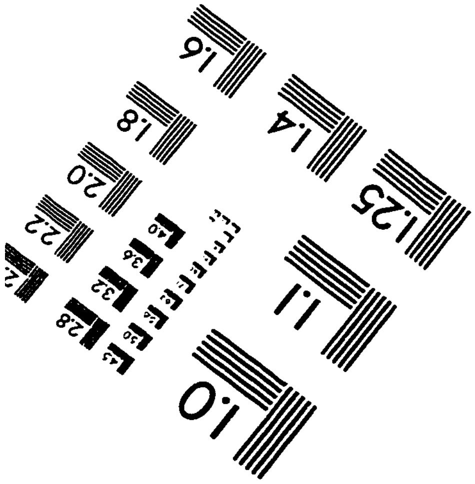

APPLIED IMAGE. Inc
1653 East Main Street
Rochester, NY 14609 USA
Phone: 716/482-0300
Fax: 716/288-5989

© 1993, Applied Image, Inc., All Rights Reserved